A thesis entitled

Theoretical and Experimental Investigation of Quantum Well Intermediate Band Solar Cells

by

Megumi Ito

Submitted for the degree of
Doctor of Philosphy
of the
Imperial College London
Department of Physics

September 2014

Declaration of Originality

I, Megumi Yoshida, hereby declare that this thesis represents my original work undertaken by solely by myself or collaboratively with my colleague, and that I have used no other sources except as noted by citations. All data, figures and text citations which have been reproduced from any other source, including the journals and internet, have been explicitly acknowledged as such.

Acknowledgements

First and foremost, I would like to express my unreserved gratitude to my excellent supervisors Dr. Ned Ekins-Daukes and Prof. Chris C Phillips for giving me this great opportunity to work on this project and to join their research groups. Ned has always been the most supportive and understanding supervisor I could have ever wished for. He is an inspiration and without his encouragement, guidance and patience that he has offered me since the days of my undergraduate research program in 2009, I am certain in my mind that I would not have had the confidence to pursue my studies in the form of a PhD. I am so lucky to have also had such a driven and knowledgeable co-supervisor in Chris, who is beyond doubt the most enthusiastic professor I have ever met and from whom I have learned so much, through having numerous discussions on a variety of interesting topics.

I would also like to extend my appreciation to all of my colleagues in the QPV and EXSS group, more than anything for their support, especially during tough times. I thoroughly enjoyed the many interesting discussions that we shared during tea breaks and the great social activities that we participated in together, including conferences and travel.

I certainly must accredit Dan Farrell, Jordi Farah and Markus Führer for sharing their theoretical work and providing me with much needed advice. Hemmel Amrania and Edward Yoxall also deserve a special mention for sharing their experimental work for this project. Without their help, I would certainly not have made it this far.

The samples used in this project were supplied by Dr Edward Clark, Dr Ken Kenedy and Dr John Roberts of the University of Sheffield, along with Prof. Keith Barnham of Imperial College London. I am eternally grateful for their tireless attention to detail which has ultimately provided us with such a valuable set of samples that will allow us to pursue our research further.

I would also like to acknowledge the Imperial College International Scholarships for supplying the funding and studentship for the PhD project. I must greatly emphasise my appreciation for Sharp Laboratories of Europe Ltd, who have generously provided financial support throughout the course of this project, while also supplying the nitride sample used in my experimental research.

Away from the academic world, I would also like to thank my parents, Tadatsugu and Masako, for introducing me to the fascinating world of science in the first place, as well as letting me study in a country so far away from home and supporting me all of the way, allowing me to follow my dream from childhood up until now.

Finally, to my husband Kenny, thank you so much for your support, understanding, proof reading and love.

Abstract

In order for photovoltaic energy conversion to compete with conventional energy sources and become a realistic alternative source of low-carbon renewable energy, significant cost-per-watt reduction is required. One obvious way to achieve this is to increase the conversion efficiency of solar cells, which is currently limited to around 30% even with modern technology.

The Intermediate Band Solar Cell (IBSC), the focus of this project, is a concept that promises photovoltaic power conversion efficiencies of up to 63.2% through the introduction of an extra energy band in the bandgap of a semiconductor. However, many attempts to achieve IBSCs using quantum dots superlattice show poor conversion efficiency due to their small absorption cross-section and short-lived intermediate state. In this project, we attempt to overcome this issue by proposing an innovative *Photon Ratchet* (PR) quantum well cascade structure designed to improve the efficiency, through increasing the absorption cross-section and the lifetime of electrons in the intermediate state. The goal of this project is to prove the benefits of this concept, both theoretically and experimentally.

In this thesis, theoretical and experimental work on quantum well solar cells is presented. The basic concept of solar cells, IBSC and PR-IBSC as well as their advantages and disadvantages are discussed in chapter 1, along with theory of quantum mechanics and optical transitions in quantum wells. Chapter 2 focuses on theoretical work, which includes limiting efficiency calculation and fundamental loss calculation in solar cells, in order to determine the fundamental benefit of the PR-IBSC when compared with conventional IBSCs. The result of this work was published in *Applied Physics Letter* in 2012 to propose the concept of the PR-IBSC for the first time. Experimental work on existing quantum well solar cells is presented in chapter 3, along with basic characterisation techniques. The InGaAs quantum well with GaAs barrier in a p-i-n diode is optically and electrically characterised and we describe how we have observed an increase in photocurrent due to sequential absorption of photons via the intermediate band (IB), which arises from the one-dimensional confinement in the quantum well, for the first time. This is an important result and has been published in the *Journal of Photovoltaics* in 2014.

In order to study the interband and inter-subband transitions in quantum wells individually, we also designed a new set of samples, along with their reference samples, which consist of n-i-n and p-i-n diodes with identical single quantum wells in the i-region. The details of the samples, along with a model which simulates the transitions in quantum wells and achieves basic characterisation of the samples, are presented in chapter 4. Finally, in chapter 5, we draw up our conclusions and future work on the new samples is discussed.

Table of Contents

List of Figures

Chapter 1

Introduction and Fundamental Concepts

In this chapter, we first review current world energy economics which is ultimately driving the motivation for using solar power. It is followed by the discussion of fundamental concepts of different solar cells which are important to this project. It is important to understand the mechanisms of solar cells as well as avoidable and unavoidable loss mechanisms which limit their efficiency. Better understanding of these concepts has led to the development of a new type of solar cell, the Intermediate Band Solar Cell (IBSC), which aims to increase the efficiency limit by cutting down on losses incurred in conventional solar cells. With its challenge, we introduce an innovative concept of the photon ratchet, designed to improve the performance of the IBSC. Finally, the basics of quantum mechanics and our motivation of using quantum wells to realise this type of device are discussed.

1.1 Energy, Human Activities and the Environmental Issues

Life requires energy to maintain its existence: all living organisms extract energy from the environment or food and convert it to a form which can be used to make new cells and keep cells alive. In the ecosystem of the Earth, the majority of the initial energy comes as light from the Sun which green plants absorb and convert into chemical energy via photosynthesis. The herbivores then eat the plants, absorbing stored energy in the plant through digestion and transforming it into the form of energy they desire. The predator finally consumes their prey to extract energy from them. We, human beings, are also a part of this food chain within this ecosystem.

On top of the use of the Earth's resources to improve their chance of survival, humans also use extra energy to enhance their quality of life by converting it from forms that are less desirable to those are more practical. There is some evidence that the use of fire, which differentiates us from other living creatures, was already present at the early stage of human history. However, for most of mankind's fifty thousand year history, the use of energy has been severely limited. The discovery of fire and the burning of wood and charcoal provided an immediate source of heat and artificial lighting. Throughout thousands of years, we have developed ways to harvest energy and to make use of it more efficiently in order to achieve a more convenient life. This includes harnessing the power of oxen and horses for agricultural activity and transportation, as well as the use of water wheels and windmills to access useful power, dramatically increasing the mechanical capabilities in agricultural production.

The significant change in the way we use energy came in the mid-18th century in the form of the Industrial Revolution. A wave of unprecedented innovation and advancement, ushered in by James Watt's enhancement of the steam engine, caused a 3-fold increase in energy consumption by 1875. Among other things, the steam engine enabled us to use the Earth's vast concentrated storage deposits of solar energy - namely coal, natural gas and oil providing energy beyond the limit of what could be provided by natural energy flows. The inventions during this period changed the way we produce and live in many ways. One of the major changes was the use of machines, which replaced human labour in many industries including food production, medicine, housing and clothing. This enabled us to develop better products through faster processes. The increases in energy consumption had been gradual throughout history, but once industrialisation occurred, the rate of consumption increased dramatically over a period of just a few generations.

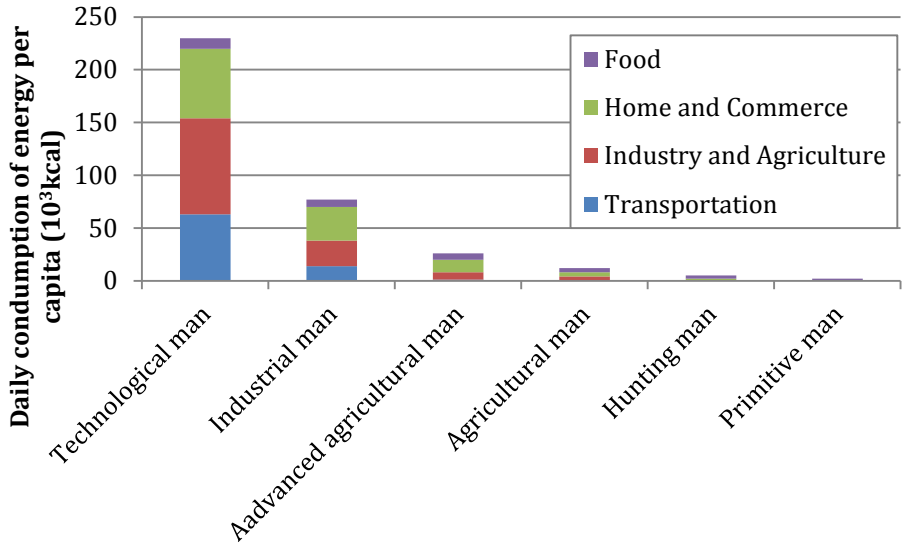

Figure 1: Daily consumption of energy per capita[1]

With the development of transport methods and infrastructure, energy has become easily accessible in our daily lives and an essential element of modern society. Aeroplanes dramatically reduced the amount of time it took to travel between countries and enabled importing and exporting items worldwide, including fresh food. In developed countries such as the United Kingdom and the United States of America, cities cannot function without public transport such as trains and buses and every other person now owns a car. Almost all houses are connected to electricity grids and have gas supplies which enable us to have an instant supply of power to heat up homes, have hot water, light up rooms and cook food 24 hours a day, 365 days a year. As well as establishing a convenient lifestyle, we also use power for entertainment such as TV, cinema, amusement parks, etc. With such a rich lifestyle, we consume hundreds of times more energy than we require for survival, as can be seen in

Figure 1. Our current economics are supported by a computer controlled environment with fast transport of goods and people, requiring a constant and instantaneous supply of energy.

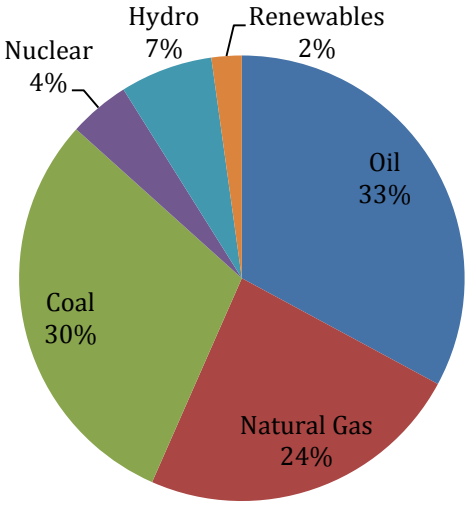

Figure 2: Percentage breakdown of global energy consumption. [2]

Most energy consumption of industrialised countries comes from the use of stored chemical energy from media such as oil, coal and natural gas (as shown in Figure 2), sources known as fossil fuels. In fact, the energy that they produce reaches a combined total of 87% of all energy used worldwide.[2] Fossil fuels form from the remains of dead plants and animals buried underground or at the bottom of the sea. Over millions of years of fossilisation, these got decomposed and, through high pressure and temperature, got converted into the various forms we know today. Stored deep underground, they can be obtained by drilling rigs or mining to reach their reserves. As they take the form of solid, liquid or gas, they are easy to transfer, dense in energy and simple to extract energy from. However, since they are simply a form of stored energy from millions of years ago, their supply is limited and with an exponentially increasing demand in energy over the past 150 years, their reserve is declining ever rapidly.

There are some concerns over the environmental impact caused by the current sources of energy.[3] When fossil fuels are burnt they emit large amounts of carbon dioxide and other harmful gases, which is said to have a negative effect on the environment and human health. Carbon dioxide, methane and other greenhouse gases naturally trap sunlight and do not allow it to leave the atmosphere, helping to maintain consistent temperatures. However, it is widely accepted that the extra emission from the burning of fossil fuels has caused a high rise in greenhouse gas volumes far beyond their natural existence, which is said to be causing temperatures to rise.[4] Additional consequences that are frequently attributed to the increase in greenhouse gases include the rise in sea levels, extreme

weather events and changes in rainfall patterns.[5] This is known as *climate change* and may lead to drastic changes in the ecosystem, geography and living environment.

After World War 2, the establishment of controlled energy release from nuclear fission led to the development of nuclear electricity power plants, which make up 4% of current energy economics.[2] These were believed to be the perfect solution to replacing the existing electricity power plants, reducing the high dependency of energy on fossil fuel. Nuclear energy is low in carbon dioxide emission, comes from natural resources and is capable of generating large amounts of electricity, via faster processes compared to other sources of electrical energy. However, they also present some significant issues. Even though the nuclear fission process and its source is clean, the resultant radioactive waste is harmful for the environment. Also, as highlighted from recent events, there is a high risk to human beings and nature which are caused by nuclear power plant accidents. The disasters at Three Mile Island in 1979, Chernobyl in 1986 and Fukushima in 2011 caused fatalities and left long-term consequences which take decades to clean up. After the realisation of this risk, the number of new power plants built worldwide declined dramatically. Through the closure of existing plants once their operating lifetime comes to an end, the contribution of nuclear power to electricity generation is expected to reduce continuously.[3]

Currently, there is wide variation in the economic performance of different countries and regions around the world. Among the more mature Organisation for Economic Co-operation and Development (OECD) regions, although the pace varies across countries, GDP growth is generally slow in comparison with the emerging economies of the non-OECD regions. As the world continues to recover from the effects of the 2008-2009 global recession, economic performance has continued to lag and there are uncertainties in future growth. In contrast to the OECD nations, developing non-OECD economies, particularly non-OECD Asia, China and India, have been among the world's fastest growing economies for the past two decades. As there is a strong correlation between increase in GDP and increase in energy demand, it is not surprising that the energy consumption in those countries has also grown rapidly. With further emerging nations expected to grow, energy consumption is expected to continue growing over the next few decades. On top of this, the global population is also increasing steadily, which accelerates energy demand further yet. The International Energy Agency (IEA) says the world's energy needs could be 50% higher in 2030 than they are today.[2]

For the reasons mentioned above - the continuing increase in energy demand, concerns about the long-term environmental effects of current energy sources, the depletion of fossil fuels and reduction of nuclear power contribution - it is clear that harnessing other sources of energy is definitely desirable and will eventually be vital. The solution will come from renewable energy which is

generated from sources that can be replenished naturally and promptly, thus will never run out. There are currently many major forms of renewable energy, including those listed below. [3]

- Solar radiation
- Hydro
- Wind
- Photosynthesis
- Geothermal energy
- Tidal energy

In this project, we focus on the direct harvesting of solar energy as described in detail in the following section.

1.2 The Sun and Solar Irradiance

The sun which we orbit provides a virtually unlimited source of energy that powers the Earth's climate and ecosystem, as mentioned above. It is vital for life and maintains the atmospheric and surface temperature of the planet through constantly supplying energy. The sun is a sphere of hot gas heated by chain of nuclear fusion reactions of two hydrogen atoms forming a helium atom at its core. Although the temperature of the core reaches 20,000,000K, with a thick layer of hydrogen ions in between, the surface of the sun is much cooler and emits electromagnetic radiation closely matching to a blackbody spectrum of temperature 5777K.[6]

The emitted radiation spreads out spherically after leaving the solar surface. With the Earth orbit located at the average distance of 149,600,000 km from the Sun, the average radiant power per unit area outside the Earth's atmosphere is 1,353W/m^2. This is the value used to calculate the estimated solar power generation in satellites and the distribution of the solar spectrum is known as *air mass zero* (AM0) radiation as it has not gone through any atmosphere. With the total solar radiation continuously available to the Earth being as large as 162,000TW,[7] it is greatly exceeding the average worldwide primary power consumption of 16.6TW in 2013 and it presents an attractive renewable power source.[8]

When the solar radiation passes through the Earth's atmosphere, it is attenuated at least by 30% due to several causes such as: the Rayleigh scattering of short wavelength radiation by air molecules in the atmosphere, aerosols and dust particles scattering, and absorption by atmospheric gas particles such as, oxygen, carbon dioxide and water vapour. As the composition of the atmosphere varies with the location, weather condition, season, environment and time of the day, the spectral distribution of the

sunlight at the surface of the Earth differs. However, as the most important parameter in the clear condition is the length of the light path through the atmosphere, the solar spectrum is characterised by the ratio of the path length to its minimum value known as the air mass coefficient (AM). The standard value used as a globally representative direct solar irradiance at the surface is AM1.5 with the total power density of 1,000kW/m^2. On top of the direct irradiation, scattered photons by the atmosphere also contribute to the diffuse light and it is particularly important in the poor weather conditions.

1.3 Photovoltaic Effect and Solar Cells

A solar cell is a device which operates by converting sunlight into electricity using the electronic properties of semiconductors and other materials such as organic molecules. The majority of conventional flat-panel solar cells are made from crystalline silicon wafer and account for more than 80% of the cumulative PV capacity installed.[9] They are called first generation solar cells and their performance can be as high as 20%, as represented by the green area in Figure 3.[10] However, their price per unit energy (cost-per-watt) remains relatively high due to the volume of silicon used in the system and inefficiencies in the manufacturing process. In order for photovoltaic energy conversion to compete with conventional energy sources, significant cost-per-watt reduction is required. There are two main approaches to overcome this problem, each forming the basis of a new class of photovoltaic technology.

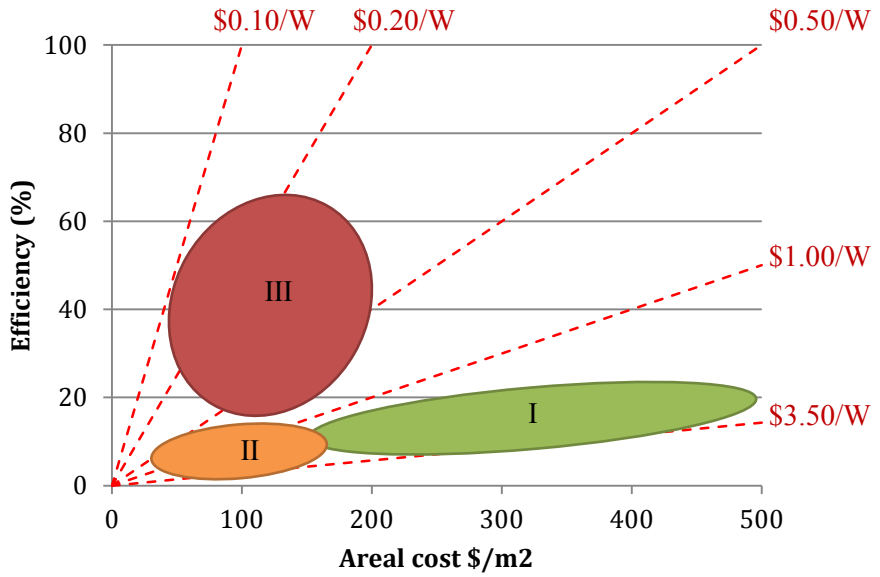

Figure 3: Three generations of PV technology: I – first generation is made of crystalline silicon, II – second generation is a thin-film PV and III – third generation is high performance technologies. [10]

The first class, known as the second generation solar cell, utilises thin-films of semiconductor deposited directly onto glass, plastic or metal foil in order to minimise the amount of semiconductor material required. A significant cost reduction is achieved by this thin-film technology but the efficiency of the device still remains low, at 10%.[9]

The second class - the third generation solar cell - aims to improve the efficiency of photovoltaic conversion targeting the thermodynamic efficiency limit of 86.8%. The highest efficiency ever to be achieved was 44.7% using a four-junction solar cell (by SoiTec in 2013) and 44.4% using a triple-junction solar cell (by Sharp in 2012),[11] but the manufacturing cost for these is still very high. Other third generation technology includes hot-carrier and intermediate band photovoltaic conversion. The long-term goal is to be able to manufacture a low-cost, high-efficiency third generation photovoltaic panel.

The most main stream of the solar cells operates by making use of photovoltaic effect in semiconductor materials, which enables a direct conversion of energy from sunlight generating electrical power.[12]. In this section, the semiconductor physics and basics of solar cell operations as well as the main loss mechanisms are looked at.

1.3.1 Semiconductors as Absorbers in Solar Cells

Semiconductors are materials with two characteristic bands of electronic states: the valence band (VB) and the conduction band (CB), separated by an energy gap (bandgap) as per Figure 4a. In a semiconductor at a temperature of 0K, the electronic states in the conduction band are completely empty and the valence band is filled by electrons. In order for a material to conduct, it must have electrons and empty states in the same band so that an electron can move to fill an empty state without requiring a significant energy, while leaving an empty state for another electron to fill. In a semiconductor, because there are neither any available states for electrons to go to within the valence band, nor any electrons to move around in the conduction band, its conductivity is zero at 0K.

However, this electronic property can be modified by *doping*, through adding a small amount of specific impurity atoms to a semiconductor which replace those of the semiconductor at their lattice position. When an impurity atom has one extra electron compared to the semiconductor atoms, the extra electron is not used for chemical bonding with the neighbouring atoms and remains free. The free electron can then move around to conduct electricity and the semiconductor becomes conductive. These impurity atoms are called donors because they donate an electron to the conduction band of the semiconductor and such semiconductors doped with donors are called n-type semiconductors, as shown in Figure 4b.

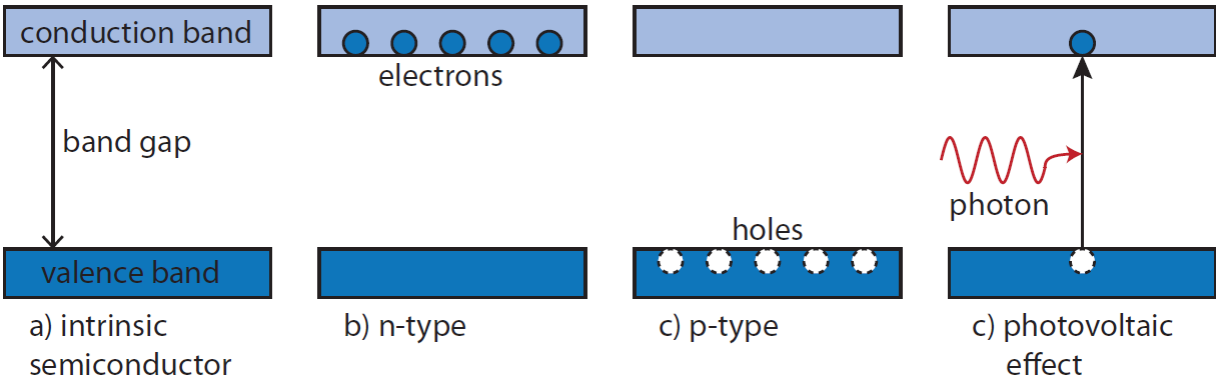

Figure 4: Semiconductor is a material with valence band (VB) and conduction band (CB) separated by bandgap. a) In an intrinsic semiconductor, the VB is full and the CB is empty at 0K. b) n-type semiconductor has extra electrons in the CB. c) p-type semiconductor has extra holes in the VB. d) photon is absorbed to create electron-hole pair.

Similarly, an impurity atom with one less electron than necessary for chemical bonding creates an empty state (hole) for an electron to move into and again the semiconductor becomes conductive (Figure 4c) These impurity atoms are called acceptors as they accept an electron from the valence band and the doped semiconductor is called p-type.

Furthermore, an electron in the valence band can be promoted into the conduction band by absorbing a photon with energy larger than the bandgap (Figure 4d). This is known as the photovoltaic effect and solar cells convert solar energy to electrical energy using this effect by extracting the excited charge carriers to the outer circuit.[13]

1.3.2 pn-junction and Operation of Solar Cells

In order to extract useful power out of a semiconductor, the excited electrons have to be efficiently extracted from the conduction band. The most common implementation of the photovoltaic concept is the semiconductor pn-junction. When a semiconductor is n-doped, its Fermi level, which represents the occupation of the bands, moves closer to the conduction band, as per Figure 5b. On the other hand, in p-type semiconductors, the Fermi level moves closer to the valence band, as shown in Figure 5a. When n-type and p-type semiconductors are connected, electrons near the junction in the n-type semiconductor move to the p-type semiconductor, leaving positive charge behind. Similarly, holes in the p-type semiconductor move to the n-type semiconductor leaving negative charge. This creates charge separation at the interface called the depletion region and creates an electric field across the junction, Figure 5c. This structure is known as the pn-junction which has constant Fermi energy, which also represents free energy per carrier, throughout the junction, as well as an energy barrier called built-in potential at thermal equilibrium.[12,14]

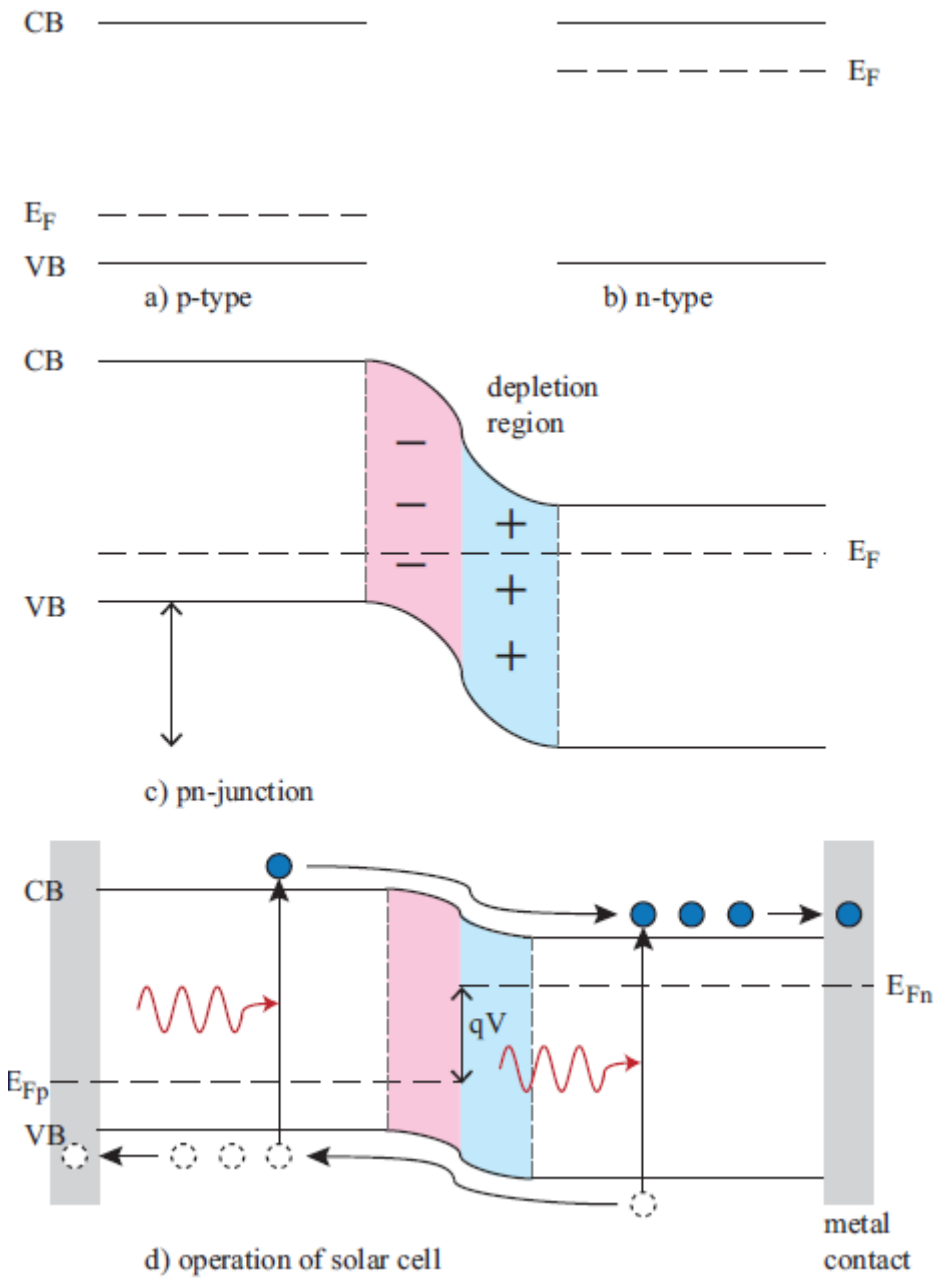

Figure 5: a) p-type semiconductor b) n-type semiconductor c) pn-junction is formed where p and n-type semiconductors are connected. d) solar cell, pn-junction under light and forward bias

When an electron is optically excited from the valence band into the conduction band on the p-side, it can diffuse to the pn-junction and be drifted over to the n-side by the electric field as shown in Figure 5d. In the same way, a hole created by absorbing a photon on the n-side moves to the p-side. Therefore, the charges created in the solar cell can be separated by the pn-junction and electrons (holes) can be extracted by a metal contact on the n-side (p-side) causing the photocurrent to flow. The build-up of carriers on each side of the junction increases the carrier density and shifts the Fermi-level closer to the bend-edge. This means that the electrons in the conduction band of the n-side to have higher free energy than the electrons in the valence band on the p-side, resulting in the splitting

of the Fermi levels on the two sides of the junction. The difference between the Fermi levels determines the voltage of the solar cell and the electrical power generated by the solar cell is given by the photocurrent multiplied by the voltage.

1.3.3 Loss Mechanisms in Solar Cells

The performance of a solar cell is determined by several factors such as the quality and design of the device. It is important to understand loss mechanisms in solar cells in order to envision potential improvements on efficiency. The loss processes occurring in a single bandgap device under 1-sun illumination can be divided into two distinct categories. Extrinsic losses, such as series resistance, parasitic recombination and contact shadowing, can substantially limit device efficiency. However, these are theoretically avoidable by improving the quality of the device. In contrast, intrinsic losses are unavoidable and fundamentally limit the efficiency of single junction solar cells to 30% under 1-sun illumination (Shockley-Queisser limit). [10,15,16] Figure 6 graphically represents the proportion of five intrinsic loss mechanisms which will still be present in an idealised solar cell.[17]

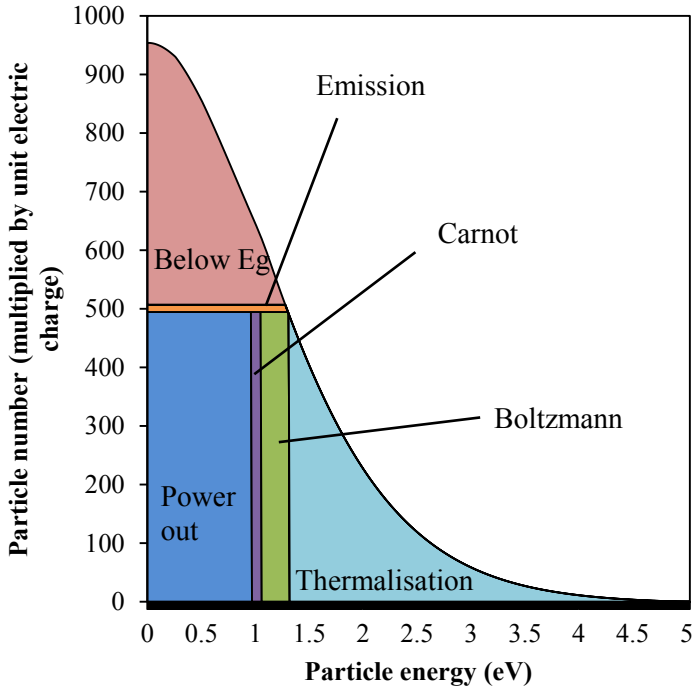

Figure 6: Intrinsic losses occurring in the optimal bandgap (Eg = 1.31eV) single junction solar cell under 1-sun illumination. 1) below-bandgap Eg loss, 2) thermalisation loss, 3) Boltzmann loss, 4) Carnot loss and 5) emission loss[17]

Some of the main intrinsic loss processes are shown in Figure 7. When an incident photon has energy lower than the bandgap of the semiconductor, it cannot be absorbed and does not contribute to electrical power (Figure 7(1) below-bandgap loss). On the other hand, a photon with higher energy

than the bandgap will be absorbed creating an electron-hole pair. However, the electron and hole lose part of their excess energy in the form of phonons to reach thermal equilibrium with the lattice (Figure 7(2) thermalisation loss). Therefore only photons with energy close to the bandgap of the material are efficiently converted to electrical power. Moreover, some of the electron-hole pairs recombine, radiatively emitting photons (Figure 7(3)) and the electron and hole lose some of their energy at the contacts (Figure 7(4) Carnot loss).[18] The calculation of each of the loss mechanisms are presented in section 2.3.

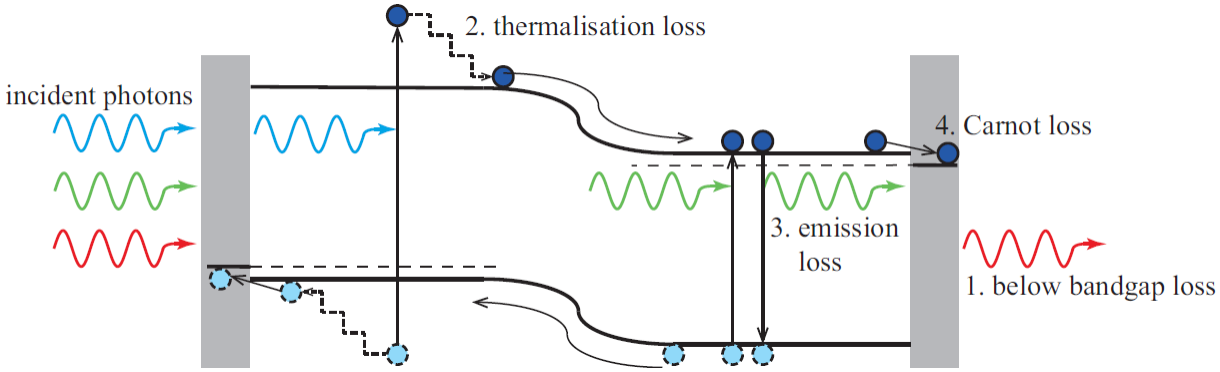

Figure 7: Loss mechanisms in solar cell.

Many designs for solar cells have been proposed to minimise these losses and push the efficiency beyond the Shockley-Queisser limit – these are the so-called third generation solar cells mentioned previously. A multi-junction solar cell has typically 2 to 4 pn-junctions of different bandgaps connected in series so that it can harvest a broad band of the solar spectrum efficiently.[10] High energy photons are absorbed by high bandgap semiconductors reducing thermalisation loss, and low energy photons are absorbed by the low bandgap junction reducing below-bandgap loss. The efficiency limit of an infinite number of junctions covering the full solar spectrum is 86% at full concentration, which is maximum geometric factor that can be achieved by optical concentrator corresponding to matching of absorption and emission solid angle.[19] (Details are explained in subsection 2.2.3) The hot carrier solar cell is a concept which impedes the thermalisation loss by extracting the carrier before relaxation occurs. The limiting efficiency of a hot carrier solar cell is 85% at full concentration.[10]

Finally, since the sun covers only part of the sky, there is inequality between the absorption and emission solid angle of solar cells. This causes entropy generation and reduces the free energy of the carriers, introducing the Boltzmann loss (Figure 6).[20,21] This loss can be eliminated when the absorption and emission solid angles are matched by either using concentration optics (at full concentration) or restricting the emission angle, through which the efficiency limit is increased to 40.7%. More details of the Boltzmann loss are presented in a later section.

1.4 The Intermediate Band Solar Cell

The Intermediate Band Solar Cell (IBSC) has been proposed by Luque and Marti in 1997 as an alternative way to exceed the Shockley-Queisser limit by harvesting broadband solar spectrum more efficiently and is a strong focus of study for next generation solar cells.[22] In an IBSC, there is a band of electronic states, an intermediate band (IB), introduced between the conduction and valence bands. The intermediate band is optically coupled to the conduction and valence bands but electrically isolated from them. This enables electrons to be excited from the valence band to the conduction band via the intermediate band by sequential absorption of two sub-bandgap photons, which would otherwise be unabsorbed, thereby reducing below-bandgap and thermalisation losses, as shown in Figure 8. In principle, by introducing the IB, the photocurrent can be enhanced without significantly reducing the voltage, hence leading to higher conversion efficiency. The theoretical limiting efficiency of the IBSC concept is calculated to be 63.2% at full concentration, which is much higher than the corresponding Shockley-Queisser limit of 40.7%.[21]

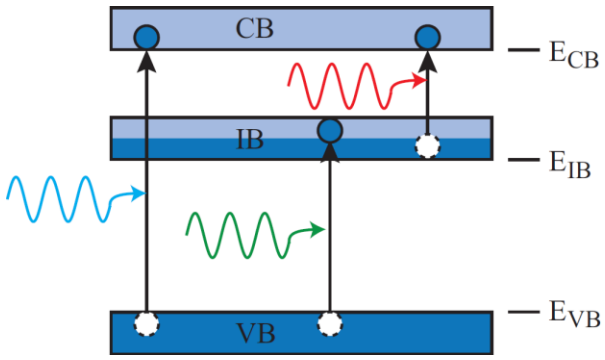

Figure 8: The IBSC has a radiatively active but electrically isolated band between valence and conduction bands. Sequential absorption of two low energy photons can create electron-hole pair in conduction and valence band contributing to photocurrent.

Many studies have attempted to create an intermediate band material using quantum dots, [23,24,25] impurity bands [26] and dilute semiconductors.[27] However, even though an increase in photocurrent has been observed in quantum dot IBSCs, they suffer from a significant voltage loss resulting in low conversion efficiency [28,29]. One of the main causes of the voltage reduction in the IBSCs is due to the short lifetime of electrons in the intermediate states, which is caused by fast non-radiative recombination.[30] In these cells, radiative and non-radiative recombination of carriers occurs before the two-photon absorption can take place, and this leads to a reduction in the quasi-Fermi level separation.[31]

Highly-mismatched alloys are a combination of group III and V or group VI and IV semiconductor elements containing isoelectronic elements with very large differences in terms of atom size, ionicity, and electronegativity, such as GaAsN.[32] In such materials, a highly electronegative and isoelectronic

impurity atom, such as N in GaAs, introduces localised s-like states near the conduction bend-edge of the host compound, while a large metallic impurity atom with much lower ionisation energy than that of the host anion, such as As in GaN, introduces localised p-like states near the valence bend-edge. An anticrossing interaction between the localised states of these impurity atoms and the extended states of the host leads to a restructuring of the band into E+ and E- subbands.[33] In GaAsN alloys, the CB forms multiple electronic bands and E- and E+ can act as the IB and CB. Lopez et al. have designed and tested a GaAsN IBSC device and proven it is possible to make contact to the E+ level.[34] N. Ahsan et al. demonstrated 1.0% increase in quantum efficiency with IR radiation exciting transition from E- to E+.[35]

In a quantum dots superlattice, the subbands, generated by quantum confinement effect, are well separated in energy space from other bands in theory and form a perfect IB.[36] If the quantum dots are spherical and distributed homogeneously, in principle the energy separation between the subbands leads to a long radiative lifetime of carriers and there has been extensive experimental effort to demonstrate the use of quantum dots super lattices as IBSCs.[22] Marti et al reported an increase in photocurrent in a δ-doped InAs/(Al,Ga)As quantum dot system with continuous infrared light exciting carriers from the IB to the CB.[37] However, the photocurrent increase observed was as small as 10^{-2} % of the initial value. We also observed photocurrent enhancement of 1mA from a single InGaAs/GaAs QW with a high power mid-IR laser exciting intersubband transition, detail of this is examined in chapter 3.[38] A recent report by Okada et al also shows a small increase in external quantum efficiency of 0.3% in a δ-doped InAs/GaNAs quantum dot solar cell, [23] while Sugiyama et al achieved 0.5% in a InGaAs/GaAsP strain-balanced quantum well superlattice cell.[39] Kita et al reported proof of sequential absorption of photons via the IB in the form of bleaching and recovery of photoluminescence (PL) in InAs/GaAs quantum dots in an optical cavity.[40] They concluded that sequential absorption of photons was actually a two-photon process and can only occur with high optical excitation energy.

As demonstrated in the above literature, sequential absorption of the photons is possible in both quantum wells and quantum dots. However, the short lifetime of the carriers in excited-state remains a critical problem in realising efficient IBSCs. In fact, all experimental reports on IBSCs show only a very weak enhancement due to the sequential absorption of photons, which generates a negligible gain in energy conversion efficiency. The short lifetime of electrons in intermediate states is mainly caused by rapid non-radiative recombination, that proceeds faster than all radiative processes.

Furthermore, it has been reported that the short-circuit current of a real IBSC is strongly dependent on the occupation of the IB, since the number of intermediate states is limited.[41] In order for photo-generation to occur, the lower state must be occupied by an electron and the upper state must be empty, where the strength of this transition is described by the absorption coefficient of photons at the

corresponding energy.[42] In a real IBSC, the absorption coefficient for IB-CB transition depends linearly on the occupation factor of the intermediate states f_{IB}, as $a_{IC}f_{IB}$, where a_{IC} is the absorption coefficient constant for the transition, so a small occupation of the IB leads to a small contribution to the short-circuit current from the IB.

Hence, the cause of reduction in both open-circuit voltage and short-circuit current comes from the short lifetime and small occupation factor of the IB. This implies that the efficiency advantage offered by the IB concept can only be realised if the lifetime in the IB state is increased to a point where the sequential absorption process is effective.

1.5 The Photon Ratchet Intermediate Band Solar Cell

In this project, we propose and investigate a new concept - the 'photon ratchet' intermediate band solar cell, Figure 9, in order to enhance efficiency by increasing the lifetime of the intermediate state.[43] A non-emissive ratchet band (RB) is introduced at a small energy interval ΔE below the intermediate band. If a fast thermal transition between the intermediate band and the ratchet band is assumed, then this energy drop ΔE enables the rapid relaxation of carriers from the intermediate band into the ratchet band. Provided that the ratchet band is not coupled radiatively to the valence band, the lifetime of the ratchet state can potentially be very long, thereby increasing the IB-CB generation rate. At the same time, the photon ratchet reduces the population of the intermediate band, which, in turn, reduces the recombination rate of the electrons from the intermediate band to the valence band. Therefore, this new concept increases the photocurrent of the solar cell by enhancing the probability of a two-photon absorption event and decreasing the recombination rate of the electrons, leading to higher efficiency.

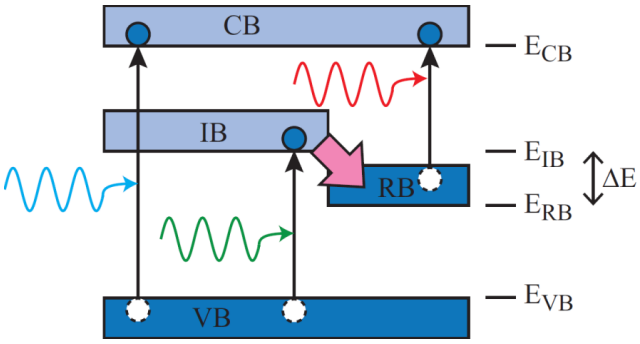

Figure 9: The photon ratchet IBSC has a ratchet level just below the intermediate band. The excited electrons in the intermediate band rapidly relax into the ratchet level which is radiatively isolated from the valence band enhancing the electron lifetime.

In terms of implementing the photon ratchet IBSC, there are a number of existing systems which are strong candidates. Photon ratchet states can be separated in momentum space by using an indirect bandgap semiconductor,[44] where electrons are first excited into a direct IB state, followed by a relaxation down via phonon emission to an indirect photon ratchet state, which is at lower energy and separated by momentum k from the IB state. Since the recombination from the indirect photon ratchet state to the VB requires simultaneous multiple phonon emission, the radiative emission from the photon ratchet state is weak. A radiatively isolated state can also be found in a molecular system as a triplet state where transition to singlet ground state is forbidden,[45, 46] and in ferromagnetic compounds.[47]

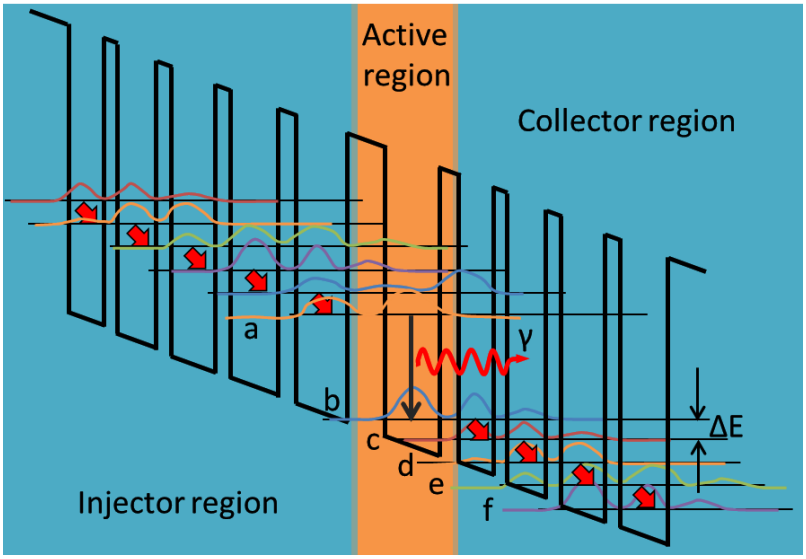

Figure 10: Schematic energy diagram of quantum cascade structure in a quantum cascade laser. Charge carriers are quickly transferred down from the upper level in the left most quantum well to the lower level in the right most quantum well due to phonon scattering.

A quantum cascade structure is a suitable structure for a photon ratchet IBSC since it enables it to achieve the desirable energy levels and rapid transfer of electrons from the intermediate band to the ratchet level. The fast transport is demonstrated in a quantum cascade laser which is a unipolar inter-subband laser emitting light through a series of inter-subband transitions in the conduction band.[48] In such a system as illustrated in Figure 10, the population inversion can only be achieved by the fast injection of carriers into the upper states (a) of the active regions, as well as through the fast collection from the lower states (b). By introducing a state (c) located at approximately one phonon energy below the lower state of the lasing transition (b), the resonant nature of the optical phonon emission induces a fast transition between these two states and reduces the lifetime of (b) to about 0.6ps.[49] Similarly, through constructing the subsequent quantized-level energy staircase which is separated by phonon energy, the fast transport of electrons occurs by sequential resonant tunnelling.[50] By

implementing this structure between the IB and the RB, the fast thermalisation of electrons into the RB can be achieved.

The other requirement of this concept is the optical isolation of the ratchet level from the valence band and this can be achieved by spatially isolating the carriers while incorporating a type-II structure. In type-II systems, the bandgaps of the materials are aligned such that the quantum wells in the conduction and valence bands are formed in different materials, as illustrated in Figure 11. This leads to the electrons and holes being confined in different layers of the semiconductor. The consequence of this is a reduced recombination rate of electrons and holes, which is determined by the overlap of their envelope functions.[51,52,53]

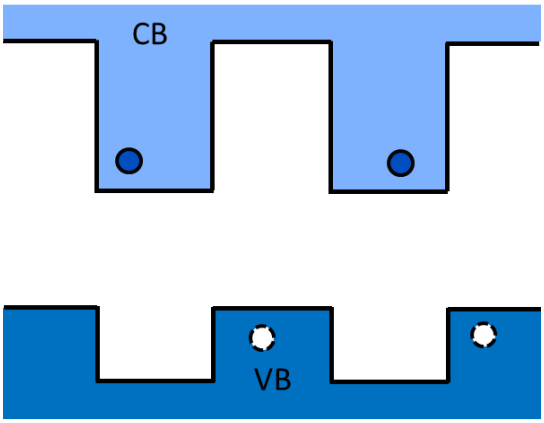

Figure 11: The one-dimensional potentials in the conduction and valence bands for a type-II quantum wells

Until now, IBSCs have been examined using III-V semiconductors such as InAs and GaAs. However, the bandgaps of these materials are small and energy separations of the three bands are far from ideal, specifically 0.71, 1.24 and 1.95eV.[22] The ideal operational region of the IBSC made with these materials is in the long wavelength part of the spectrum. By using different materials with a higher bandgap such as GaN, AlGaAs and GaAsP as a barrier, the two-photon absorption process can be shifted towards shorter wavelength radiation making it more beneficial for improving the efficiency of photovoltaic devices. Despite having an advantage with their large bandgap, nitrides have hexagonal lattice structures and they are difficult to fabricate or model. Therefore, most of the fundamental work in this project, such as proof of concept, will be undertaken using GaAs based structures.

Amongst other possible quantum structures, we have chosen to study quantum wells as a potential IBSC material and the detail and advantages of using this material are described in the following section.

1.6 Quantum Mechanics: Bulk Semiconductor Material, Quantum Well, Quantum Wire and Quantum Dots

The majority of the III-V semiconductors have a zinc-blend crystal structure. It is convenient to approximate the electrostatic potential as a three-dimensional lattice of spherically symmetric ionic core potentials screened by the inner shell electrons, which are further surrounded by the covalent bond charge distributions. This enables the Schrödinger equation derived for an electron in a vacuum to be used with an empirical fitting parameter called the effective mass m^*. This is called effective mass approximation and the time-independent Schrödinger equation describes the wave function ψ of electrons as:

$$-\frac{\hbar^2}{2m^*}\nabla^2\psi = E\psi \tag{1.1}$$

and the energy eigenvalue of the electron is:

$$E = \frac{\hbar^2 k^2}{2m^*} \tag{1.2}$$

where $\hbar = \frac{h}{2\pi}$ is Planck's constant. This approximation has been experimentally found to be suitable for electrons near the bend-edge of both conduction and valence bands. The curvature of the relationship between E and k can be calculated from experiments and effective mass of GaAs is measured to be $0.067m_0$ for an electron in the conduction band and $0.6m_0$ for a heavy hole in the valance band where m_0 is the rest mass of an electron in a vacuum. This is a good approximation for a bulk semiconductor which has a dimension much larger than the scale of the electron wavefunction and it can be treated as being effectively infinite.

When two of such semiconductor materials are placed adjacent to each other, they form a heterojunction. However, as the effective mass and the bandgap of the materials would differ at the junction, the electron wavefunction orthogonal to the plane of the junction, in the z-direction, will also differ from the bulk case. The wavefunction can be obtained by solving the generalised one-dimensional Schrödinger equation for each band with the one-dimensional potential $V(z)$ and position-dependent effective mass $m^*(z)$.

$$-\frac{\hbar^2}{2}\frac{\partial}{\partial z}\left[\frac{1}{m^*(z)}\frac{\partial\psi(z)}{\partial z}\right] + V(z)\psi(z) = E\psi(z) \tag{1.3}$$

When a thin layer of a narrow bandgap material is sandwiched between two layers of a wider bandgap material, it forms a quantum well as shown in Figure 12. As the potential energy is lower in the well region compared to the barrier region, it leads to a confinement in the electron wavefunction, which

can be derived by solving the equation (1.3). The confinement leads to discrete electron energy states in the quantum well, $E_z = E_n$, which depends on the effective masses, energy depth of the well and the width. The corresponding wave function takes the sinusoidal form in the well and exponentially decaying function in the barrier in the z-direction. In the one-dimensional potential $V(z)$, as is the case with quantum wells, the charge carriers can move freely in the plane of the layers leading to two-dimensional dispersion, $E_{xy} = \frac{\hbar^2 |\boldsymbol{k}_{xy}|^2}{2m^*}$. Therefore the total energy of an electron or hole of mass m^* with in-plane momentum $\boldsymbol{k}_{xy}$ is equal to,

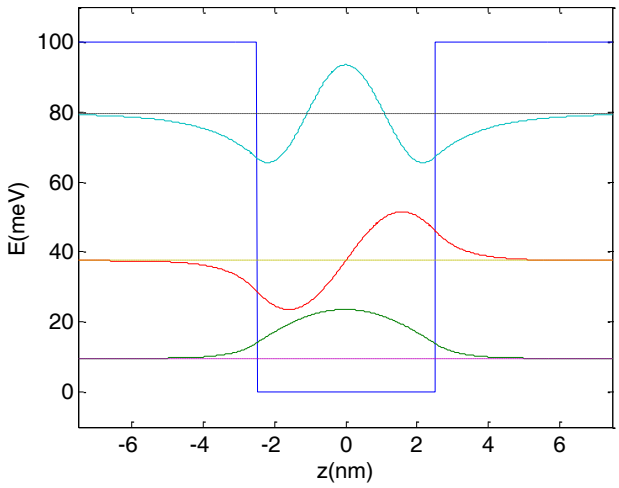

Figure 12: Conduction band-structure for a 5nm Quantum well with depth of 100meV showing first three confined electron states.

$$E = E_n + \frac{\hbar^2 |\boldsymbol{k}_{xy}|^2}{2m^*} \tag{1.4}$$

Electrons have spin $1/2$ and are Fermions. From the Pauli Exclusion Principle, each state can hold two charge carriers of opposite spins $\pm 1/2$. This leads to the density of states which defines the finite number of electron states within a specific energy range. In the bulk semiconductor crystal, which has three degrees of freedom and parabolic energy function of momentum around a minimum, the density of states within a band is continual and proportional to the square root of the energy:

$$\rho^{3D}(E) = \frac{1}{2\pi^2}\left(\frac{2m^*}{\hbar^2}\right)^{\frac{3}{2}} E^{\frac{1}{2}} \tag{1.5}$$

which defines number of electron states per energy per unit volume.

In quantum well systems, there are only two degrees of freedom as there is one-dimensional confinement and it leads to an energy-independent density of states for each confined subband.[54]

$$\rho^{2D}(E) = \frac{1}{2\pi}\frac{2m^*}{\hbar^2}E^0 \tag{1.6}$$

which is number of electron states per energy per unit area per quantum well layer.

When there is more than one confined state within the quantum well system, then the density of states at any particular energy becomes the sum over all subbands below that point, making it a step function. Similarly, for a quantum wire, which is a one-dimensional system, and quantum dots (0D), the density of states are:

$$\rho^{1D}(E) = \frac{1}{\pi}\left(\frac{2m^*}{\hbar^2}\right)^{\frac{1}{2}}E^{-\frac{1}{2}} \tag{1.7}$$

$$\rho^{0D}(E) = \frac{1}{2\pi}\frac{2m^*}{\hbar^2}\delta(E - E_n) \tag{1.8}$$

which are number of electron states per energy per unit length per quantum wire and per energy per quantum dot respectively.

The advantage of using such a confined system is that we can modify the optical characteristics of the material, such as the optical absorption edge. In this project, quantum wells are chosen to be examined as they take the simplest form, enabling the achievement of a high quality material with a large optical absorption cross-section.

1.7 Optical Transitions

Due to the quantum confinement and resulting discrete energy states, the quantum well has different optical characteristics compared to the bulk semiconductors. The optical absorption coefficient α is determined by the quantum mechanical transition rate $W_{i\to f}$ for exciting an electron in an initial quantum state ψ_i to a final state ψ_f by absorption of a photon with energy E_γ. The transition rate is given by Fermi's golden rule:

$$W_{i\to f}(E_\gamma) = \frac{2\pi}{\hbar}\left|\boldsymbol{M}_{if}\right|^2 g(E_\gamma)\delta(E_f - E_i - E_\gamma) \tag{1.9}$$

where $g(E)$ is the joint density of states for the transition. The matrix element;

$$\boldsymbol{M}_{if} = \left\langle \psi_i \middle| H' \middle| \psi_f \right\rangle = \int {\psi_f}^*(\boldsymbol{r})H'(\boldsymbol{r})\psi_i(\boldsymbol{r})\, d^3\boldsymbol{r} \tag{1.10}$$

where $\boldsymbol{r}$ is the position vector of the electron, describes the effect of the external perturbation H' caused by the light wave on the electrons. The quantum perturbation describes the electric dipole interaction between the light and the electron:

$$H'(\boldsymbol{r}) = -\boldsymbol{p}_e(\boldsymbol{r}) \cdot \boldsymbol{\varepsilon}_\gamma(\boldsymbol{r}) \tag{1.11}$$

where $\boldsymbol{p}_e = -e\boldsymbol{r}$ is the electron dipole moment and $\boldsymbol{\varepsilon}_\gamma(\boldsymbol{r}) = e\boldsymbol{\varepsilon}_0 e^{\pm i\boldsymbol{k}_\gamma \cdot \boldsymbol{r}}$ is the electric field of the photon. In a bulk semiconductor, the electron states are described by Bloch functions which is the product of a plane wave $e^{i\boldsymbol{k}\cdot\boldsymbol{r}}$ and a periodic function $u(\boldsymbol{r})$ that has the periodicity of the crystal lattice.

$$\psi_i(\boldsymbol{r}) = \frac{1}{\sqrt{Volume}} u_i(\boldsymbol{r}) e^{i\boldsymbol{k}_i \cdot \boldsymbol{r}} \tag{1.12}$$

The matrix element shows that momentum must be conserved, $\hbar\boldsymbol{k}_f - \hbar\boldsymbol{k}_i = \pm\hbar\boldsymbol{k}_\gamma$ for the optical excitation to occur. As the wave vector of photons is negligible, $\boldsymbol{k}_\gamma \sim 10^7 m^{-1}$, compared to that of electrons, initial and final electron momentum needs to be the same: $\hbar\boldsymbol{k}_f = \hbar\boldsymbol{k}_i$ for purely optical processes. For direct bandgap semiconductors, such as GaAs, the absorption coefficient is typically of order $10^6 m^{-1}$ and for indirect bandgap semiconductors, such as Si, it is much smaller as the optical excitation is required to be phonon-assisted.

In the case of quantum wells, one-dimensional confinement leads to a wavefunction which takes the form of a product of the Bloch function $u_i(\boldsymbol{r})$, free wave in xy-plane $e^{i\boldsymbol{k}_{xy,i}\cdot\boldsymbol{r}_{xy}}$ and the bound envelope function $\varphi_{i,n}(z)$ in the z-direction.

$$\psi_i(\boldsymbol{r}) = \frac{1}{\sqrt{Area}} u_i(\boldsymbol{r}) \varphi_{i,n}(z) e^{i\boldsymbol{k}_{xy,i}\cdot\boldsymbol{r}_{xy}} \tag{1.13}$$

The fast evolving periodic Bloch function $u_i(\boldsymbol{r})$ will be the same within the band and it differs only for conduction and valence bands. The slowly varying envelope function $v_{i,n_i}(\boldsymbol{r}) = \frac{1}{\sqrt{A}}\varphi_{i,n_i}(z)e^{i\boldsymbol{k}_{xy,i}\cdot\boldsymbol{r}_{xy}}$ differs for each subband. The matrix element can be separated into 2 parts;

$$\boldsymbol{M}_{if} = \boldsymbol{\varepsilon}_\gamma(\boldsymbol{r}) \cdot \langle u_i | \boldsymbol{p}_e(\boldsymbol{r}) | u_f \rangle \left\langle v_{n_i} \middle| v_{n_f} \right\rangle + \boldsymbol{\varepsilon}_\gamma(\boldsymbol{r}) \cdot \langle u_i | u_f \rangle \left\langle v_{n_i} \middle| \boldsymbol{p}_e(\boldsymbol{r}) \middle| v_{n_f} \right\rangle \tag{1.14}$$

The first term describes interband transitions and second term describes transitions between subbands in the same band.

1.7.1. Interband Transitions in Quantum Wells

When the periodic components of the initial and final states are different, i.e. transitions between conduction and valence band, the valence-conduction band dipole matrix element of the Bloch function $\boldsymbol{M}_{cv} = \langle u_c | \boldsymbol{p}_e(\boldsymbol{r}) | u_v \rangle$ dictates the interband polarisation selection rules, and the electron-hole overlap integral of the envelope functions $\boldsymbol{M}_{n_i,n_f} = \left\langle \nu_{n_i} \middle| \nu_{n_f} \right\rangle$ gives rise to selection rules concerning the electron and hole subband quantum numbers n_i and n_f. In most of the commonly used materials, such as GaAs, the electric dipole transitions between the conduction and valence bands are strongly allowed and $\boldsymbol{M}_{cv}$ is non –zero. Therefore the optical transition matrix is proportional to the overlap of the electron and hole states leading to the quantum number selection rule on $\Delta n = n_f - n_i$. The transition with $\Delta n \neq 0$ is usually weak and is strictly forbidden if Δn is an odd number because the overlap of states with opposite parities is zero. In this case the second term vanishes because $\langle u_c | u_v \rangle = 0$.

1.7.2. Inter-Subband Transitions in Quantum Wells

In the case of transitions between subbands, the initial and final states are in the same band, so the first term vanishes and second term describes the transition in equation (1.14). The overlap integral of the Bloch function $\langle u_i | u_f \rangle$ is unity for the same band, $i = f$, thus the dipole matrix element of the envelope functions $\langle \nu_i | \boldsymbol{p}_e(\boldsymbol{r}) | \nu_f \rangle$ describes the inter-subband transition. As the dipole matrix element vanishes for the electric field of light oscillating in the plane of the quantum well, it leads to the polarisation selection rule: the optical electric field must have a component perpendicular to the semiconductor layers in order to induce inter-subband absorption. This means normal incidence radiation will not be absorbed and hence the radiation must come in at an angle.

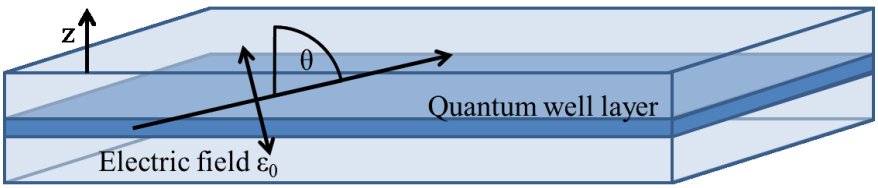

Figure 13: Optical beam of electric field ε_0 approaching the quantum layer with angle of incident between the growth axis (z) and the propagation direction of the optical radiation inside the material.

For a given angle of incidence θ between the growth axis and the propagation direction of the optical radiation inside the material, the electric field component interacting with the inter-subband transition is $\boldsymbol{\varepsilon}_z = \boldsymbol{\varepsilon}_0 \sin\theta$. The transition strength depends on the square of $\boldsymbol{\varepsilon}_z$ and is thus proportional to $\sin^2\theta$.

As the effective interaction path length increases by a factor of $\frac{1}{\cos\theta}$, we see that the absorption strength is proportional to $\frac{\sin^2\theta}{\cos\theta}$.

1.7.3. Light Trapping Techniques to Couple Light into Inter-Subband Transitions

Here we study quantum wells which have the advantage of a larger optical cross-section compared with quantum dots so that they can absorb photons effectively. However, as described in 1.7.2, a quantum well's inter-subband transition can only be excited by mid-IR light polarised in the quantum well direction (the growth direction) and is forbidden in the case of perpendicularly polarised light within our structures. The simplest way that light can be coupled into the inter-subband transition is via an oblique incident of radiation at Brewster's angle, as shown in Figure 13a). We can achieve inter-subband transition in this structure by fabricating a grating on the top or rear of the solar cell Figure 13d). For experimental purposes, we couple the light in from the side through a wedge, as suggested by West and Eglash,[55] which is shown in Figure 13b) and c). Ideally, by using Brewster's angle geometry, a large component of the optical electric field along the growth direction can be achieved and it is possible to couple IR-radiation to the inter-subband transition.

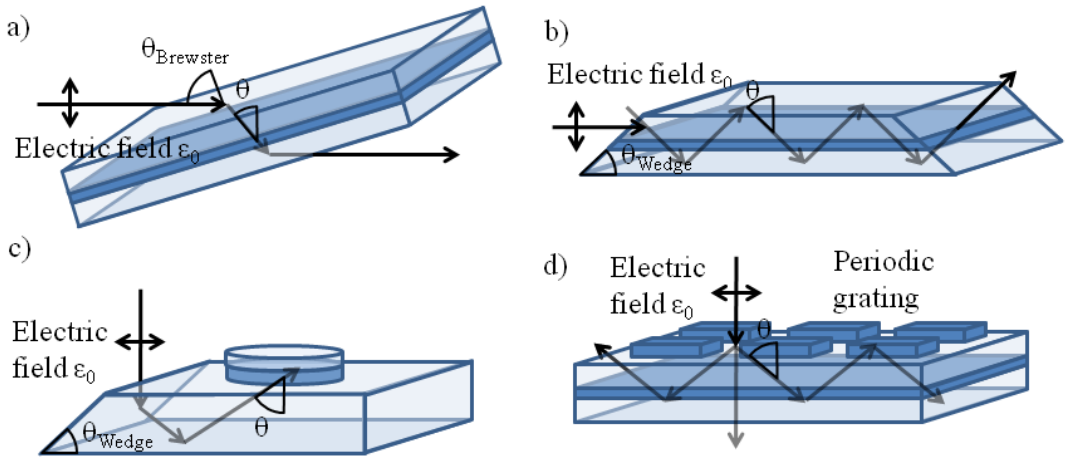

Figure 14: Different geomeries for coupling light into inter-subband transitions. a) Oblique-incident geometru with Brewster's angle b) Multipass waveguide c) Coupling into quantum well device on mesa d) two-dimentional grating

Chapter 2

Theoretical Analysis of the Photon Ratchet Intermediate Band Solar Cell

In this chapter, the theoretical study of an Intermediate Band Solar Cell (IBSC) is presented. Firstly we revisit the issues surrounding the realisation of conventional IBSCs and introduce our innovative new concept, the *Photon Ratchet* Intermediate Band Solar Cell (PR-IBSC), which we propose will increase the lifetime of carriers in the intermediate state - a necessary step towards achieving improved efficiency. As a parameter to examining the fundamental benefits of the PR-IBSC, we calculate the respective limiting efficiencies of a single bandgap solar cell, an IBSC and a PR-IBSC under idealised conditions. Through this comparison, we demonstrate that there is a fundamental efficiency gain that can be obtained, despite the loss introduced by the thermalisation of carriers. In order to explain the enhancement in efficiency, we investigate the fundamental sources of energy loss in these solar cells. The results of this work have been published in *Applied Physics Letters* in 2012 where we introduced the notion of the PR-IBSC for the first time. [43]

2.1 The Photon Ratchet Intermediate Band Solar Cell

The IBSC is an advanced concept in which the broadband solar spectrum is harvested more efficiently to overcome the single bandgap efficiency limit of 30% (known as the Shockley-Queisser limit).[15] By introducing a radiatively efficient but electrically isolated band between the conduction band (CB) and valence band (VB), additional photocurrent can be generated by the sequential absorption of two sub-bandgap photons, which would otherwise be unabsorbed, thereby reducing below-bandgap and thermalisation losses.[22] In principle, by introducing the intermediate band (IB), the current can be enhanced without significantly reducing the voltage, hence leading to higher conversion efficiency. There has been much experimental effort to realise such a device, such as by making the use of three-dimensional quantum dot superlattices. [37]

Marti et al reported an increase in photocurrent in a δ-doped InAs/(Al,Ga)As quantum dot system with continuous infrared light exciting carriers from the IB to the CB.[22] However, the photocurrent increase observed was as small as 10^{-2} % of the band-to-band value. A recent report by Okada et al also shows a small increase in quantum efficiency of 0.3% in a n-δ-doped InAs/GaNAs quantum dot solar cell, [23] while Sugiyama et al achieved 0.5% in a InGaAs/GaAsP strain-balanced quantum well

superlattice cell. [39] Kita et al reported proof of sequential absorption of photons via the IB in the form of bleaching and recovery of photoluminescence (PL) in InAs/GaAs quantum dots in an optical cavity. [40] They concluded that sequential absorption of photons was actually dominated by a two-photon process which can only occur with high optical excitation energy. [22]

As demonstrated in the literatures mentioned above, sequential absorption of the photons is possible in both quantum wells and quantum dots. However, the short excited-state lifetime of the carriers remains a critical problem in realising efficient IBSCs. In fact, all experimental reports on IBSCs show only a very weak effect due to the sequential absorption of photons, which generates a negligible gain in energy conversion efficiency. The short lifetime of electrons in intermediate states is mainly caused by fast non-radiative recombination that proceeds faster than all radiative processes.

In order to overcome this critical issue, some engineering to increase the lifetime of the excited electrons is essential. One way to do this is to introduce an irreversible or entropically-preferred one-directional process to move the excited carriers away from the recombination route. The PR-IBSC has an extra energy band, known as the ratchet band (RB), with energy less than the IB and which is decoupled from the VB. Strong thermal coupling between the IB and the RB means excited carriers in the IB quickly move to the low energy RB where the only recombination route back to the VB is via the IB. This theoretically reduces the recombination rate increasing the occupation of the RB and lifetime of the carriers. This should also increase the probability of the second excitation from the IB to the CB increasing the photocurrent. A comparison of the limiting efficiency between a PR-IBSC and an IBSC, as well as their fundamental loss mechanisms, is presented in the following sections.[43]

2.2 Limiting Efficiency Calculation

As discussed in chapter 1.3.3, there are two classes of loss mechanisms in a solar cell; intrinsic and extrinsic. Extrinsic losses are avoidable and can be minimised by improving the quality of solar cells. Although intrinsic losses are unavoidable, favourable designs of solar cells can reduce some of the loss mechanisms. The limiting efficiency calculation predicts an upper limit to the photovoltaic conversion efficiency of a device using the detailed balance model and only intrinsic losses are considered. Although this model is incomplete because it discounts extrinsic losses, it is a good measure of potential for solar cell design. In this section, the principle of the detailed balance model is explained and limiting efficiency calculations of single junction solar cells, IBSCs and PR-IBSCs are portrayed.

2.2.1 Detailed Balance Model [56]

Before starting the calculation, it is important to consider how to treat the source of the energy since the energy delivered by a solar cell depends on the incident light spectrum. The sun emits light over a wide range of wavelengths, covering ultraviolet, visible and infrared sections of the electromagnetic spectrum. Figure 15 shows various spectra relevant for photovoltaic technology. In theoretical work, it is common to use the black-body spectrum because this is described by a simple mathematical function and resembles the solar spectrum satisfactorily. Although the actual surface temperature of the sun is 5762K, the 6000K black-body spectrum (as well as 5762K) is often used. The black-body spectrum $BB(E)$ [W/m^2/J] at the temperature of the sun T_s and with geometric factor f_s, concentration factor C, is:

$$BB(E) = \frac{2Cf_s}{h^3c^2}\frac{E^3}{\exp\left(\frac{E}{k_BT_s}\right)-1} \qquad (2.1)$$

where h is Planck's constant, c is the speed of light in a vacuum and k_B is Boltzmann's constant. Power in the black-body spectrum of 5762K is $P_{solar} = 1355W/m^2$.[56]

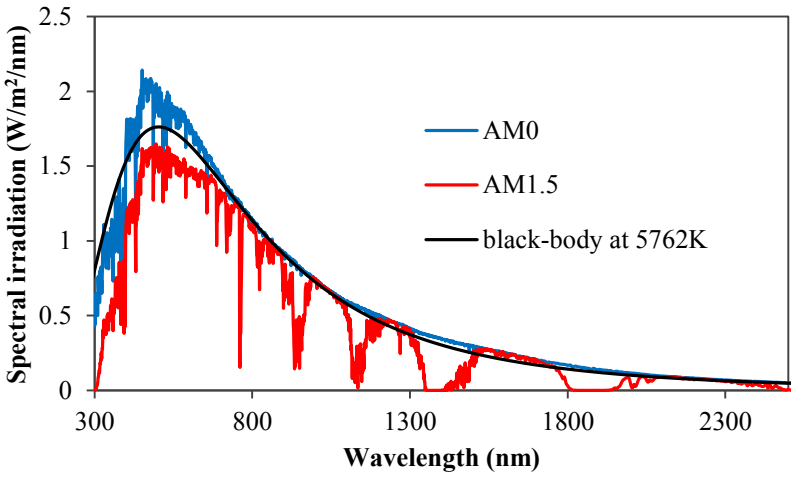

Figure 15: Spectra of sunlight relevant for PV-technology. AM0 is a spectrum outside of the atmosphere. AM1.5 is a spectrum at the surface of the earth corresponding to the sun being at an angle of elevation of 42°. Black-body spectrum is analytically obtained from equation (3.12) [57]

For modelling aimed at approaching the actual conditions under which a solar cell operates, the standard spectrum air mass 1.5 (AM1.5) is commonly used.[57] The AM1.5 spectrum is the solar spectrum after passing through 1.5 times the thickness of the standard atmosphere of the Earth and corresponds to the sun being at an angle of elevation of 42°. Similarly, the AM0 spectrum corresponds to the solar spectrum outside of the earth's atmosphere.

The detailed balance theory is widely used to calculate the limiting efficiency of photovoltaic concepts. The method was originally proposed by Shockley and Queisser in 1961.[15,10] In our model, we consider the solar cell to be a perfectly absorbing body, i.e. 100% absorption above the bandgap, and all of the absorbed photons create electron-hole pairs. However, an inevitable physical property of an absorbing body is that it is also an emitting body.

In this model, only optical transitions between bands are considered and the mobility is assumed to be infinite, allowing collection of carriers no matter where they are generated in the device. This means that by calculating the absorption flux and the flux emitted from the solar cell, the current generated by the solar cell is the difference between these two multiplied by the charge of electron q.

The absorption consists of two parts; one from the sun and the other from the other regions of the sky. Under maximum concentration, the optics render the conditions such that the entire surrounding of the solar cell is illuminated by radiation at the same temperature as the sun. Under conditions other than maximum concentration, one portion of the sky (shown in yellow in Figure 16) is illuminated by the sun, and the remainder is illuminated by a radiation source with the same temperature as the Earth. With 1-sun, the absorption étendue from the sun is $f_s = \frac{\pi {R_s}^2}{r} = 6.79 \times 10^{-5}$ where RS is the diameter of the sun and r is the radius of the Earth's orbit. At full concentration, $Cf_s = \pi$ where C is the concentration factor which has a maximum value of 46300. The emission étendue is $f_{cell} = \pi$ for any concentration.

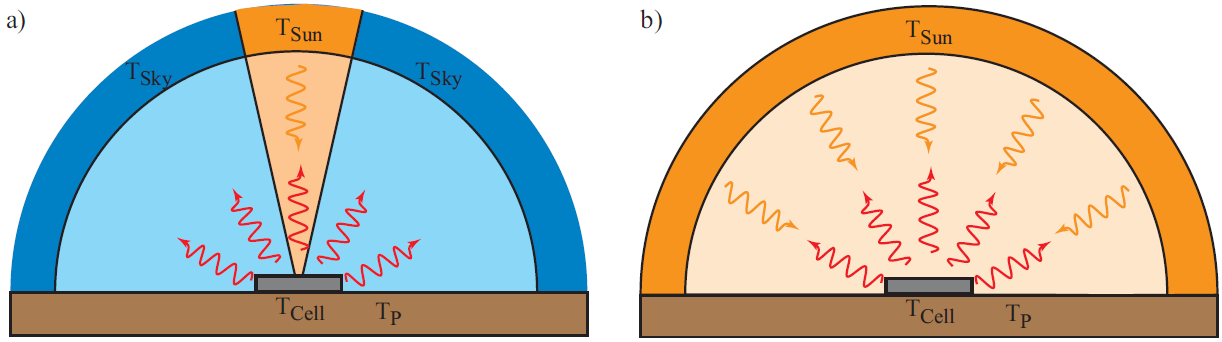

Figure 16: Solid angle of emission and absorption of a solar cell at a) 1-sun b) full concentration

In this model, we assume the temperature of the sun to be $T_{Sun} = 5762K$ and the temperature of the sky and the solar cells to be $T_P = T_{Cell} = T_{Sky} = 300K$.

If the absorption coefficient for a photon of energy E is given for a solar cell, the radiative generation rate of an electron-hole pair per unit volume per unit time is given by:

$$G = \frac{2f_s}{h^3c^2}\int_0^\infty \alpha(E)\frac{E^2}{\exp\left(\frac{E}{k_B T_s}\right)-1} + \frac{2(\pi - f_s)}{h^3c^2}\int_0^\infty \alpha(E)\frac{E^2}{\exp\left(\frac{E}{k_B T_P}\right)-1} \quad (2.2)$$

where f_S is an absorption solid angle from the sun, (π-f_s) is an absorption solid angle from the sky, and T_S, T_P are the temperatures of the sun and the sky respectively.

In solar cells under normal operation, the occupation of each band is described by the quasi-Fermi level. According to a generalised form of Planck's radiation law, the radiative recombination rate of an electron-hole pair per unit volume per unit time is given by:

$$R = \frac{2f_{cell}}{h^3c^2}\int_0^\infty \alpha(E)\frac{E^2}{\exp\left(\frac{E-\Delta\mu}{k_B T_{cell}}\right)-1} \quad (2.3)$$

where f_{cell} is an emission solid angle, $\Delta\mu = E_{F1}$-E_{F2} is the splitting between the quasi-Fermi levels and T_{cell} is the temperature of the device.

2.2.2 Limiting Efficiency Calculation of Single Junction Solar Cells

In single junction solar cells, the absorption coefficient is unity above the bandgap Eg and zero below. The population of conduction and valence bands is described by a corresponding quasi-Fermi level. At steady state, the particle number, i.e. number of electrons, in both the CB and the VB has to be conserved, while the difference between the generation and recombination rate multiplied by electron charge, must equal the current density J generated by the cell.

$$q[G - R] = J \quad (2.4)$$

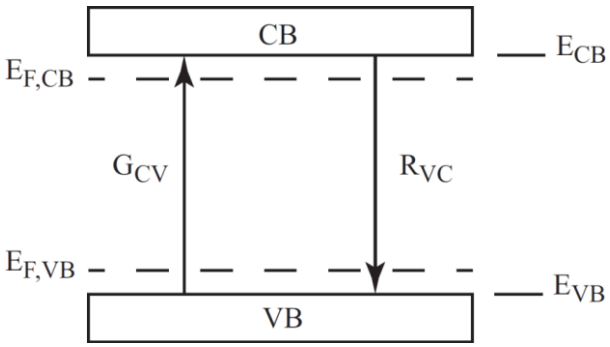

Figure 17: Energy diagram of single junction solar cell

By substituting equations (3.13) and (3.14), the current generated by the cell can be obtained.

$$J = \frac{2q}{h^3c^2}\left[f_s\int_{E_g}^{\infty}\frac{E^2}{\exp\left(\frac{E}{k_BT_s}\right)-1} + (\pi - f_s)\int_{E_g}^{\infty}\frac{E^2}{\exp\left(\frac{E}{k_BT_P}\right)-1} - f_{cell}\int_{E_g}^{\infty}\frac{E^2}{\exp\left(\frac{E-\Delta\mu}{k_BT_{cell}}\right)-1}\right] \quad (2.5)$$

where $\Delta\mu = qV$. Therefore the power generated by the solar cell is:

$$P = JV \quad (2.6)$$

and the conversion efficiency is:

$$\eta = \frac{P}{P_{solar}} \quad (2.7)$$

This equation is solved numerically using MATLAB and the maximum efficiency is 31.0% at $E_g = 1.30eV$ at 1-sun and 40.7% at $E_g = 1.10eV$ at full concentration.

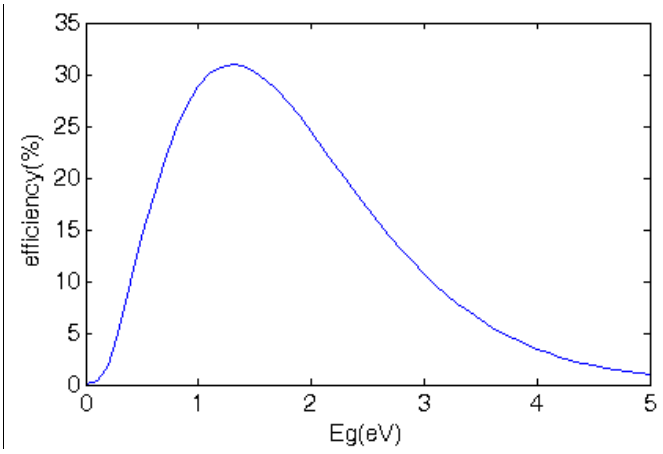

Figure 18: Efficiency of single junction solar cell as a function of bandgap Eg at 1-sun.

2.2.3 Limiting Efficiency Calculation of Intermediate Band Solar Cells

Following the same approach as a single junction solar cell, the limiting efficiency of an IBSC can be calculated. In this system, there are three recombination routes and three generation routes across three bandgaps: from the VB to the CB (E_{VC}); from the VB to the IB (E_{VI}); and from the IB to the CB (E_{IC}). As well as a unity absorption coefficient, good photon selectivity is assumed, which means that

there is no overlap between absorption of any transitions. The energy dependent absorption coefficient $\alpha(E)$ of IBSCs for the case where $E_{VI} > E_{IC}$ is shown in Figure 19.[58,59]

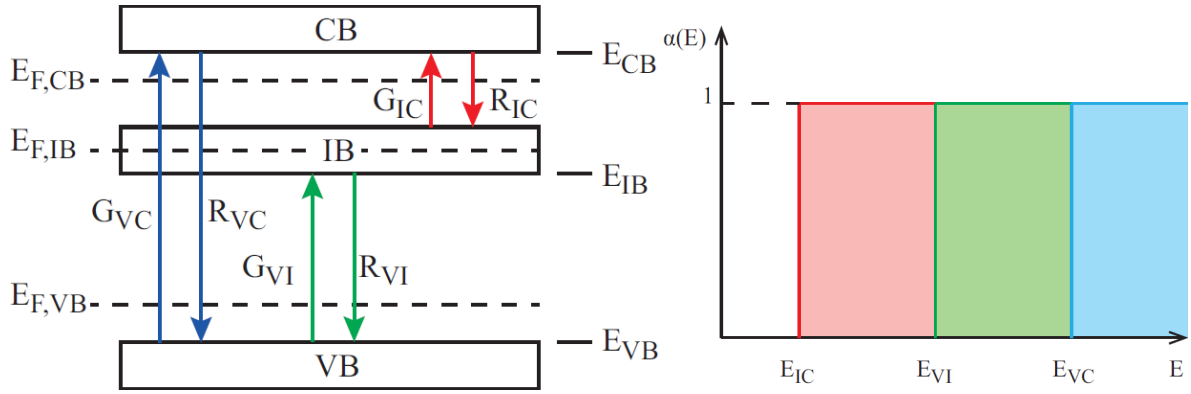

Figure 19: Energy diagram and absorption coefficient of IBSC.

The generation flux for a given sub-cell with lower absorption limit of E_a and higher absorption limit of E_b is given by:

$$G(E_a, E_b) = \frac{2f_s}{h^3c^2}\int_{E_a}^{E_b}\frac{E^2}{\exp\left(\frac{E}{k_B T_s}\right)-1} + \frac{2(\pi - f_s)}{h^3c^2}\int_{E_a}^{E_b}\frac{E^2}{\exp\left(\frac{E}{k_B T_P}\right)-1} \quad (2.8)$$

Similarly, the recombination flux for the same sub-cell with quasi-Fermi level splitting Δμ is:

$$R(E_a, E_b, \Delta\mu) = \frac{2f_{cell}}{h^3c^2}\int_{E_a}^{E_b}\frac{E^2}{\exp\left(\frac{E-\Delta\mu}{k_B T_{cell}}\right)-1} \quad (2.9)$$

The IB is assumed to be infinitely narrow, being at a level of state with energy E_{IB} rather than a band, and is electrically isolated. Therefore, the only escape route for the electrons in the IB is to be excited to the CB by absorbing photons or to fall down to the VB by emitting photons. At the steady state, the electron number in all bands must be constant which leads to the equilibrium flux equation for two sub-bandgap transitions.

$$G_{VI}(E_{VI}, E_{VC}) - R_{VI}(E_{VI}, E_{VC}, \Delta\mu_{VI}) = G_{IC}(E_{IC}, E_{VI}) - R_{IC}(E_{IC}, E_{VI}, \Delta\mu_{IC}) \quad (2.10)$$

The second equation required comes from the fact that the quasi-Fermi level splitting over the two sub-bandgaps must equal the total quasi-Fermi level split $\Delta\mu_{VC} = qV$.

$$\Delta\mu_{VC} = \Delta\mu_{VI} + \Delta\mu_{IC} \quad (2.11)$$

Solving equations (3.21) and (3.22) makes it possible to calculate the recombination rates since $\Delta\mu_{VI}$ and $\Delta\mu_{IC}$ can be found for any given V. Once the quasi-Fermi level splits are known, the current density can be calculated.

$$J = q(G_{VC} - R_{VC} + G_{IC} - R_{IC}) \tag{2.12}$$

The efficiency is then calculated following the same steps as for a single junction solar cell.

In Figure 20, the detailed balance efficiencies for the 5762K black-body spectrum at 1-sun are plotted for various bandgaps. The efficiency limits are 46.8% for 1-sun and 62.9% for full concentration.

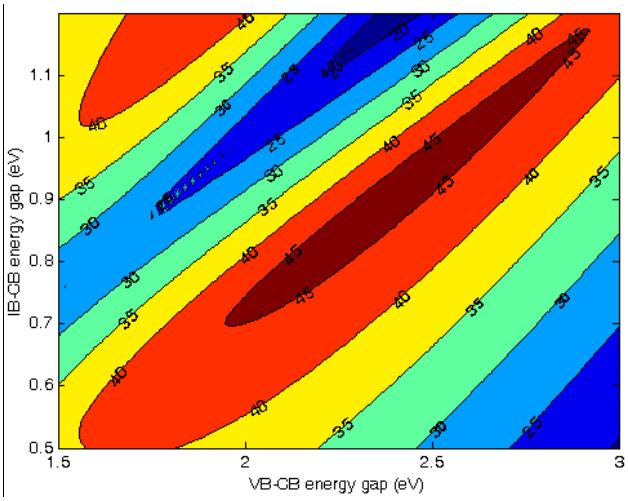

Figure 20: efficiency of IBSC at 1-sun 5762K blackbody for various bandgap energies E_{VC} and E_{VI}.

2.2.4 Limiting Efficiency Calculation of Photon Ratchet Intermediate Band Solar Cells

The 'photon ratchet' IBSC has the ratchet level introduced just below the IB in order to enhance conversion efficiency by increasing the lifetime of the intermediate state. This energy drop ΔE enables the rapid relaxation of carriers into the ratchet level, so the lifetime of the ratchet state can be very long provided the ratchet level is not coupled radiatively to the VB. Similarly, the IB also needs to be isolated from the CB in order to supress the direct recombination route. [43]

If we assume the rapid thermal exchange of electrons between the IB and the ratchet level, they reach thermal equilibrium with each other and share a single quasi-Fermi level E_{FIB}, as shown in Figure 21. As for conventional IBSCs, the IB is considered to be infinitely narrow in energy and there is no overlap between absorption of any band. Figure 21 shows the energy dependent absorption coefficient for three bandgaps in the case of $E_{VI} > E_{RC}$.

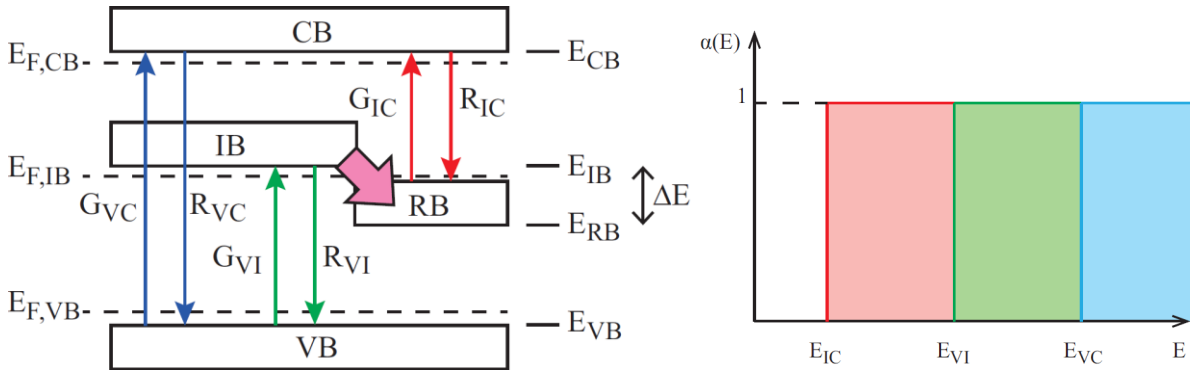

Figure 21: energy diagram and absorption coefficient of PR-IBSC for each sub-cells. [43]

The generation and recombination flux for each bandgap is identical to that of a standard IBSC, i.e. equations (3.19) and (3.20). Since the IB and ratchet level is electrically isolated, the net generation rates over the sub-bandgaps must equal each other.

$$G_{VI}(E_{VI}, E_{VC}) - R_{VI}(E_{VI}, E_{VC}, \Delta\mu_{VI}) = R_{RC}(E_{RC}, E_{VI}, \Delta\mu_{IC}) - G_{RC}(E_{RC}, E_{VI}) \quad (2.13)$$

The second equation required is the same as for the conventional IBSC (3.22) and comes from the notion that the quasi-Fermi level splitting over the two sub-bandgaps must equal the total quasi-Fermi level split $\Delta\mu_{VC} = qV$.

$$\Delta\mu_{VC} = \Delta\mu_{VI} + \Delta\mu_{I,C} \quad (2.14)$$

Solving equations (3.24) and (3.25) makes it possible to calculate the recombination rates and subsequently the current density which is given by:

$$J = q(G_{VC} - R_{VC} + G_{RC} - R_{RC}) \quad (2.15)$$

Again, the efficiency can then be calculated via the same method as for the single junction solar cell.

The limiting efficiency of the device with energy drop of $\Delta E = 270meV$ for the 5762K black-body spectrum at 1-sun is plotted in Figure 22. Even with the energy drop, which fundamentally is a loss, the limiting efficiency is increased from 46.8% to 48.5%. [43]

In Figure 23, the globally optimised limiting efficiency of the PR-IBSC for various energy drops ΔE is plotted at different concentrations. It can be seen that the gain in efficiency reduces as the concentration is increased and the fundamental limit of 62.9% is reached at full concentration where no efficiency gain is possible with the introduction of the photon ratchet. This result proves that the PR-IBSC is a fundamentally beneficial concept.

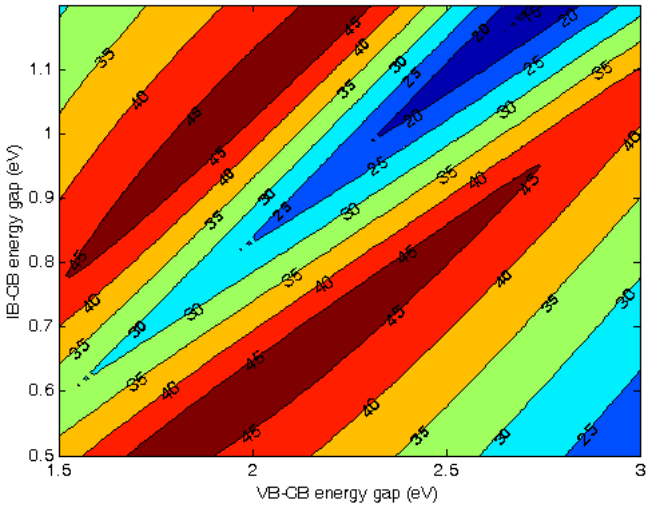

Figure 22: limiting efficiency of PR-IBSC with energy drop of $\Delta E=270meV$ at 1-sun 5762K blackbody for various bandgap energies E_{VC} and E_{VI}.

To understand this result we first note that the IBSC is a constrained implementation of a 3-threshold photovoltaic device. Maximum efficiency is always obtained with three, independent solar cells with no constraint on cell voltage and current flow, giving the device the freedom to operate each sub-cell at its maximum power point. As discussed earlier, the IBSC is constrained in current and voltage as shown in Equations (3.28) & (3.29).

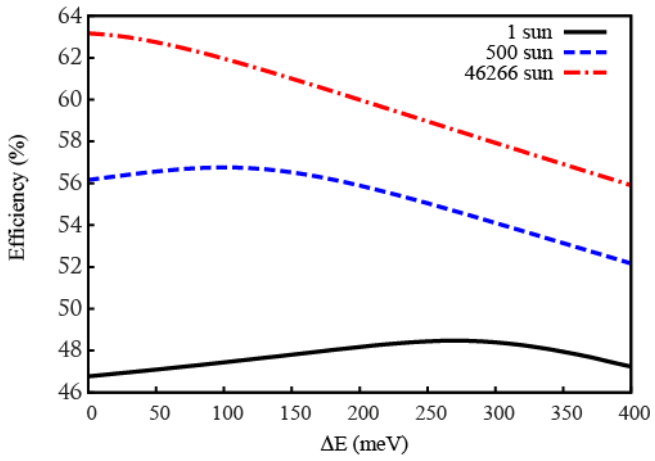

Figure 23: maximum energy conversion efficiency of PR-IBSC as a function of ratchet band energy ΔE at 2 different solar concentration factors; 1 sun, 500 sun and 46266 sun (full concentration). [43]

The introduction of the ratchet band therefore affects all of the recombination rates in the system and the generation rates, G_{VI} and G_{IC}. Figure 24(a) illustrates the variation in efficiency and recombination rates R_{VI}, R_{IC} and R_{VC} at the maximum power point as a function of ratchet band energy ΔE. Maximum efficiency occurs when the rates R_{VI} and R_{IC} are similar, at which point the total recombination rate $R_{VI} + R_{IC} + R_{VC}$ is at a minimum. However, at full concentration, the same quantities plotted in Figure 24 (b) show that the introduction of the ratchet serves only to increase the recombination rates in the solar cell. This change in the total recombination rate (i.e. the rate of

photon emission) is an important factor in understanding the fundamental efficiency gain in an IBSC through the introduction of the RB. More detail on this is presented in section 3.2.

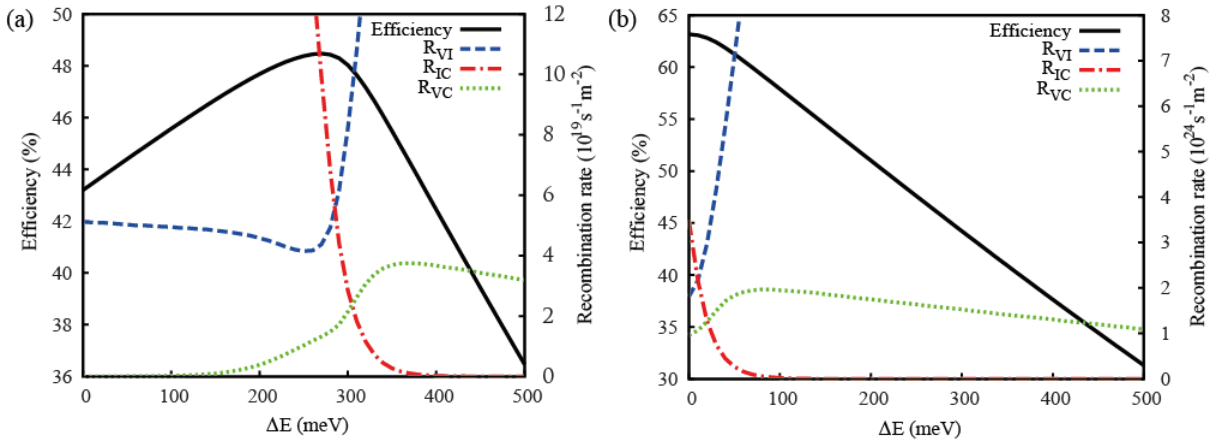

Figure 24: Efficiency of photon ratchet IBSC and recombination rates R_{VI} and R_{IC} as a function of ΔE with bandgaps fixed at maximum efficiency point, a) $E_{VC} = 2.10eV$ and $E_{VI} = 1.42eV$ at 1-sun and b) $E_{VC} = 1.96eV$ and $E_{VI} = 1.24eV$ at full concentration. [43]

2.2.5 Limiting efficiency calculation with non-radiative term

In real solar cell devices, the excitation and recombination routes can be non-radiative as well as radiative. Non-radiative excitation and recombination includes thermal excitations in which carriers are excited by absorbing phonons (quanta of thermal energy of lattice) and thermal recombinations where carriers recombine losing energy to phonons. This is often caused by energy states within the bandgap created by impurities and defects in the lattice (localised states). The localised states, which extend in momentum space, can capture carriers effectively and trap them, enhancing the thermal transitions. This process often reduces the radiative lifetime of the carriers and reduces efficiency of the photovoltaic devices.

Our limiting efficiency calculation of photovoltaic devices, described in the previous sections, ignores the possibility of the non-radiative process. However, it is important to consider this process in order to estimate the realistic energy conversion efficiencies. It has been suggested to estimate the non-radiative recombination rate using the radiative efficiency of each material system which is defined by:[60]

$$\eta_{rad} = \frac{J_{radiative}}{J_{radiative} + J_{non-radiative}} \tag{2.16}$$

where $J_{radiative}$ and $J_{non-radiative}$ are currents corresponding to radiative and non-radiative process recombination respectively. The radiative recombination is bimolecular and can be described as:

$$J_{radiative} = J_{01}\left(e^{qV/kT} - 1\right) \quad (2.17)$$

while the non-radiative recombination is dominated by monomolecular recombination (Shockley-Read-Hall):

$$J_{non-radiative} = J_{02}\left(e^{qV/2kT} - 1\right) \quad (2.18)$$

The efficiency of a single-junction solar cell as a function of bandgap is plotted for different radiative efficiencies in Figure 25.

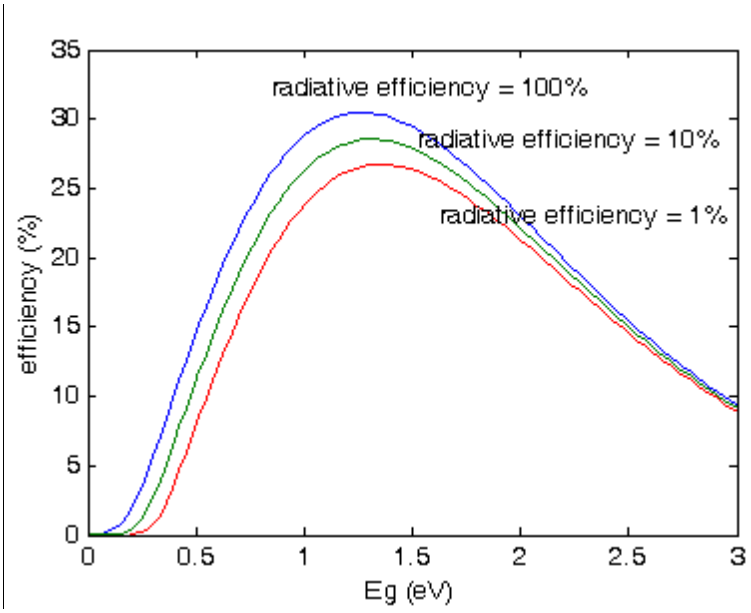

Figure 25: Efficiency (%) vs Eg (eV) of single-junction solar cell for different radiative efficiency.

The conversion efficiency decreases with the radiative efficiency but even with the radiative efficiency of 1%, the efficiency remains over 25% at the maxima.

In both a conventional IBSC (system A) and a PR-IBSC, non-radiative recombination is considered for all possible routes (3 recombination routes).

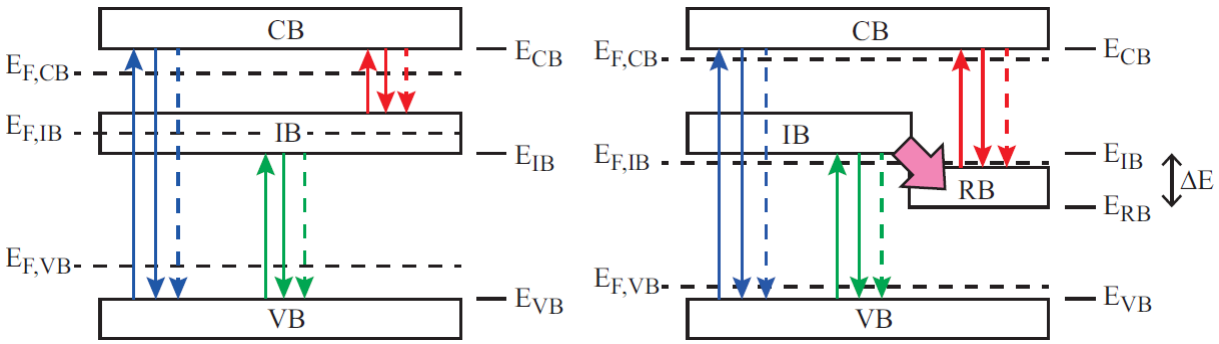

Figure 26: schematic energy diagram of IBSC and PR-IBSC with 3 routes of non-radiative recombination.

The efficiency as a function of radiative efficiency is plotted for a set of fixed bandgaps: $E_{VI} = 1.42eV$, $E_{VC} = 2.10eV$ and $\Delta E = 270meV$ (which is an optimum for PR-IBSC at 1sun)

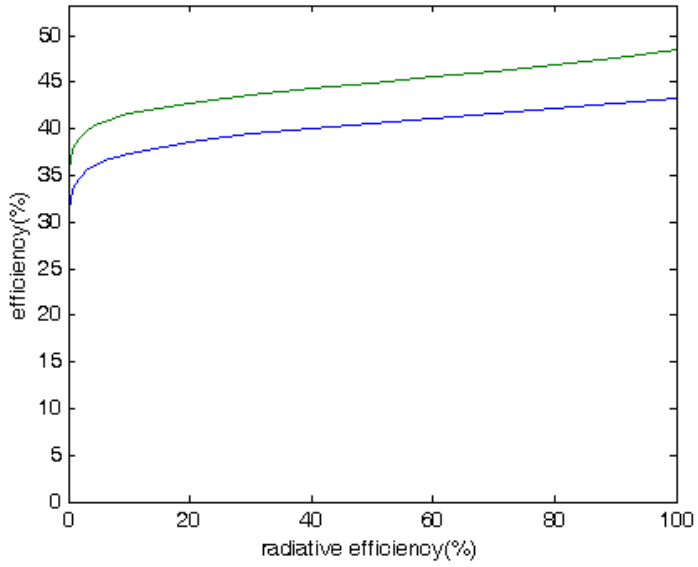

Figure 27: Efficiency (%) vs radiative efficiency (%) of IBSC (blue line) and PR-IBSC (green line) at full concentration, with fixed bandgaps and 3 non-radiative recombination routes.

Again, the conversion efficiency decreases with radiative efficiency and reaches zero at the point where the radiative efficiency equals zero. Similar results have been obtained for different bandgap combinations and it can be seen that the efficiency of PR-IBSCs is always higher than the efficiency of the conventional IBSC.

Next, we consider only 1 recombination route for both conventional and PR-IBSCs. The recombination route from the IB to the VB is what we are aiming to suppress by introducing the photon ratchet.

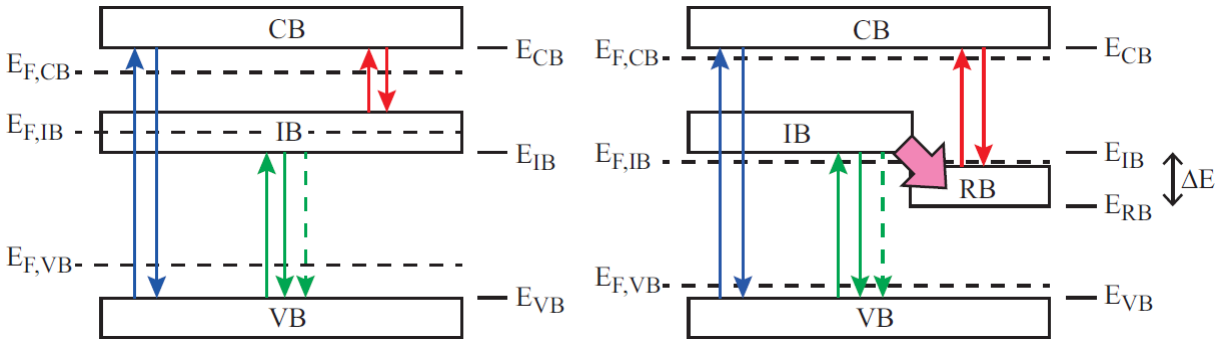

Figure 28: schematic energy diagram of IBSC and PR-IBSC with one route of non-radiative recombination.

As for the 3 channels, at the optimum bandgaps for PR-IBSCs at 1-sun, the photon ratchet improves the efficiency for any value of radiative efficiency. In this scenario, the conversion efficiency remains

positive even at zero radiative efficiency, the value of which is close to that of a single junction solar cell with bandgap $E_g = E_{VI}$.

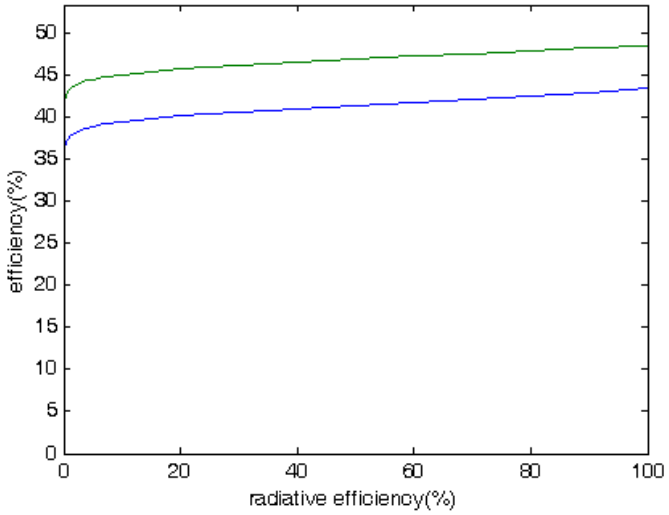

Figure 29: Efficiency (%) vs radiative efficiency (%) of IBSC (blue line) and PR-IBSC (green line) for fixed bandgaps with only 1 recombination route.

From the simulation, we can conclude that the non-radiative recombination by itself does not kill the conversion efficiency of the IBSC. What may be more important to consider is the variation in absorption when the occupation of the IB is changed, meaning the absorption coefficient decreases as the IB is filled.

2.3 Fundamental Loss Calculation

In order to understand the fundamental benefit of PR-IBSCs, it is important to know exactly where the efficiency gain is generated; in other words, which of the loss mechanisms are suppressed by the introduction of the ratchet band. In this section, the details of the fundamental loss mechanisms are discussed and the percentage contribution of each loss is calculated for both with and without photon ratchet band. The comparison of the results enables deeper understanding of the concept.

2.3.1 Fundamental Losses in Solar Cells

As mentioned previously, the performance of a solar cell is limited by extrinsic and intrinsic loss mechanisms. Extrinsic loss can be minimised by improving the quality of the device but intrinsic losses are unavoidable and this limits the efficiency of a single junction solar cell to 31.0% under 1-sun illumination.[15,16]

There are five intrinsic loss processes in solar cells as mentioned in section 2.1.3. Energy loss due to each mechanism can be calculated by using the following equations: [17]

1. Below-bandgap loss: Figure 7(5) – When an incident photon has energy lower than the bandgap of the semiconductor, it cannot be absorbed and does not contribute to electrical power. The loss amount is calculated by integrating the solar energy spectrum with photon energy below the lowest bandgap of the subcells, between the IB and the CB or between the VB and the IB, depending on the position of the IB in the IBSC shown in Figure 19.

$$f_s \int_0^{E_g} \frac{E^3}{exp\left(\frac{E}{kT_s}\right) - 1} dE \tag{2.19}$$

   This value increases as the bandgap E_g increases, because the solar cell becomes transparent to a wider range of wavelengths.

2. Thermalisation loss: Figure 7(1) – A photon with higher energy than the bandgap will be absorbed creating an electron-hole pair. However, the electron and hole lose part of their excess energy in the form of phonons to reach thermal equilibrium with the lattice. Total energy lost through this process is calculated by subtracting the number of absorbed photons multiplied by the bandgap energy from the total energy of the photons absorbed.

$$f_s \int_{E_g}^{E_{upper}} \frac{E^3}{exp\left(\frac{E}{kT_s}\right) - 1} dE - Egf_s \int_{E_g}^{E_{upper}} \frac{E^2}{exp\left(\frac{E}{kT_s}\right) - 1} dE \tag{2.20}$$

   This value is expected to decrease as the absorption range i.e. $E_{upper} - E_g$ decreases, because the energy range in which thermalisation occurs decreases.

3. Emission loss: Figure 7(3) – Some of the electron-hole pair recombines radiatively emitting photons. Energy lost through recombination is determined by the bandgap energy multiplied by the number of emitted photons.

$$Egf_{cell} \int_{E_g}^{E_{upper}} \frac{E^2}{exp\left(\frac{E - eV}{kT_{cell}}\right) - 1} dE \tag{2.21}$$

   This value is expected to increase with the corresponding cell voltage V and decrease as bandgap E_g increases.

4. Voltage loss: Figure 7(4) – the electron and hole lose some of their energy at the contacts. There is a reduction in voltage from bandgap ($V < \frac{E_g}{e}$) due to intrinsic thermodynamical loss (Carnot loss), mismatch in absorption and emission solid angle (Boltzmann loss) and

restrictions of voltage and current (series and parallel connection of sub-cells). By multiplying the voltage loss per electron by the current produced by the cell, we can determine the total energy loss:

$$\left(\frac{E_g}{e} - V\right)J = (Eg - eV)\left[f_s \int_{E_g}^{E_{upper}} \frac{E^2}{exp\left(\frac{E}{kT_s}\right) - 1} dE - f_{cell} \int_{E_g}^{E_{upper}} \frac{E^2}{exp\left(\frac{E - eV}{kT_{cell}}\right) - 1} dE\right] \quad (2.22)$$

This value decreases as the concentration is increased because of the reduction in the Boltzmann loss, which is the free energy lost through the emission of photons over a wider solid angle compared to that of incoming photons.

The respective contributions of each of these loss mechanisms in a single bandgap solar cell with $E_g = 1.1eV$ at 1-sun are graphically represented in Figure 6.

2.3.2 Fundamental Losses in Intermediate Band Solar Cells and Photon Ratchet Intermediate Band Solar Cells

The contribution of all 4 loss mechanisms are compared between IBSCs and PR-IBSCs with fixed bandgaps E_{IB} and E_{CB} for 1-sun and full concentration respectively. The bandgaps of the IBSC and PR-IBSC are fixed at the globally optimised values of $E_{IB} = 1.42eV$ and $E_{CB} = 2.10eV$ for both cells and a ratchet step of $\Delta E = 270meV$ introduced for the PR-IBSC for 1-sun. The contribution of thermalisation, emission and voltage losses are individually derived for each subcell and the below-bandgap loss was calculated for the subcell with the lowest bandgap. At full concentration, the bandgaps are fixed at $E_{IB} = 1.19eV$, $E_{CB} = 1.88eV$ and $\Delta E = 270meV$, which are the global optima for this condition. [55]

Figure 30 shows the breakdown of fundamental losses in IBSCs and PR-IBSCs at 1-sun concentration. The increase in the below-bandgap loss and the decrease in the thermalisation loss are due to the increase in magnitude of the lowest bandgap of the sub-cells. The introduction of the photon-ratchet level results in an increase in the sum of below-bandgap and thermalisation losses (-2.4%). However, the reduction of photon emission, which has been examined in detail in subsection 2.2.4, leads to the simultaneous decrease in the voltage and emission losses (+7.7%). Therefore, the overall losses are decreased at 1-sun, where the Boltzmann loss is significant, resulting in an increase in efficiency

(+5.3%). What is surprising is that the efficiency of an optimum photon ratchet IBSC surpasses that of an optimum IBSC.

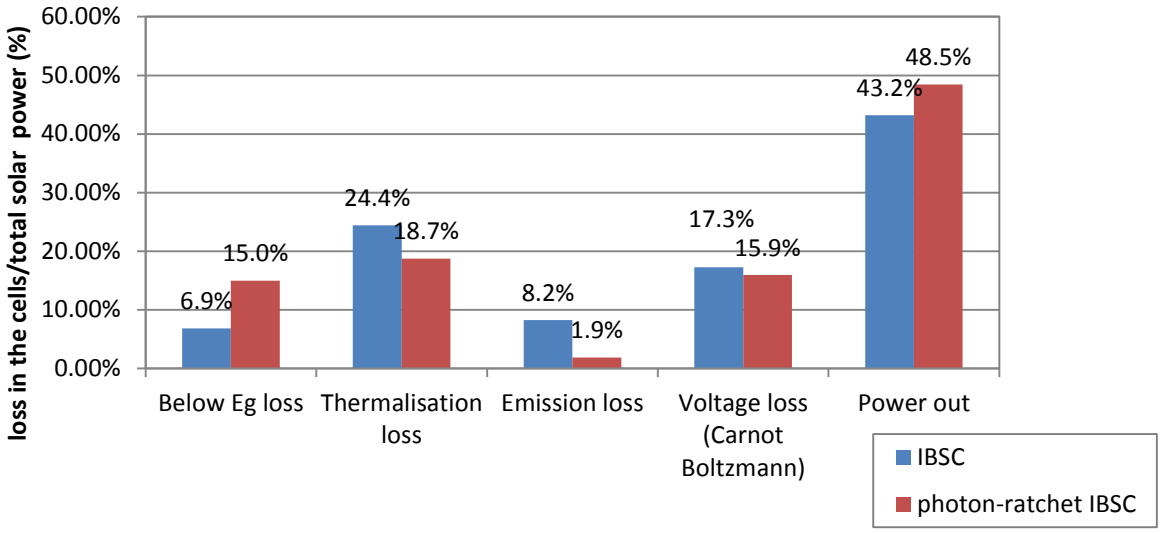

Figure 30: fundamental losses in IBSC and PR-IBSC at 1-sun concentration of bandgaps: $E_{IB} = 1.42eV$ and $E_{CB} = 2.10eV$ for both cells and ratchet step $\Delta E = 270meV$ for PR-IBSC.

However, at full concentration, the introduction of the ratchet serves only to increase the recombination rates in the solar cell, as was discussed in subsection 2.2.4. At this condition, the Boltzmann loss is zero and there is no significant voltage loss to compromise the below-bandgap and thermalisation loss due to the photon-ratchet step. Therefore, the introduction of a ratchet step results in an overall efficiency loss.

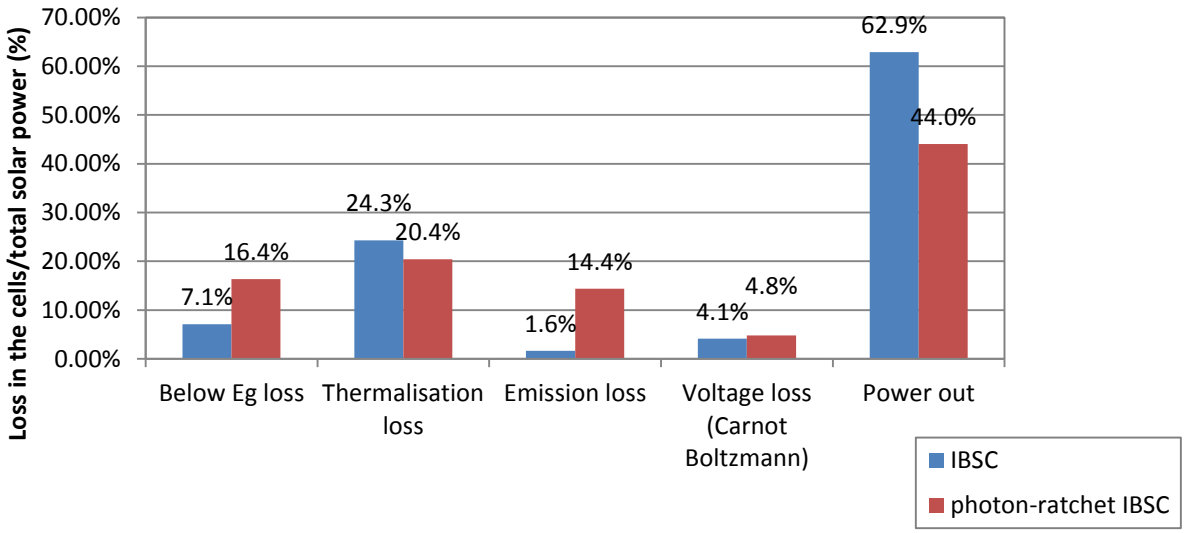

Figure 31: fundamental losses in IBSC and PR-IBSC at full concentration of bandgaps: $E_{IB} = 1.19eV$, $E_{CB} = 1.88eV$ and $\Delta E = 270meV$.

In addition to the fundamental benefits of introducing a ratchet band, there are also practical advantages. The conventional IBSC suffers from efficiency loss due to the short lifetime and low occupation factor in the IB. Introducing the ratchet serves to extend the lifetime of the intermediate band and ensures that the two carrier-generating transitions pump electrons from the occupied ground states into vacant excited states. Hence, introducing a ratchet band is an important component for realising efficient operation of a multi-band solar cell, such as the IBSC.

In terms of implementing the PR-IBSC, there are a number of existing materials which are strong candidates. Photon ratchet states can be separated in momentum space by using an indirect bandgap semiconductor, [44] where electrons are first excited into a direct IB state, followed by a relaxation down via phonon emission to an indirect photon ratchet state, which is at lower energy and separated by momentum k from the IB state. Since the recombination from the indirect photon ratchet state to the VB requires simultaneous multiple phonon emission, the radiative emission from the photon ratchet state is weak. A radiatively isolated state can also be found in a molecular system as a triplet state where transition to singlet ground state is forbidden,[45, 46] and in ferromagnetic compounds. [47] The PR-IBSC can also be implemented in quantum well and quantum dot systems by spatially separating the carriers using type-II structures. In such systems, the photo-generated electrons and holes rapidly separate into separate positions in the lattice, reducing the strength of both radiative and non-radiative recombination processes; hence the lifetime of the carriers can be extended. [51,53,52] We note that theoretical calculation of the type-II "ratchet" quantum dots IBSC predicts an enhancement in efficiency[61] and the same would apply for the type-II "ratchet" quantum well IBSC. The next challenge is to implement a prototype structure and to enhance the conversion efficiencies by extending the carrier lifetime in an IBSC.

2.4 Summary

In this chapter, the limiting efficiency of a new concept for IBSCs, the PR-IBSC, has been calculated and compared to that of a more traditional IBSC. It was shown that there is a fundamental gain by introducing the RB at 1-sun condition, due to the reduction in Boltzman losses through the suppression of photon emission. More importantly, there are greater advantages in introducing the RB in real IBSCs as the non-radiative recombination dominates the recombination route and the carrier lifetime of the IB is low. The extension of the electron lifetime in the excited states is key to successfully building a working IBSC with efficiency gains and the PR-IBSC offers a realistic way of achieving this. One way to accomplish this is to introduce a type-II quantum well and in the next chapter, quantum well devices are experimentally studied, with evidence presented proving that they would be suitable structures for building such devices.

Chapter 3

Basic Characterisation of Devices and Experimental Studies of Quantum Well Solar Cells

As a part of this project, we aim to design the possible structure of a Photon Ratchet IB Solar Cell (PR-IBSC) and experimentally prove the concept. In order to achieve the desirable energy levels and rapid transfer of electrons from the intermediate band (IB) to the ratchet level, a quantum cascade structure may be suitable. Before designing and testing the photon ratchet structure, it is important to experimentally confirm that quantum wells are suitable structures to create the intermediate state. This can be tested by observing the photocurrent due to the sequential absorption of two photons via the IB which typically arises from the confined states of the electrons in the conduction band potential.

In this chapter, some of the characterisation methods of potential materials and devices are described and results of initial experiments using existing samples are evaluated.

3.1 Optical and Electrical Characterisation

Before attempting to measure the photocurrent due to sequential absorption of sub-bandgap photons or making more advanced measurements, it is essential to characterise the device by measuring its optical and electrical responses. The performance of a solar cell device depends on many factors and experimental samples used for fundamental investigations of solar cell properties must be fabricated using high quality material and good electrical contacts, in order to increase the chances of obtaining reliable and accurate measurements with minimal background noise.

The basic characterisation of a processed device starts with the measurement of its dark-IV profile, from which the electrical performance of the device can be obtained. Within this project, this measurement was performed on all devices on all headers and a couple of the best performing headers consisting of good consistent devices with least leakage current, were selected. Following this, a bias-dependent external quantum efficiency (EQE) measurement was performed on the selected devices to identify the opto-electrical response of the sample.

For a device with a quantum well, it is also important to check the energy levels of the two-dimensional energy bands which arise from the confinement to ensure the well has depth and width as designed. The optical transitions between the confined states can be identified using

photoluminescence (PL) measurement as well as EQE measurement. Details of the measurements and light sources available for the experiments are described below.

3.1.1 Light Sources

Different light sources are required in order to optically characterise samples of solar cell devices. For this project, a list of light sources that were available for the experiments is as follows:

Quartz halogen and xenon lamp with monochromator: The combination of quartz halogen and xenon lamp produces a broadband blackbody spectrum from UV to mid-IR. Together with a monochromator which has an optical grating and a set of filters, the output of the source will be monochromatic light at a wavelength selected by the position of the grating. Although the output is incoherent and low in optical power, it is sufficient for wavelength-dependent characterisation (such as EQE) of small devices.

Solar simulator: This unit closely reproduces solar radiation via a combination of lamps and filters. It is useful for testing devices under 1-sun condition such as light-IV.

Diode pumped solid state laser: This is a 532nm CW laser with 5W of optical power. It is useful to optically generate high carrier concentration in the device and also to pump the Ti:Sapphire laser (explained below).

Ti:Sapphire laser: Pumped by the diode-pumped solid state laser, a Ti:Sapphire laser produces CW near-IR radiation which can be tuned by changing the angle of a birefringent filter. As the photon energy tuneable range matches that of some GaAs based QW diodes, the laser is useful for interband carrier generation and as a photogeneration source for PL experiments.

Fianium super-continuum laser with acousto-optic tuneable filters (AOTF): An ultra-broadband supercontinuum radiation source produces a pulsed coherent broadband radiation with total optical power of 8W ranging from wavelengths of 400 to 2000nm. The repetition rate can be changed from 100kHz to 1MHz while the pulse width is fixed at 146ps.

Quantum cascade laser (QCL) – Lasertune: A pulsed mid-IR laser which covers a wavelength range of 6 to 10μm and which is suitable to be used as an inter-subband excitation source. Both the pulse width and repetition rate can be chosen individually, between 50 and 500ns for pulse width and up to 1MHz for the repetition rate, as long as the corresponding duty cycle does not exceed 5%.

By combining the above available sources, different types of optical characterisation and experiments can be performed on the samples.

3.1.2 Temperature Dependent Dark and Light IV

In order to check the electrical properties of the devices including the quality of the wafer and contacts, the dark-IV is measured at room temperature using a Keithley source meter which records current readings while applying a series of bias points. In order to characterise multiple devices efficiently, the measurement is automated using computer software communicated via an IEEE GPIB interface. A typical bias range is measured from reverse bias -2V to the some forward bias voltage below the bandgap where it reaches the compliant current to verify the diode behaviour. The forward current limit is normally set to 1mA which is large enough to determine the electrical characteristics of the device and small enough not to damage the thin gold wires typically used to connect the contact to the external circuit.

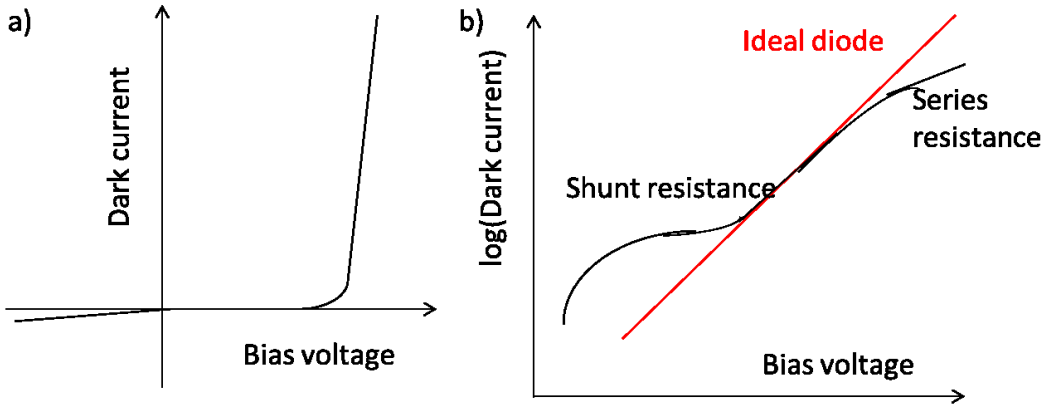

Figure 32: a) Dark-IV of typical diode. b) Logarismic plot of dark-IV of ideal diode and typical diode. Variation is caused by shunt and series resistances.

A typical dark-IV of a diode will look like Figure 32 a); when a reverse bias is applied to a diode, the depletion region of a pn-junction widens and the device acts as a resister, while at forward bias, the depletion region becomes smaller and a sudden increase in current takes place at some bias voltage points, where the carriers are injected into the depletion region or the intrinsic region and optical recombination of carriers takes place. A logarithmic plot of an ideal diode should show linear behaviour as seen in Figure 32 b) in red. However, in reality, a typical device will show some small leakage current both at forward and reverse bias caused by other routes of current flow and this can be represented with Shunt resistance in parallel to the diode.[14] At high forward bias, series resistance, which is caused by surface resistance and contact resistance, reduces the dark current.[62] These electrical characteristics of the diode are a good indication of the quality of the device. In most cases,

the series resistance and Shunt resistance is low and so devices show good behaviour; however, a high defect density, interface states and processing errors may lead to high resistance.

3.1.3 Temperature and Bias Dependent Quantum Efficiency

One way to investigate the optical response of a device is to measure its photocurrent due to illumination at a specific wavelength. The normalised wavelength-dependent photocurrent is represented by external quantum efficiency (EQE). A setup which can be used for EQE measurement is shown in Figure 33.

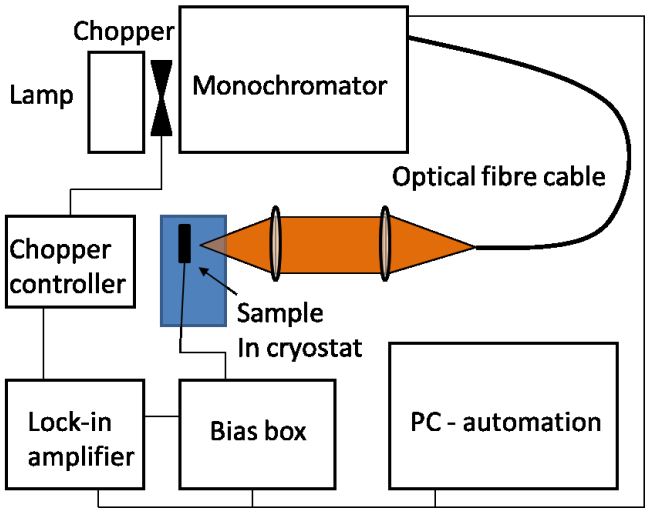

Figure 33: Schematic of the experimental setup of the external quantum efficiency measurement. Broadband radiation from a lamp is optically chopped, passed through a monochromator and directed towards the samples in a cryostat via optical fibre. The device, with applied bias voltage, generates photocurrent which is converted into voltage signal and only the relevant signal is recorded by PC after background signal is removed by the lock-in amplifier.

The light source, which consists of a quartz halogen bulb and a xenon lamp, emits broadband radiation covering some parts of UV all the way to mid-IR. In order to separate the signal due to the illumination from background light sources, the light is optically chopped at specific frequencies before it enters a monochromator, which selects a radiation wavelength range of a few nanometres using a grating and a set of filters. The monochromatic light then enters an optical fibre cable to be carried across the optical bench to be focused onto the sample by a combination of lenses. The sample is connected to a transimpedance amplifier, which consists of a voltage source, an operational-amplifier and a resister, and the photocurrent generated is converted into an amplified voltage signal. Only the component of the signal which is in phase with the frequency of the optical chopper is picked up by the lock-in amplifier and therefore only the photocurrent signal caused by radiation at the selected wavelengths is recorded. The result is recorded at different wavelengths to accumulate the

optical wavelength-dependent response of the device $J_{device}(\lambda)$ by sweeping the wavelength of the monochromated light controlled by an automation program communicated via the IEEE GPIB interface. By repeating the measurement on a reference Si diode of known optical response, $EQE_{reference}(\lambda)$, the EQE of the device under test $EQE_{device}(\lambda)$ can be calculated by using the equation:

$$EQE_{device}(\lambda) = \frac{J_{device}(\lambda)}{J_{reference}(\lambda)} EQE_{reference}(\lambda) \qquad (3.1)$$

where the $J_{reference}(\lambda)$ is the photocurrent response of the reference Si diode at wavelength λ.

The sample is mounted on a cold finger inside a cryostat which means the EQE measurement can be performed at different cryogenic temperatures. This is useful as the optical and electrical characteristic of the device will differ at different temperatures.

3.1.4 Photoluminescence

Photoluminescence measurement is another way of identifying the confined energy levels in both unprocessed wafers and processed devices. A schematic diagram of the experimental setup is shown in Figure 34. Photo-excitation of carriers takes place by illuminating a sample with a chopped laser light above the bandgap of the semiconductor generating electron-hole pairs in the conduction and valence bands respectively. The generated carriers quickly relax down to the band-edge of the semiconductor and the electron-hole pairs recombine, emitting photons. By collecting the emitted radiation and detecting it after it has passed through a spectrometer, the wavelength of the emitted photons can be determined along with the band-edge of the sample.

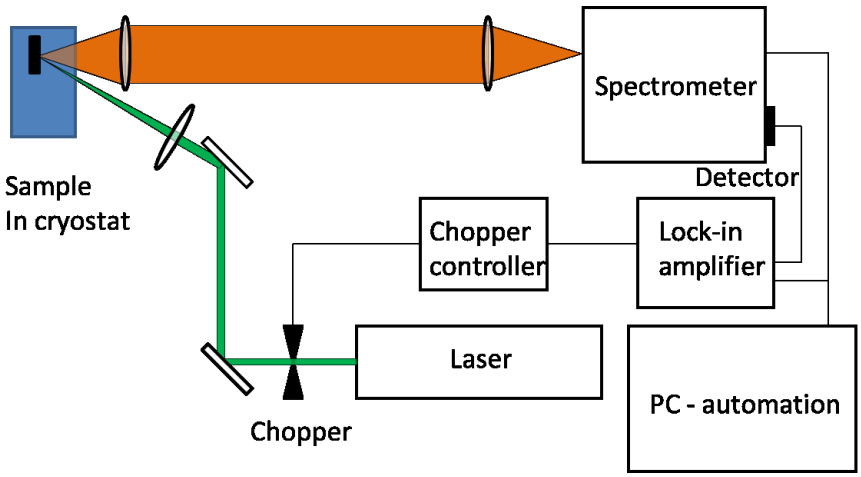

Figure 34: Schematic diagram of photoluminescent measurement. Optically chopped laser excite sample in cryostat generating carriers. They eventually recombine to emit photons and wavelength is determined by spectrometer.

In a quantum well device, the generated carriers near the well region accumulate at the lowest confined levels in both bands as this is energetically favourable. Therefore, the energy of the emitted photons corresponds to the energy separation between those confined levels and the photoluminescence is a useful tool to determine the quantum energy property.

Once the emission wavelength is determined, the detection wavelength is fixed and a signal is recorded while varying the excitation wavelength. This is known as a photoluminescence excitation (PLE) experiment and is a way to determine the absorption characteristics of the material and how strongly the absorbing states are thermally coupled to the emitting states.

3.2 Spectroscopy Setup

In order to fully characterise IBSCs, a spectroscopy measurement facility is required to have tuneable light sources with high optical power so that enough carriers can be photogenerated across the resonance wavelength of the transition. This tunability is required for both interband and inter-subband excitations which can change depending on the conditions of the experiment. It is also important to be able to obtain measurements at different temperatures below room temperature as the carrier dynamics will be different when thermal effect is minimised.

Figure 35 shows a full spectroscopic characterisation setup used in this project to perform optical experiments on quantum well IBSCs. There are several coherent light sources made up of a combination of those that are tuneable, fixed wavelength, high power, CW and pulsed. By combining these optical sources, it is possible to capture the electrical response of the device using computer software to control some parameters and acquire the results. This setup has been built up over the course of the project and through several improvements and modifications made as a result of extensive testing, most of the hardware and software is now in place and ready to be used for experimental study, as is described in chapters 4 and 5.

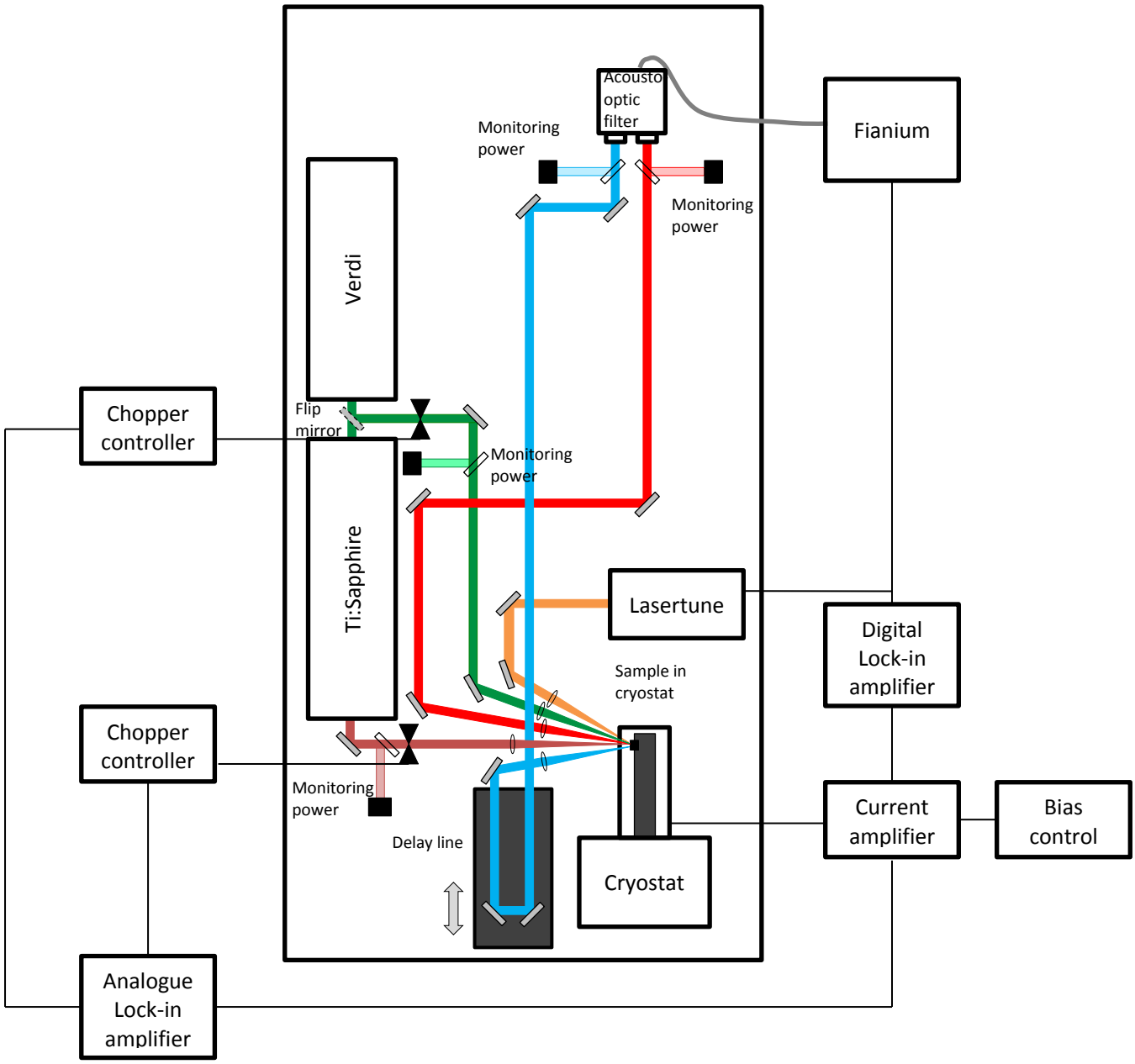

Figure 35: Full spectroscopic characterisation set up for IB solar cells

3.3 Sequential Photon Absorption via Intermediate Band

The single quantum well sample QT1168 used in this experiment is a p-i-n diode based on GaAs with a 7nm InGaAs quantum well in the i-region. The sample was originally fabricated using metal-organic chemical vapour deposition in the 1990s by J.S.Roberts at the University of Sheffield. The thickness of the intrinsic region is 319nm, while the p-type region is doped with $2.0 \times 10^{18} cm^{-3}$ carbon and the n-type region is doped with $1.0 \times 10^{18} cm^{-3}$ silicon (detailed data of QT1168 is described in Appendix A - 1).

Low temperature electroluminescence measurement was performed to determine the exact position of the IB in the quantum well. The result for sample QT1168 is shown in Figure 36, as the emission peak shifts with temperature.

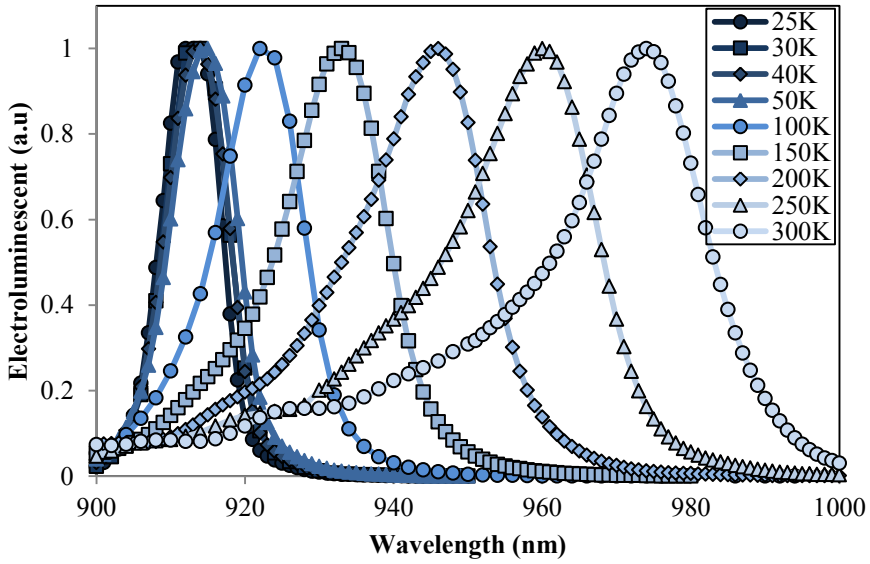

Figure 36: Normalised temperature dependent electroluminescence of QT1168 with applied bias of 1.5V. [38]

The data shows that the energy levels of the quantum well are temperature dependent and, as the temperature of the sample is lowered, the width of the thermal distribution of the carrier is reduced, resulting in sharper peaks. In Figure 37, the predicted transition wavelength from the VB to the IB is plotted using a k.p model, programmed by Dr D. J. Farrell, and is shown to vary between 920nm and 990 nm depending on its lattice temperature. These predicted transition wavelengths, when lattice strain is included, match well with the observed electroluminescence peaks in Figure 37.

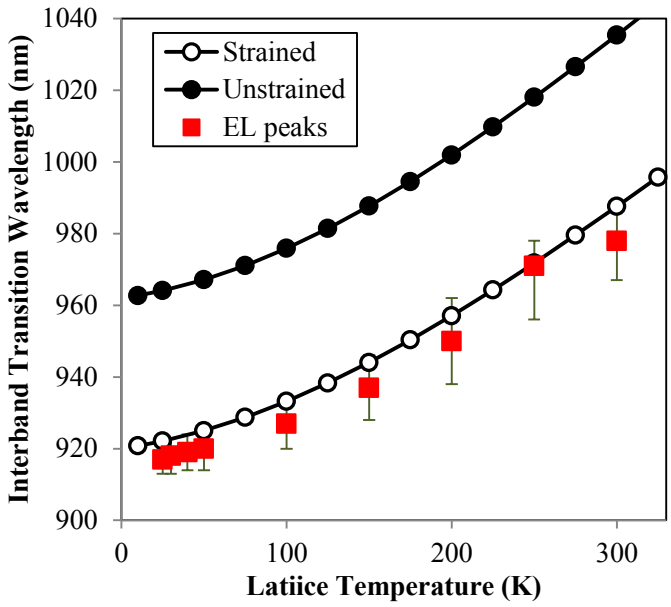

Figure 37: Wavelength of the interband transition of the sample predicted by the k.p model, with and without considering the lattice strain. The temperature dependent electroluminescence peaks from the sample (see Figure 36) are plotted in red. [38]

The temperature-dependent optical response is also seen in the EQE measurement of the sample, Figure 38. The result shows that as the temperature increases, the bandgap of the semiconductor decreases. This is caused by the increase in interatomic spacing due to the increased amplitude of the vibrations with the thermal energy.[63] As the interatomic spacing increases, the potential experienced by the electrons in the material decreases and therefore the bandgap energy also reduces. The relationship between bandgap energy E_g and temperature T can be described by Varshni's empirical expression:[64]

$$E_g(T) = E_g(0) - \frac{\alpha T^2}{T + \beta} \tag{3.2}$$

where $E_g(0)$ is the bandgap energy at $T = 0K$, α and β are fitting parameters characteristic of a given material. For example, for GaAs, $E_g(0) = 1.5216\, eV$, $\alpha = 8.871 \times 10^{-4}$ and $\beta = 572K$.[64] In this sample, the reduction of the bandgap is also affected by the strain due to the mismatch in the lattice constant.

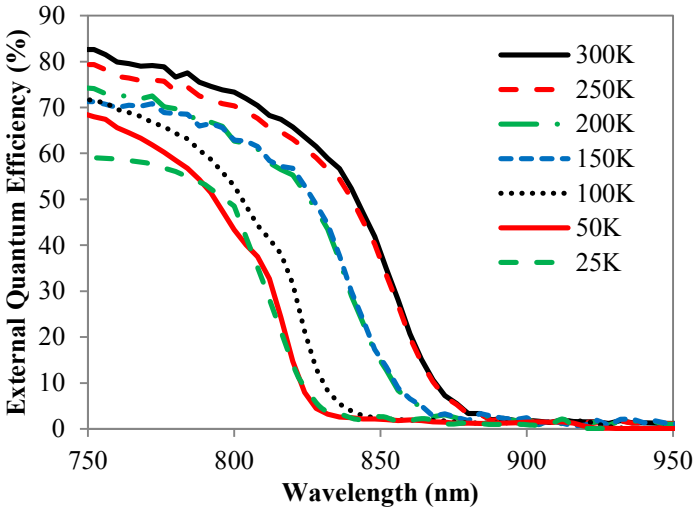

Figure 38: External quantum efficiency measurement of QT1168.

The optical response of the sample is also examined by measuring its current-voltage characteristics at different temperatures. In order to minimise the background photocurrent, the light IV measurement is taken at an illumination of 905nm such that carrier excitation takes place only in the quantum well, not in the bulk region. However, since the pn-junction device has a built-in voltage, carriers can escape from the well by tunnelling, and this generates measurable photocurrent even at low temperatures. The temperature variation in the short circuit current (zero bias point) is caused by the difference in effective density of states in the quantum well, corresponding to the fixed photoexcitation wavelength of 905nm, as well as variation in the carrier escape rate at different temperatures.[65,66]

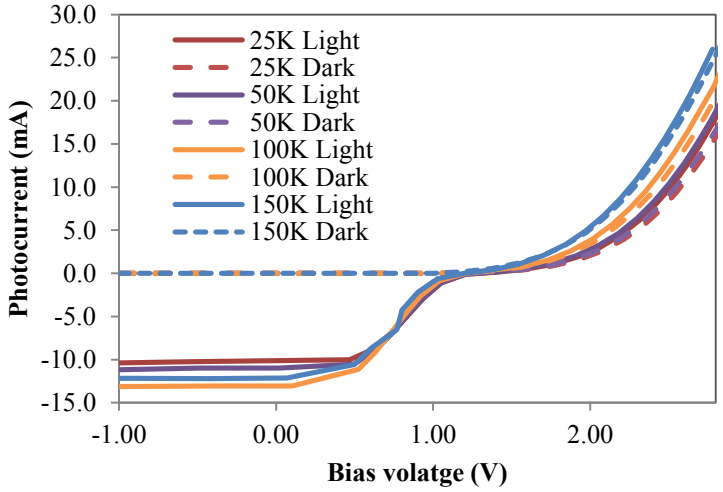

Figure 39: Light and Dark current voltage characteristics of QT1168. The light IV is taken with the sample illuminated at 905nm at a power of 120mW. [38]

When a forward bias is applied, the tunnelling rate of the carriers reduces and the photocurrent decreases, eventually reaching zero just below open circuit voltage.[65] Near this point, the IV curve has a flat region (at an applied bias of between 1.1V and 1.3V) in Figure 39. At this bias, carriers cannot escape via tunnelling and become trapped in the well.[65] The following experiment is performed at this bias condition so that there is no DC background current and the only photocurrent detected is due to the absorption of infrared photons.

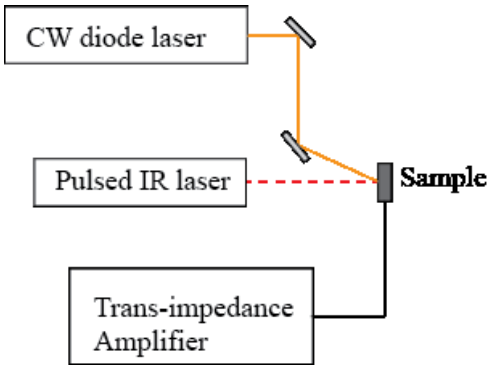

Figure 40: Experimental setup to observe sequential absorption of photons. The sample QT1168 is illuminated with continuous light populating the ground state of the quantum well. Inter-subband excitation pulsed radiation is coupled from the wedge while the photocurrent is observed using trans-impedance amplifier.

An electron can be excited from the VB to the lowest confined energy states in the CB potential well by absorbing a photon, followed by optical excitation to higher confined states or continuum states, where the electron can be extracted to the outer circuit. However, for this two-photon process to be efficient, the long wavelength photon must be absorbed while the electron is still in the confined state. The short lifetime (order of ns) of the excited electron in the IB means that it is necessary either to increase the lifetime of the electronic state in the IB or to increase the photon flux by using a high intensity of short wavelength radiation (usually mid-IR for III-V quantum structure) in order to be able to observe the photocurrent effectively.

An IR optical parametric generator (OPG) enables us to achieve a high intensity mid-IR radiation to pump the inter-subband transition in the quantum structure. The sample was illuminated with continuous 980nm diode laser light at room temperature populating the ground state of the quantum well. While carriers are continuously excited into the well, a 100ps pulse of light at 2.79μm, from an OPG with energy 2mJ and 3Hz repetition rate, was directed at the sample enabling the carriers trapped in the quantum well to escape and resulting in a photocurrent shown in Figure 41.

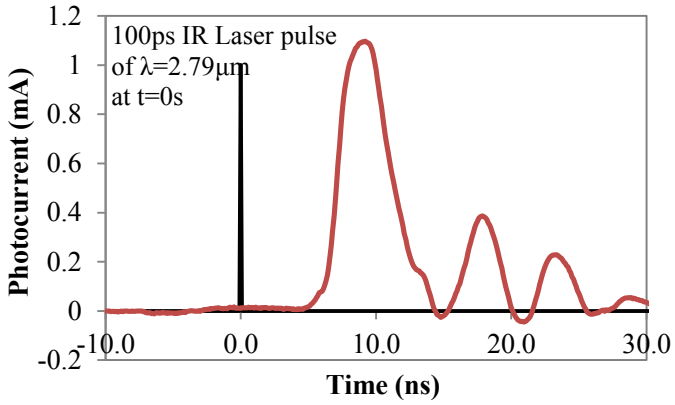

Figure 41: A transient photocurrent arising from sequential absorption of two photons in a quantum well structure when the sample QT1168 is illuminated by an IR laser pulse at t=0s. The oscillatory behaviour is ringing caused by incomplete impedance matching in the detection electronics. [38]

A clear observation of a two-photon photocurrent of 1.1mA in a single-quantum well structure has been obtained. [38] The oscillatory behaviour is known as ringing and is caused by incomplete impedance matching in the detection electronics. The delay of photocurrent enhancement is due to the combination of optical and electrical delays in the detection system. The result demonstrates that multiple photon absorption can be achieved in quantum well devices and offers a route to high efficiency power conversion in the future.

In order to study the sequential absorption of photons in quantum wells, the experiment needs to be repeated at low temperature, where the carrier will not have enough thermal energy to escape from the well without absorbing the second photon. At this condition, the background current is much lower and more precise and reliable measurement can be done. As demonstrated in EL and EQE measurements, the shift in the excitation peak means optical excitations to populate the ground state of the well requires a use of tuneable light sources and it is within the tuning range of the Ti:Sapphire laser at any cryogenic temperature. However, due to the long-term unavailability of the OPG laser through upgrade and servicing work, the inter-subband transition wavelength became temporarily inaccessible thus rendering the repetition of the experiment more challenging.

In the next chapter, we discuss a new set of samples that were designed during this project in order to achieve a transitional wavelength which is accessible by the set of lasers that are currently available.

3.4 Nitride Quantum Well Intermediate Band Solar Cells

A nitride quantum well sample N2139 was supplied by Sharp Laboratories Europe and studied in order to investigate if nitride quantum wells are suitable structures to create the intermediate state.

The ideal bandgap for an IBSC is close to 2eV which cannot be achieved with GaAs based quantum well structures. By using higher bandgap material such as GaN, the operation region of the IBSC can be shifted to the visible part of the spectrum and thus improve the efficiency.

As was the case for GaAs/InGaAs quantum wells, it is important to experimentally prove that GaN/InGaN quantum wells are suitable structures for creating intermediate states. Hence, the nitride quantum well sample N2139 (a single 2.4 nm $In_{0.2}Ga_{0.8}N$ well with an $Al_{0.1}Ga_{0.9}N$ barrier on a GaN substrate increasing confinement) must be tested by observing the photocurrent due to sequential absorption of two photons via the IB (detailed data of N2139 is shown in Appendix A - 2).

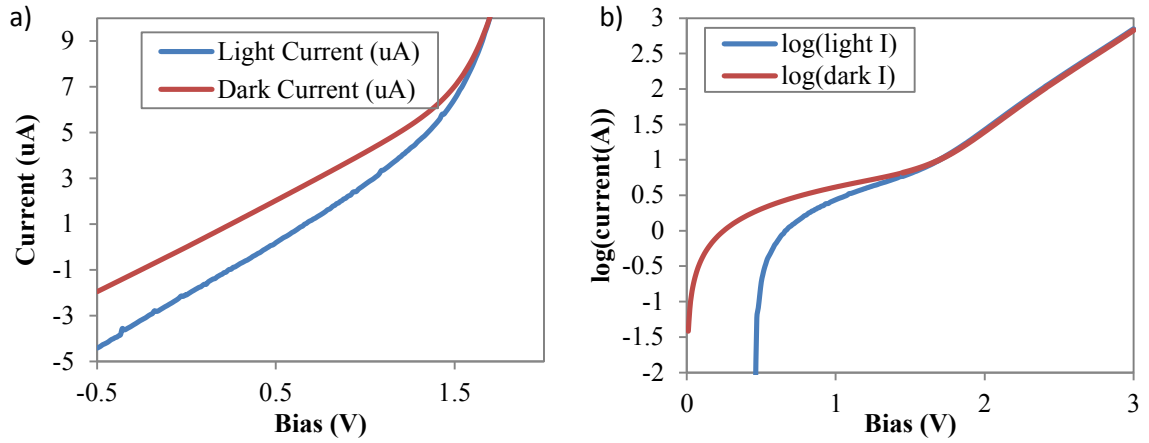

Figure 42: Dark and light current voltage characteristics of N 2139; a) on a normal scale showing poor fill factor and b) on logarithmic current scale showing presence of shunt and series resistances.

The device visibly emits light of wavelength centred on 540nm, with applied bias voltage of around 2.3V. However, the electrical power produced by the device is low: 243nW when illuminated by 309.7W/m^2 of broadband light.

The spectral response of the N2139 photocurrent is shown in Figure 43. The current decreases dramatically as the wavelength of the light exceeds that of the GaN barrier and it becomes negligible above 520nm. This indicates that even at room temperature, the well is deep enough so that the carrier excited into the well region does not have enough thermal energy to escape.

Electrical luminescence of N2139 shows bias dependency, since the emission peak shifts from 550nm to 520nm as bias is increased. The emission is from the ground state of the quantum well and forward bias acts against the built-in voltage raising the energy levels. By comparing the emission peak at low bias with the photocurrent, it can be seen that excitation of the ground state of the well does not contribute to photocurrent.

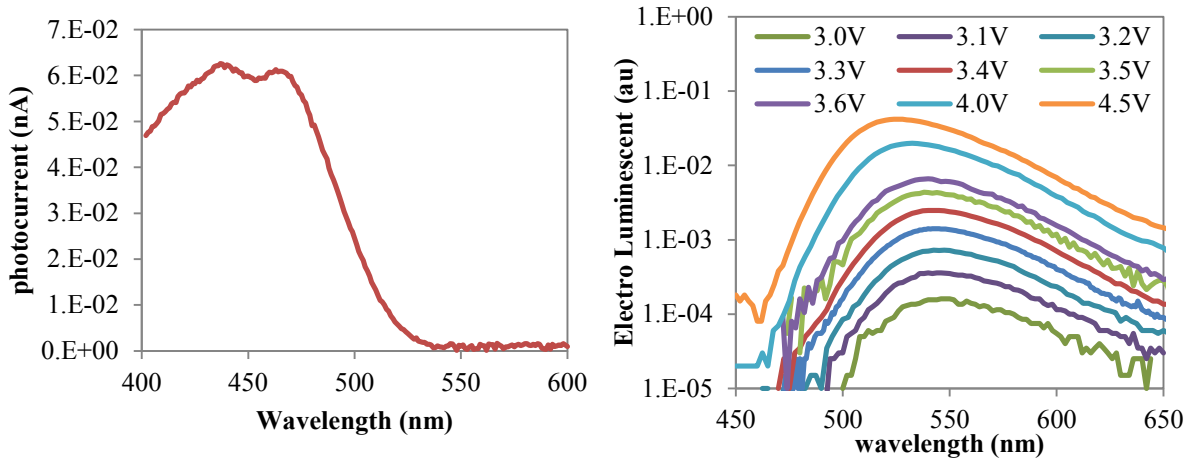

Figure 43: Photocurrent and electro-luminescence of N2139 at room temperature.

Further experimental study of the sequential absorption of photons in this nitride sample has proven to be challenging since the way it is processed is not suitable for solar cell operation. The high series and Shunt resistance means that there is high background current and measuring small changes in photocurrent proved to be impossible.

3.5 Summary

In this chapter, we have discussed preliminary experimental evidence to demonstrate that quantum wells are suitable structures for building IBSCs, through experimental work on existing samples. However, due to limitations in the properties of the samples that were available, there was a necessity to design a new set of samples which could be used to study the optical transitions in quantum well systems in more detail. We discuss our design work around the new samples in the following chapter.

Chapter 4

Spectroscopic Study of Inter-Subband and Interband Transitions in Quantum Well Solar Cells

In order to study optical transitions in quantum wells, it is important to characterise the interband and inter-subband transitions individually leading to the sequential generation process between confined energy levels. Both the carrier density-dependent strength of the transitions as well as the lifetime of excited carriers for required transitions are key factors in achieving Intermediate Band Solar Cells (IBSCs). In this chapter, we describe how n-i-n and p-i-n devices with an identical single quantum well were designed for this purpose, with the basic characterisation and possible future work on these samples also presented later.

4.1 Designing Samples

As per the previous chapter, in order to design a suitable quantum well structure with suitable transition energies, which were also accessible by our lasers, it was required to use quantum mechanical modelling of a semiconductor. Here, we first review theoretical quantum mechanics which form the basis of our work.

4.1.1. Basics of Quantum Mechanics [67,68]

De Broglie stated that particles such as electrons have wave properties and the frequencies and wave vectors of these "matter waves" would be related to the energy and momentum of the associated particle given by the de Broglie relations:

$$\begin{aligned} E &= \hbar\omega \\ \boldsymbol{p} &= \hbar\boldsymbol{k} \end{aligned} \tag{3.3}$$

where $\hbar = \frac{h}{2\pi}$ is Planck's constant. This wave-particle duality has been observed experimentally; for example, diffraction of electron through crystals.

The wave property of a particle moving under the influence of potential $V(\boldsymbol{r}, t)$ can be described by Schrödinger's equation:

$$i\hbar\frac{\partial}{\partial t}\Psi(\boldsymbol{r},t) = -\frac{\hbar^2}{2m^*}\nabla^2\Psi(\boldsymbol{r},t) + V(\boldsymbol{r},t)\Psi(\boldsymbol{r},t) \tag{3.4}$$

where $\Psi(\boldsymbol{r},t) = \psi(\boldsymbol{r})T(t)$ is a wave function of the particle and $\psi(\boldsymbol{r})$ is spacial and $T(t)$ is the time dependent part of the wave function. In a one-dimensional case, by separating time dependent and independent parts, it can reduce down to time independent Schrödinger's equation which describes the total energy E of a particle in this wave:

$$-\frac{\hbar^2}{2m^*}\frac{\partial^2\psi(x)}{\partial x^2} + V(x)\psi(x) = E\psi(x) \tag{3.5}$$

By solving the equation for a particular potential $V(x)$ and effective mass m^* (m_0 for an electron in a free space), the energy eigenvalue E and wave function $\psi(x)$ associated with the particle can be found. It is important to consider the following boundary conditions when solving the equation.

1. The wave function must be a continuous, single-valued function of position and time.
2. The integral of the squared modulus of the wave function over all values of x must be finite.
3. The first derivative of the wave function with respect to x must be continuous everywhere except where there is an infinite discontinuity in the potential.

4.1.2. Solving Schrödinger's Equation

The analytical solution to Schrödinger's equation only exists for certain potentials such as that of an infinite potential well. For most of the potentials $V(x)$, the equation has to be solved numerically to find energy eigenvalues E and the eigenfunctions $\psi(x)$.

a. Shooting method

The shooting method is a standard method to solve differential equations numerically. The second-order derivative is expanded in terms of finite differences as:

$$\frac{\partial^2\psi(x)}{\partial \mathrm{x}^2} \approx \frac{\psi(x+\delta x) - 2\psi(x) + \psi(x-\delta x)}{(\delta x)^2} \tag{3.6}$$

Substituting equation (3.4) into equation (3.3) leads to:

$$\psi(x+\delta x) = \left[\frac{2m^*}{\hbar^2}(\delta x)^2(V(x)-E) + 2\right]\psi(x) - \psi(x-\delta x) \tag{3.7}$$

Equation (3.5) implies that if the wave function is known at the two points $(x - \delta x)$ and x, then the value of the wave function at $(x + \delta x)$ can be calculated for any energy E. This iterative equation forms the basis of the shooting method. Using two known values of the wave function $\psi(x - \delta x)$ and $\psi(x)$, a third value $\psi(x + \delta x)$ can be predicted. Using this new point $\psi(x + \delta x)$ together with $\psi(x)$, a fourth point $\psi(x + 2\delta x)$ can be calculated, and so on. Hence the complete wave function can be deduced for any particular energy E. The solutions for stationary states have wave functions which satisfy the standard boundary conditions $\psi(\infty) \to 0$ and $\frac{\partial}{\partial x}\psi(\infty) \to 0$, as $x \to 0$.

b. Tri-diagonal method

Another method of solving the differential equation numerically is called the tri-diagonal method. If we consider variation in effective mass of electron $m^*(x)$, the one-dimensional time independent Schrödinger's equation (3.3) becomes:

$$-\frac{\hbar^2}{2}\frac{\partial}{\partial x}\left[\frac{1}{m^*(x)}\frac{\partial\psi(x)}{\partial x}\right] = [E - V(x)]\psi \tag{3.8}$$

Since the approximate form of the first-order derivative is:

$$\frac{\partial\psi}{\partial \mathrm{x}} \approx \frac{\psi(x + \delta x) - \psi(x - \delta x)}{2\partial \mathrm{x}} \tag{3.9}$$

equation (3.6) can be expanded and rearranged into:

$$\begin{aligned} -\frac{\hbar^2}{2\delta x^2}\frac{1}{m^*(x + \frac{\delta x}{2})}\psi(x + \delta x) \\ + \frac{\hbar^2}{2\delta x^2}\left[\frac{1}{m^*\left(x + \frac{\delta x}{2}\right)} + \frac{1}{m^*\left(x - \frac{\delta x}{2}\right)} + \frac{2\delta x^2}{\hbar^2}\right]\psi(x) \\ - \frac{\hbar^2}{2\delta x^2}\frac{1}{m^*\left(x - \frac{\delta x}{2}\right)}\psi(x - \delta x) = E\psi(x) \end{aligned} \tag{3.10}$$

This equation can be written in the form of a matrix equation:

$$\bar{\bar{H}}\bar{\psi} = E\bar{\psi} \tag{3.11}$$

where $\bar{\bar{H}}$ is a tri-diagonal matrix and $\bar{\psi}$ is a vector:

$$\bar{\bar{H}} = \begin{pmatrix} a_1 & b_2 & & & & & \\ b_2 & a_2 & b_3 & \cdots & & 0 & \\ & b_3 & a_3 & & & & \\ & \vdots & & \ddots & & \vdots & \\ & & & & a_{n-2} & b_{n-1} & \\ & 0 & & \cdots & b_{n-1} & a_{n-1} & b_n \\ & & & & & b_n & a_n \end{pmatrix}, \quad \bar{\psi} = \begin{pmatrix} \psi_1 \\ \psi_2 \\ \psi_3 \\ \vdots \\ \psi_n \end{pmatrix} \tag{3.12}$$

and each term is:

$$\begin{aligned} a_i &= \frac{\hbar^2}{2\delta x^2}\left[\frac{1}{m^*\left(x_i + \frac{\delta x}{2}\right)} + \frac{1}{m^*\left(x_i - \frac{\delta x}{2}\right)} + \frac{2\delta x^2}{\hbar^2}\right] \\ b_i &= -\frac{\hbar^2}{2\delta x^2}\frac{1}{m^*\left(x_i - \frac{\delta x}{2}\right)} \\ \psi_i &= \psi(x_i) \end{aligned} \tag{3.13}$$

where $x_{i+1} = x_i + \delta x$.

By numerically solving the diagonalisation of the matrix, energy eigenvalues and corresponding wave functions can be obtained. For example, the solution looks like Figure 44 for a single quantum well of finite depth.

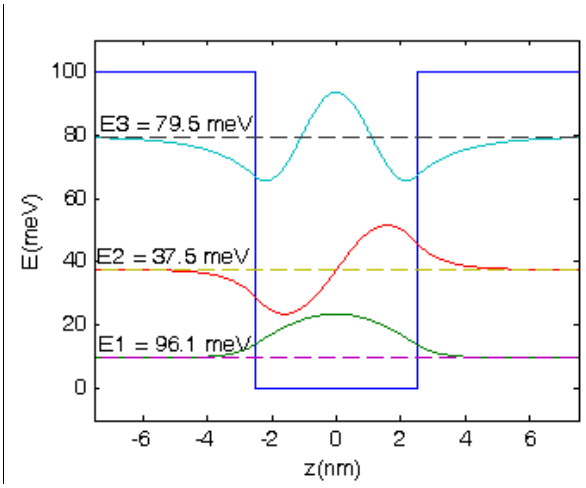

Figure 44: Energy eigen-values and corresponding wave function of a finite quantum well of depth 100meV and width 5nm calculated by tri-diagonal method.

Based on this model, a suitable structure can be designed using the commercially available software Nextnano[69], which is described in more detail in the following section.

4.1.3. Final Design for the Interband and Inter-subband Transition Study in a Quantum Well

We aim to design and fabricate samples specific to studying inter-subband and interband transitions in quantum wells one by one. By keeping the well and the material system the same for both, the transition wavelength should remain unchanged as the doping is changed.

The first device that is considered consists of an n-i-n sample with an embedded n-doped quantum well in the i-region, as pictured in Figure 45. With the electrical contacts both connected to the conduction band, this device acts as a photoconductor responding to inter-subband excitation. The purpose of this sample is to study inter-subband transition from the carriers available in the QW so that there is no need for photo-filling the state. The carrier density in the lower quantum state is known as it is defined by the n-doping density in the well region. By measuring the inter-subband transition rate, it is possible to produce a model to describe this transition, which will be essential for designing the PR-IBSC using quantum wells.

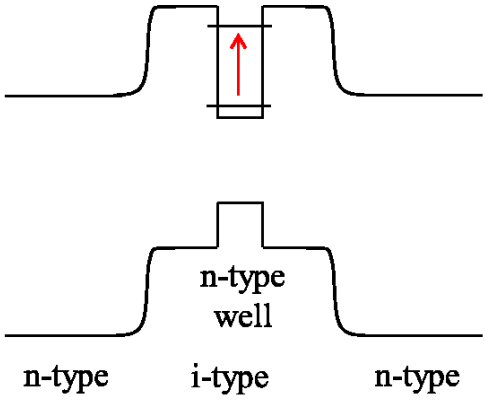

Figure 45: n-i-n sample with n-doped quantum well in the i region – to study inter-subband transition while from the carriers available in the QW due to doping.

The second device presented here is a p-i-n diode with an identical quantum well in the i-region, as shown in Figure 46. As the quantum well is identical to the first sample, the inter-subband transition should have equal characteristics and can be described using the same model. The only difference is that the quantum well is not doped meaning there are no carriers available in the lowest confined level and thus the transition requires carriers to be photo-generated. Through characterisation and measurements, a model can be established to describe the interband transition and when used in combination with the inter-subband model from the first sample, a full picture of the sequential absorption via the intermediate band, which arises from the quantum well, can be obtained.

Once the model is established, it is possible to predict the probabilities involved in this process, allowing for the estimation of the photocurrent resulting from the sequential absorption of subbandgap

photons for any given excitation power and set of conditions. Subsequently, experiments to measure this additional photocurrent caused by the inter-subband photons can be attempted to confirm this effect.

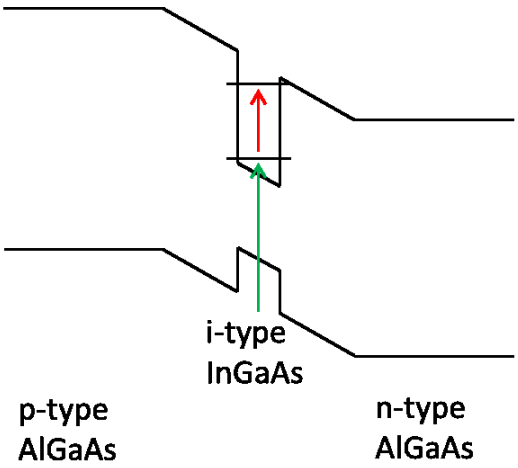

Figure 46: p-i-n sample with undoped quantum well in the i-region – full solar cell sample with the intermediate band. Sequential photon absorption will lead to excess photocurrent to be generated in the sample.

Each of these samples require a suitable reference to confirm any measurement is genuine and that it is caused by quantum well transitions and not by other effects such as free carrier absorption.

In order to design the samples described above, the commercially available software "Nextnano" was used to simulate the electronic and optoelectronic semiconductor nano-devices and materials for any given structure and conditions. It has a built-in database of group IV, III-V and II-VI materials along with their respective ternaries and quaternaries. The software consists of a quantum mechanical model based on a three-dimensional Schrödinger solver with the 8-band k.p model enabling the accurate designing of quantum dots and wires as well as quantum wells, including effect of strain caused by mismatch in lattice constants. A Poisson solver is also used in the model to take the carrier distributions into account, leading to a self-consistent Schrödinger-Poisson solver. (see Appendix B)

With the lasers that were available to us, the accessible wavelength range was 700-950nm for interband transitions and 6-10μm for inter-subband transitions. Through the use of the cryostat, the temperature of the device under test can be as low as 10K. Considering the variation may be caused by a small change in the material composition and well thickness in the growth process, the design chosen here was with transition wavelength at around 850nm and inter-subband transition at around 8μm at 10K.

Through adjustments made as a result of a series of simulations over several iterations, the final design for the quantum well consisted of 7nm of an $In_{0.05}Ga_{0.95}As$ well with $Al_{0.3}Ga_{0.7}As$ barriers. This led to an interband transition energy of 1.52eV (815nm) between H1 and E1 and an inter-subband

transition energy of 0.15eV (8.3µm) between E1 and E2 as shown in Figure 47. The wavelength does vary greatly with the applied bias across the quantum well region but the confinement and the transition energies remain within the accessible range.

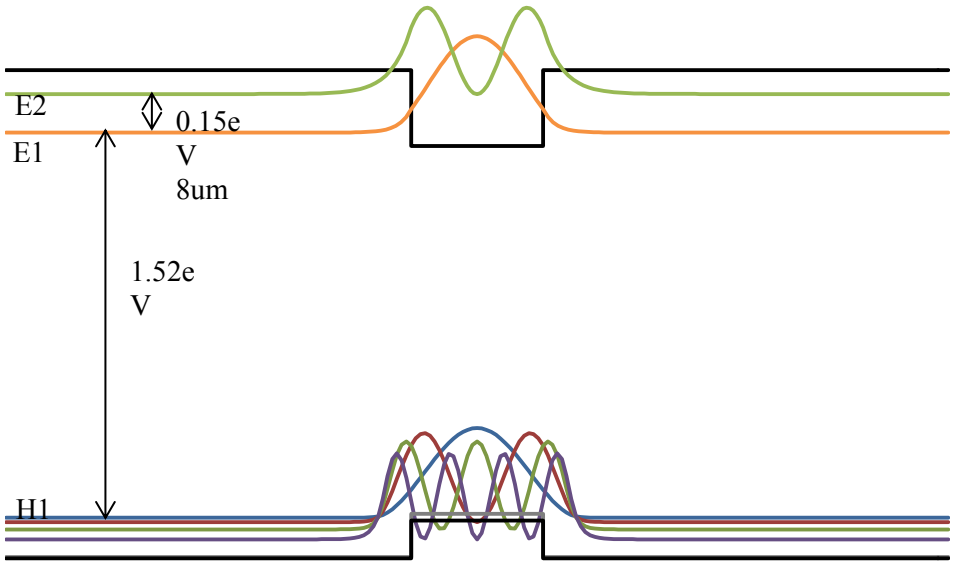

Figure 47: Schematic energy diagram of single quantum well with 7nm of In0.05Ga0.95As well and Al0.3Ga0.7As barriers, simulated using Nextnano.

The simulated energy diagram of the p-i-n diode sample with intrinsic quantum well looks like Figure 48a) and that of the n-i-n sample with an n-doped quantum well looks like Figure 48b).

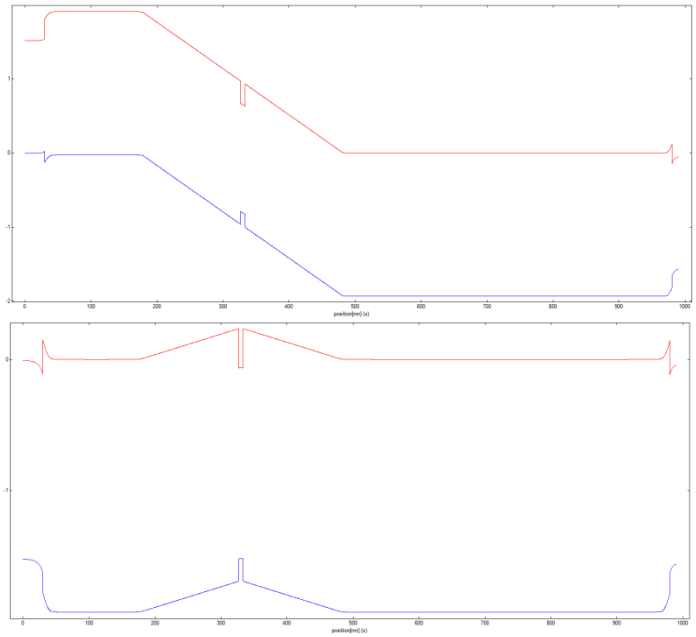

Figure 48: Simulated energy diagram of a) AlGaAs p-i-n diode with 7nm InGaAs quantum well and b) AlGaAs n-i-n sample with identical quantum well, simulated using Nextnano.

4.2 Growth and Processing

The samples were grown and processed at the EPSRC National Centre for III-V Technologies following the recent EPSRC funding for experimental and theoretical investigation on PR-IBSCs which started in June 2013. Dr Edmund Clarke took the role of growing all 4 samples using molecular beam epitaxy (MBE) and Dr Ken Kennedy performed the fabrication of the device, as well as the post-processing after their growth.

MBE is an advanced atomic-layer by atomic-layer crystal growth technique which requires an ultra high vacuum of less than $10^{-11} mbar$ and is based on the reaction of molecular or atomic beams with a heated crystalline substrate.[70] It is capable of producing extremely high purity and highly crystalline thin films with precise control over the composition, doping and interfaces in a fraction of the nanometer range in the growth direction. The molecular beam is produced by evaporation of elemental sources and with a growth rate of $\sim 1 \mu m/hr$, the composition and thickness of the layers is controlled by the temperature of the cells containing the source elements and by the opening and closing of shutters.[71] In-situ surface analysis is also possible via reflection of high energy electron diffraction. The sample wafer grown is characterised by photoluminescence measurements to make sure that the transition energy between the confined levels matches what has been predicted by the model before being processed into devices.

In order to couple the mid-IR radiation into the inter-subband transition of the quantum well, the radiation needs to go through several reflections inside the wafer. Normal solar cell devices are commonly grown on an n-doped substrate; however, a doped semiconductor has significantly higher free carrier absorption. Therefore, in order to minimise the absorption loss, the samples are grown on an intrinsic wafer. After the samples are made into the devices, they are mechanically processed with a bevelled edge from which inter-subband excitation can be coupled into the device, as shown in Figure 49. The IR light is deflected at the wedge into total internal reflection mode and reaches the active region with a component of polarisation which can excite inter-subband transitions.

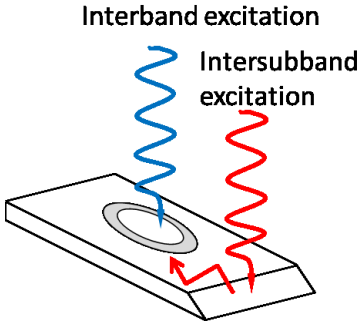

Figure 49: Schematic diagram of processed device

The samples are processed into the device using a mask to etch down part of the wafer forming mesas, as per Figure 50a). The etching is stopped at the n-type layer beneath the active device layer so that contact to the layer can be made. The top p-type layer (n-type for n-i-n sample) is electrically isolated from the n-type layer, so contact at the top of the mesas, along with lower contact on the n-type layer can be made as shown in Figure 50b).

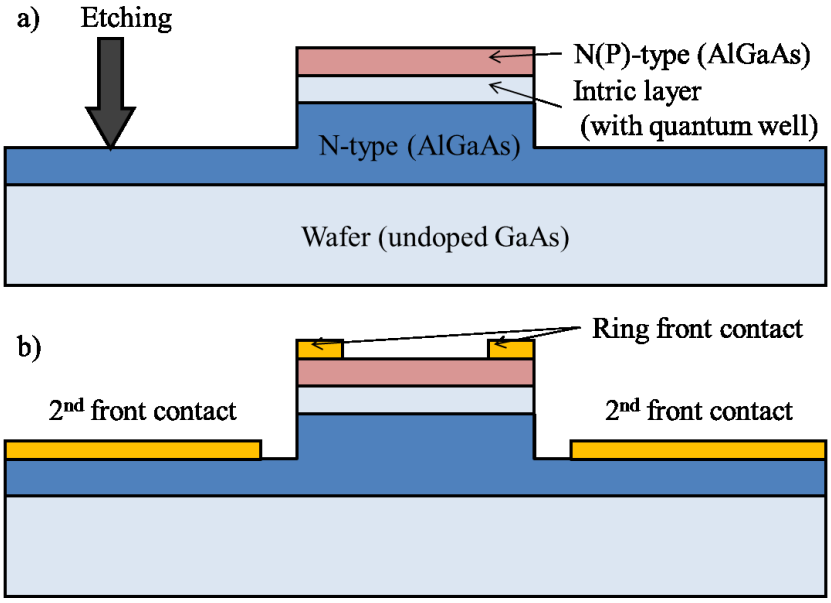

Figure 50: Processing of the samples

4.3 Rate Model for Sequential Absorption

In order to predict the sequential absorption of photons via the intermediate band which arises from confined states in the quantum well, a model combining the transition characteristics of the interband and inter-subband transitions is required.

4.3.1 Einstein Coefficients

Radiative transition of carriers between two discrete states occurs by emission or absorption of a photon with energy $E_\gamma = E_f - E_i$, whereE_f is the energy of the final state and E_i is the energy of the initial state. There are three types of radiative transitions: spontaneous emission, absorption and stimulated emission.

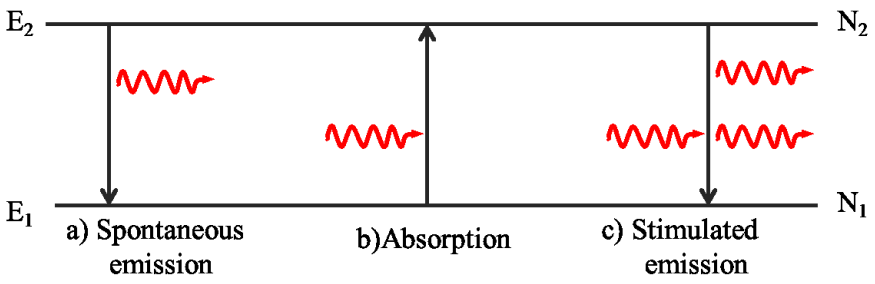

Figure 51: Spontaneous emission, absorption and stimulated emission transitions between two levels at energy E_1 and E_2 with population N_1 and N_2 through emission and absorption of photons

Spontaneous emission is a radiative process by which an electron in an upper state drops to a lower level through the emission of a photon, as shown in Figure 51a). The rate of spontaneous emission is described by the Einstein A coefficient for the transition A_{21}, which gives the probability of the electron in the upper level 2 dropping down to the lower level 1 by emitting a photon per unit time. The rate of change of the population of upper state N_2 is:

$$\frac{dN_2}{dt} = -A_{21}N_2 \tag{3.14}$$

and therefore by solving the equation the time dependent population of the excited state N_2 is given by an exponential decay:

$$N_2(t) = N_2(0)e^{-A_{21}t} = N_2(0)e^{-t/\tau} \tag{3.15}$$

where the radiative lifetime of the excited state $\tau = \frac{1}{A_{21}}$ is a time constant due to spontaneous emission and ranges from nanoseconds to several milliseconds depending on the type of process.

Conversely, absorption is a process which promotes an electron from the lower level to the upper state through the absorption of a photon, as per Figure 51b). This process only occurs when there is a photon present in the system and therefore depends on the spectral energy density $u(E_\gamma)$ of incoming radiation with photon energy E_γ. The transition probability is characterised by the Einstein B coefficient B_{12}, and the rate of absorption transition per unit time is given by:

$$\frac{dN_1}{dt} = -B_{12}N_1u(E_\gamma) \tag{3.16}$$

where the number of electrons in lower states 1 N_1.

Finally, we have stimulated emission, in which the incoming photon field stimulates downward transition through the emission of an additional photon, as per Figure 51a). The rate of this process is governed by the second Einstein B coefficient B_{21} and is given by:

$$\frac{dN_2}{dt} = -B_{21}N_2u(E_\gamma) \tag{3.17}$$

The three Einstein coefficients are not independent parameters and they all depend on each other. When the system is at thermal equilibrium with the environment, the steady state condition leads to the rate of upward transitions due to absorption balancing the rate of downward transition due to spontaneous and stimulated emissions.

$$B_{12}N_1u(E_\gamma) = A_{21}N_2 + B_{21}N_2u(E_\gamma) \tag{3.18}$$

Boltzmann's law determines the ratio of the population of upper and lower levels, which are in thermal equilibrium at temperature T:

$$\frac{N_2}{N_1} = \frac{g_2}{g_1}e^{-E_\gamma/kT} \tag{3.19}$$

and the black-body radiation equation of temperature T is given by the Planck formula:

$$u(E_\gamma) = \frac{{E_\gamma}^3}{\hbar^3\pi^2c^3}e^{E_\gamma/kT} \tag{3.20}$$

Therefore the relationship between the Einstein coefficients is given by:

$$g_1B_{12} = g_2B_{21} \tag{3.21}$$

$$A_{21} = \frac{{E_\gamma}^3}{\hbar^3\pi^2c^3}B_{21} \tag{3.22}$$

This shows that in the case of $g_1 = g_2$, the probabilities of absorption and stimulated emission are the same and once the radiative lifetime of transitions is known, the A_{21} coefficient can be determined, thus allowing for the calculation of $B_{12} = B_{21}$.

4.3.2 Radiative Transition Rate

The radiative transition rates between electronic states can be calculated by quantum mechanics based on time-dependent perturbation theory of light-matter interaction. Fermi's golden rule states that the transition rate between an initial state i and final state f is:

$$W_{i\to f}(E_\gamma) = \frac{2\pi}{\hbar}\left|\boldsymbol{M}_{if}\right|^2\delta(E_f - E_i - E_\gamma) \tag{3.23}$$

where the matrix element given by;

$$\boldsymbol{M}_{if} = \langle \psi_i | H' | \psi_f \rangle = \int \psi_f{}^*(\boldsymbol{r}) H'(\boldsymbol{r}) \psi_i(\boldsymbol{r})\, d^3\boldsymbol{r} \tag{3.24}$$

where $\boldsymbol{r}$ is the position vector of the electron, describes the effect of the external perturbation H' caused by the light wave on the electrons. $\psi_i(\boldsymbol{r})$ and $\psi_f(\boldsymbol{r})$ are the wavefunctions of the initial and final electronic states, i and f, respectively.

In the classical theory of radiative emission and absorption, the atoms are treated as oscillating electric dipoles. Absorption occurs when electromagnetic waves at the natural resonance frequency force oscillations that transfer energy from the light to the atoms. Emission also occurs at the natural frequency of the oscillator. The electric dipole interaction is the dominant factor in radiative transitions by several order of magnitude compared to the other dipoles, such as the magnetic dipole. The first order perturbation to the atom H' is caused by the integration between the electric field amplitude $\boldsymbol{\varepsilon}_\gamma$ of the light and the electric dipole $\boldsymbol{p}_e = -e\boldsymbol{r}$ of the atom.

$$H'(\boldsymbol{r}) = -\boldsymbol{p}_e(\boldsymbol{r}) \cdot \boldsymbol{\varepsilon}_\gamma(\boldsymbol{r}) \tag{3.25}$$

Then the matrix element can be written as:

$$\boldsymbol{M}_{if} = -\boldsymbol{\mu}_{if} \cdot \boldsymbol{\varepsilon}_\gamma \tag{3.26}$$

where the dipole moment of the transition is:

$$-\boldsymbol{\mu}_{if} = -e\big(\langle \psi_i | \boldsymbol{r} | \psi_f \rangle\big) \tag{3.27}$$

which determines the transition rate for the electric-dipole process.

In quantum wells, one-dimensional confinement in the z-direction leads to an electron state described by a wavefunction which takes the form of a product of the Bloch function of the band $u_i(\boldsymbol{r})$ and the slowly varying envelope function $\nu_{i,n_i}(\boldsymbol{r})$. The fast evolving periodic Bloch function is the same within the band and differs for states in different bands, i.e. conduction and valence bands. The slowly varying envelope function consists of a free wave in the xy-plane $e^{i\boldsymbol{k}_{xy,i}\cdot\boldsymbol{r}_{xy}}$ and the bound envelope function $\varphi_{i,n}(z)$ in the z-direction and is unique for each subband, $\nu_{i,n_i}(\boldsymbol{r}) = \frac{1}{\sqrt{A}}\varphi_{i,n_i}(z)e^{i\boldsymbol{k}_{xy,i}\cdot\boldsymbol{r}_{xy}}$

$$\psi_i(\boldsymbol{r}) = \frac{1}{\sqrt{A}} u_i(\boldsymbol{r})\varphi_{i,n_i}(z)e^{i\boldsymbol{k}_{xy,i}\cdot\boldsymbol{r}_{xy}} \tag{3.28}$$

where $n_i$is the subband index of the confined state. Therefore the matrix element can be separated into 2 parts which describes different types of optical transitions;

$$\boldsymbol{M}_{if} = \boldsymbol{\varepsilon}_{\gamma}(\boldsymbol{r}) \cdot \langle u_i | \boldsymbol{p}_e(\boldsymbol{r}) | u_f \rangle \left\langle \nu_{n_i} \middle| \nu_{n_f} \right\rangle + \boldsymbol{\varepsilon}_{\gamma}(\boldsymbol{r}) \cdot \langle u_i | u_f \rangle \left\langle \nu_{n_i} \middle| \boldsymbol{p}_e(\boldsymbol{r}) \middle| \nu_{n_f} \right\rangle \quad (3.29)$$

The first term is relevant only for interband transitions and the second term describes transitions between subbands in the same band.

Based on equation (4.21), the transition rate between two states can be calculated. When considering the total transition rate, all of the states which fulfil the required conditions for the transition to occur must be taken into account. The total upwards transition rate per unit area is calculated by summing over all the states while considering the occupation probability of both initial lower states 1 and final upper states 2:

$$R_{1\to2}(E_\gamma) = \sum_1 \sum_2 \frac{2\pi}{\hbar} |\boldsymbol{M}_{12}|^2 \delta(E_2 - E_1 - E_\gamma) f_1(E_1)(1 - f_2(E_2)) \quad (3.30)$$

where the occupation probability is given by the Fermi-Dirac distribution:

$$f_1(E_1) = \frac{1}{1 + e^{(E_1 - E_{F1})/kT}} \quad (3.31)$$

where E_F is the Fermi energy and T is the temperature of the system. Similarly, the downward transition rate per unit area is given by:

$$R_{2\to1}(E_\gamma) = \sum_1 \sum_2 \frac{2\pi}{\hbar} |\boldsymbol{M}_{21}|^2 \delta(E_1 - E_2 - E_\gamma) f_2(E_2)(1 - f_1(E_1)) \quad (3.32)$$

With $|\boldsymbol{M}_{12}| = |\boldsymbol{M}_{21}|$, the net upward transition rate per unit area in between the confined states 1 and 2 in the quantum well is given by $R_{1\to2} - R_{2\to1}$:

$$R_{12}(E_\gamma) = \sum_1 \sum_2 \frac{2\pi}{\hbar} |\boldsymbol{M}_{12}|^2 \delta(E_2 - E_1 - E_\gamma)(f_1(E_1) - f_2(E_2)) \quad (3.33)$$

It is important to note that a direct purely optical transition requires conservation of electro momentum as mentioned in chapter 1: $\boldsymbol{k}_2 = \boldsymbol{k}_1$. This means that the initial and final state must have the same k value as well as satisfying the conservation of energy forced by the delta-function and the transition is represented by vertical arrows in the electron E-k diagrams.

4.3.3 Interband Transition Model

The interband transition rate is governed by the matrix element;

$$\boldsymbol{M}_{if} = \boldsymbol{\varepsilon}_{\gamma}(\boldsymbol{r}) \cdot \langle u_i | \boldsymbol{p}_e(\boldsymbol{r}) | u_f \rangle \left\langle \nu_{n_i} \middle| \nu_{n_f} \right\rangle \tag{3.34}$$

The periodic function u_i and u_f is unique for the semiconductor material of the quantum well and therefore it is independent of the confinement. Therefore the dipole matrix element $\boldsymbol{P}_{if} = \langle u_i | \boldsymbol{p}_e(\boldsymbol{r}) | u_f \rangle$ is a constant for interband transition and it is given by $\frac{2|\boldsymbol{P}_{if}|^2}{m} \approx 20eV$ for most group-IV, III-V and II-VI semiconductors. The envelope function is given by $\nu_{i,n_i}(r) = \frac{1}{\sqrt{A}} \varphi_{i,n_i}(z) e^{ik_{xy,i} \cdot r_{xy}}$ where $\varphi_{i,n_i}(z)$ is the wavefunction confined by the quantum well potential and is determined by solving Schrödinger's equation (4.6).

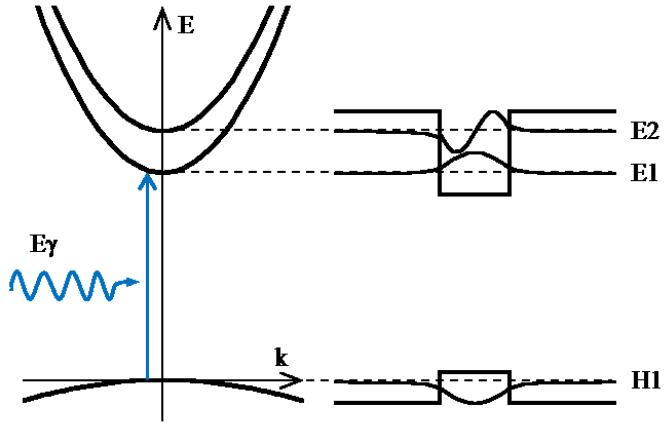

Figure 52: Schematic diagram of E-k dispersion relationship of quantum well and showing optical interband transition at Eγ between H1 and E1, which arise from 1 dimensional confinement.

By substituting equation (4.33) into equation (4.31) and summing over all the available states, the total strength of the transition can be calculated. In a quantum well system, there are many electron states distributed in both real space and energy space and we must consider all of these. As mentioned in section 1.6, in E-k space the electron states are distributed with a parabolic function which is a good approximation for both the conduction and valence band near the bend-edge.

$$E = E_n + \frac{\hbar^2 |\boldsymbol{k}_{xy}|^2}{2m^*} \tag{3.35}$$

The distribution is determined by the fitted parameter called effective mass m^* which differs for electrons m_e^* and holes m_{hh}^*. This distribution leads to a well defined density of states of a quantum well system, which defines the number of electron states per energy per unit area per quantum well layer as given by:

$$\rho^{2D}(E) = \frac{1}{2\pi} \frac{2m^*}{\hbar^2} \tag{3.36}$$

In order for the optical transition to occur, both energy and momentum needs to be conserved.

The E-k dispersion relationship of the electronic states for both E1 and H1 are given by;

$$E_{E1}(k) = E1 + \frac{\hbar^2 k^2}{2m_e^*} \tag{3.37}$$

$$E_{H1}(k) = H1 - \frac{\hbar^2 k^2}{2m_{hh}^*} \tag{3.38}$$

Conservation of energy means that the photon energy must equal to the energy difference between the initial and final electron states:

$$E_\gamma = E_{E1} - E_{H1} = E1 - H1 + \frac{\hbar^2 k^2}{2m_e^*} + \frac{\hbar^2 k^2}{2m_{hh}^*} \tag{3.39}$$

By defining the reduced electron-home mass μ:

$$\frac{1}{\mu} = \frac{1}{m_e^*} + \frac{1}{m_{hh}^*} \tag{3.40}$$

the relationship simplifies to:

$$E_\gamma = E1 - H1 + \frac{\hbar^2 k^2}{2\mu} \tag{3.41}$$

Then, the joint density of electron-hole states for any given photon energy can be determined:

$$\rho^{2D}(E_\gamma) = \begin{cases} 0, & E_\gamma < E1 - H1 \\ \frac{1}{2\pi}\frac{2\mu}{\hbar^2}, & E_\gamma \geq E1 - H1 \end{cases} \tag{3.42}$$

Therefore, the net absorption transition rate can be calculated by the integral of the function over energy:

$$R_{abs} = \int_{E_\gamma} \frac{2\pi}{\hbar} |\boldsymbol{M}_{12}|^2 \rho^{2D}(E_\gamma)\big(f_1(E_{H1}) - f_2(E_{E1})\big) dE_\gamma \tag{3.43}$$

This also depends on the intensity of the radiation I_γ which is related to the field strength of the electric field by:

$$I_\gamma = \frac{cn\epsilon_0}{2} |\boldsymbol{\varepsilon}_\gamma|^2 \tag{3.44}$$

where c is the speed of light, n is the refractive index and ϵ_0 is the vacuum permittivity. Therefore, for a known optical intensity, the absorption rate per unit area is given by:

$$R_{abs} = I_\gamma \int_{E_\gamma} \frac{2\pi}{\hbar}\frac{2}{cn\epsilon_0}\frac{1}{3}\left|\boldsymbol{P}_{if}\right|^2 \left|\left\langle \nu_{n_i}\middle|\nu_{n_f}\right\rangle\right|^2 \rho^{2D}(E_\gamma)\big(f(E_{H1}) - f(E_{E1})\big)dE_\gamma \tag{3.45}$$

The spontaneous emission rate relates to the absorption as per equation (4.20) through Einstein coefficients. Therefore, the emission rate can be determined by:

$$R_{emit} = \int_{E_\gamma} \frac{{E_\gamma}^3 n}{3\pi\epsilon_0\hbar^5 c}\left|\boldsymbol{P}_{if}\right|^2 \left|\left\langle \nu_{n_i}\middle|\nu_{n_f}\right\rangle\right|^2 \rho^{2D}(E_\gamma) f(E_{E1})\big(1 - f(E_{H1})\big)dE_\gamma \tag{3.46}$$

In both absorption and emission transitions, the overlap of the envelope function $\langle \nu_{n_i}|\nu_{n_i}\rangle$ determines the strength of the transition between confined energy levels and it is strongest when quantum numbers of the confined states in the valence and conduction bands are the same, i.e. $n_i = n_f$.

For known incoming radiation intensity $I_\gamma(E_\gamma,\, t_1)$ at given time t_1 and initial occupation of relevant states E_{H1} and E_{E1} through the Fermi-Dirac distribution (4.29), characterised by Fermi-level $E_{F,H1}(\,t_1)$ and $E_{F,E1}(\,t_1)$, the total generation rate $R_{abs,total}(t_1) = \int R_{abs}(E_\gamma, t_1)\, dE_\gamma$ and total recombination rate $R_{emit,total}(t_1) = \int R_{emit}(E_\gamma,\, t_1)\, dE_\gamma$ can be calculated from the above equations. The net charge carrier exchanged between the states in time interval dt is given by $\left(R_{abs,total}(t_1) - R_{emit,total}(t_1)\right)\Delta t$. The total number of carriers in the upper state at time $t_2 = t_1 + \Delta t$ is:

$$n_{E1}(t_2) = \int_{E_\gamma} \left[\rho^{2D}(E_\gamma) f\left(E_{E1}, E_{F,E1}(\,t_1)\right), + \left(R_{abs,total}(t_1) - R_{emit,total}(t_1)\right)\Delta t\right] dE_\gamma \tag{3.47}$$

Since the time mesh size is set to be longer than the thermalisation lifetime of the excited carriers, the carrier distribution is represented by the Fermi-Dirac distribution. Because of the constant density of states in quantum well confined energy bands, the new Fermi-level for a known number of carriers can be numerically determined:

$$E_{F,E1}(n_{E1}) = kT\log\left(\frac{h^2 n_{E1}}{4\pi m_e^* kT} - 1\right) \tag{3.48}$$

Similarly the Fermi-level for holes in the valence band can be determined and the same process is repeated for the time domain t_2, t_3… etc. For CW excitation, the system eventually reaches equilibrium.

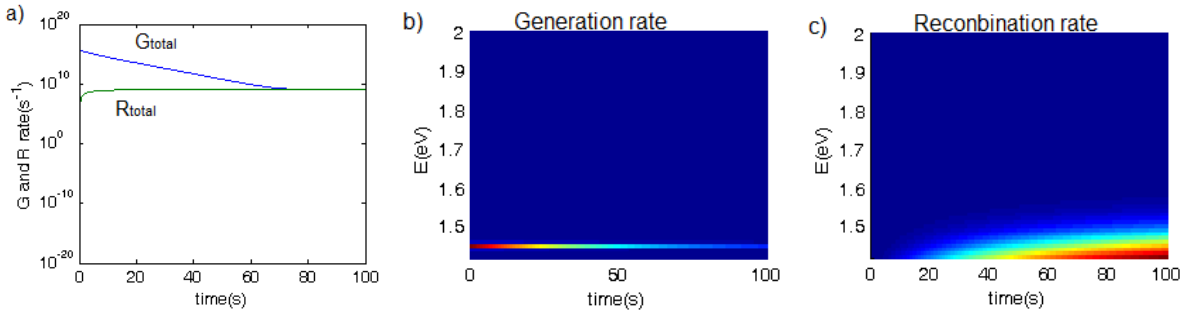

Figure 53: Simulation of interband transition in quantum well; a) showing total generation rate (G_{total}) and recombination rate (R_{total}) which convers as the system approaches steady state, b) showing generation rate and c) showing recombination rate at different photon energies E.

Figure 53 shows the simulation results of a quantum well with $E1 = 1.4eV$with CW optical excitation with monochromatic light source at 1.45eV with bandwidth of 0.01eV. As the excitation is above the bandgap between H1 and E1, the excited carriers quickly relax down to the bend-edge where they recombine. As the states fill up, the generation rate declines and reaches equilibrium where the generation rate and recombination rate balances.

4.3.4 Inter-subband Transition Model

In the case of the inter-subband transition between E1 and E2 states, the two states share the same periodic function of the conduction band, i.e. $u_i = u_f$. Therefore, the relevant matrix element to be considered is:

$$\boldsymbol{M} = \langle u_i | u_f \rangle \left\langle \nu_{n_i} \middle| \boldsymbol{\varepsilon}_\gamma(\boldsymbol{r}) \cdot \boldsymbol{p}_e(\boldsymbol{r}) \middle| \nu_{n_f} \right\rangle \tag{3.49}$$

where $\langle u_i | u_f \rangle = 1$.

The dipole matrix element of the envelope function $\left\langle \nu_{n_i} \middle| \boldsymbol{\varepsilon}_\gamma(\boldsymbol{r}) \cdot \boldsymbol{p}_e(\boldsymbol{r}) \middle| \nu_{n_f} \right\rangle$ defines all of the properties of this transition including the polarisation selection rule mentioned in section 1.7.2.

$$\left\langle \nu_{n_i} \middle| \boldsymbol{\varepsilon}_\gamma(\boldsymbol{r}) \cdot \boldsymbol{p}_e(\boldsymbol{r}) \middle| \nu_{n_f} \right\rangle = \frac{1}{A} \int \mathrm{d}^3\mathbf{r} e^{-i\boldsymbol{k}_{xy,i}\cdot\boldsymbol{r}_{xy}} \varphi^*_{i,n_i}(z) \left[\varepsilon_{\gamma,x} p_{e,x} + \varepsilon_{\gamma,y} p_{e,y} + \varepsilon_{\gamma,z} p_{e,z} \right] \varphi_{f,n_f}(z) e^{i\boldsymbol{k}_{xy,f}\cdot\boldsymbol{r}_{xy}} \tag{3.50}$$

Only the term proportional to $\varepsilon_{\gamma,z}$ yields a contribution as the other terms vanish except for when the initial and final states are identical, i.e. $n_i = n_f$ and $\boldsymbol{k}_{xy,i} = \boldsymbol{k}_{xy,f}$, which leads to the free-carrier absorption in the two-dimensional electron gas. Therefore, the matrix element of a confined envelope function $\left\langle \varphi_{i,n_i}(z) \middle| p_{e,z} \middle| \varphi_{f,n_f}(z) \right\rangle$, determines the inter-subband transition and only radiation with electric field component in the z-direction can be absorbed. This can be calculated numerically for known confined envelope functions.

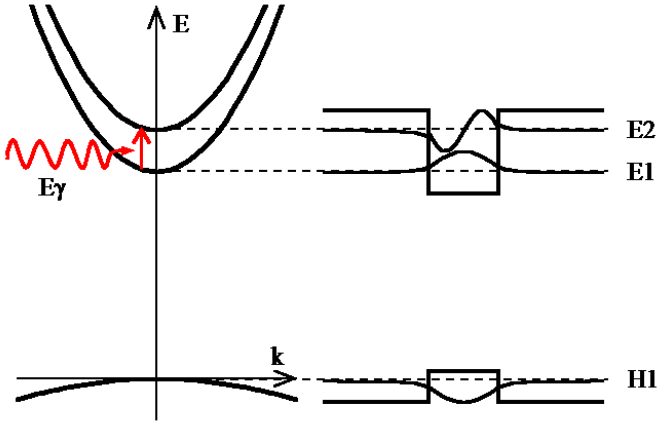

Figure 54: Schematic diagram of E-k dispersion relationship of quantum well and showing optical inter-subband transition at Eγ between E1 and E2, which arise from 1 dimensional confinement.

As mentioned in previous sections, there are many electron states distributed both in real space and energy space and we must consider all of these in order to calculated the total transition rate. The total absorption rate can be calculated by integrating equation (4.31) in two-dimensional k space $\boldsymbol{k}_{xy}$;

$$R_{abs} = I_\gamma \frac{2\pi}{\hbar} \frac{2}{cn\epsilon_0} \sum_i \sum_f \frac{2}{(2\pi)^2} \int d^2\boldsymbol{k}_{xy} \left| \left\langle \varphi_{i,n_i}(z) \middle| p_{e,z} \middle| \varphi_{f,n_f}(z) \right\rangle \right|^2 \delta\left(E_{E2} - E_{E1} - E_\gamma\right)\left(f_1(E_{E1}) - f_2(E_{E2})\right) \tag{3.51}$$

In the case of transition between states which belong to the same band, the E-k dispersion relationship of the electronic states is defined by the same effective mass m_e^*. Therefore, the parabolic relationship for E1 and E2 are given by;

$$E_{E1}(k) = E1 + \frac{\hbar^2 k^2}{2m_e^*} \tag{3.52}$$

$$E_{H2}(k) = E2 + \frac{\hbar^2 k^2}{2m_e^*} \tag{3.53}$$

The conservation of energy must also apply in this case and it is enforced by replacing the delta-function by a normalised Lorentzian with half width at half maximum of Γ. The same curvature of the initial and final states E-k dispersion relationship leads to monochromatic transition energy, $E_\gamma = E2 - E1$ and delta-function-like density of states:

$$R_{abs} = I_\gamma \frac{2\pi}{\hbar} \frac{2}{cn\epsilon_0} kT \sum_i \sum_f \frac{2}{(2\pi)^2} \left| \left\langle \varphi_{i,n_i}(z) \middle| p_{e,z} \middle| \varphi_{f,n_f}(z) \right\rangle \right|^2 \frac{\Gamma/\pi}{\left(E2 - E1 - E_\gamma\right)^2 + \Gamma^2} \ln\left[\frac{1 + e^{(E_{F,E1} - E_{E1})/kT}}{1 + e^{(E_{F,E2} - E_{E2})/kT}}\right] \tag{3.54}$$

and for the emission rate:

$$R_{emit} = I_\gamma \frac{2\pi}{\hbar} \frac{2}{cn\epsilon_0} \sum_i \sum_f \frac{2}{(2\pi)^2} \left| \left\langle \varphi_{i,n_i}(z) \middle| p_{e,z} \middle| \varphi_{f,n_f}(z) \right\rangle \right|^2 \frac{\Gamma/\pi}{\left(E_{E2} - E_{E1} - E_\gamma\right)^2 + \Gamma^2} f(E_{E2})\left(1 - f(E_{E1})\right) \tag{3.55}$$

Except for the difference in the transition strength, the model follows the same process to predict the behaviour. The generation rate and recombination rate is calculated at t_1 for known incoming radiation for the inter-subband transition $I_\gamma(E_\gamma, t_1)$ and initial occupation of the states. The net charge carrier exchanged between the states in time interval dt is given by $\left(R_{abs,total}(t_1) - R_{emit,total}(t_1)\right)\Delta t$ and the total number of carriers in the upper state at time $t_2 = t_1 + \Delta t$ can be calculated. The new Fermi-level is calculated for both bands and the same process is repeated for each time step.

4.3.5 Sequential Photon Absorption via Intermediate Band

In order to complete the model, the above two models must be proved by experiment and combined to create a model which describes the sequential absorption of photons via the intermediate band arising from quantum well confined states.

The model follows exactly the same steps, except for that E1 is now the final state of the interband transition, as well as the initial state of the inter-subband transition. The new carrier number of the E1 state is, therefore, calculated by:

$$n_{E1}(t_2) = \int_{E_\gamma} \Big[\rho^{2D}(E_\gamma) f\left(E_{E1}, E_{F,E1}(t_1)\right), + \Big(R_{interband\ abs,total}(t_1) - R_{interband\ emit,total}(t_1) - R_{intersubband\ abs,total}(t_1) + R_{interband\ emit,total}(t_1)\Big)\Delta t\Big] dE_\gamma \quad (3.56)$$

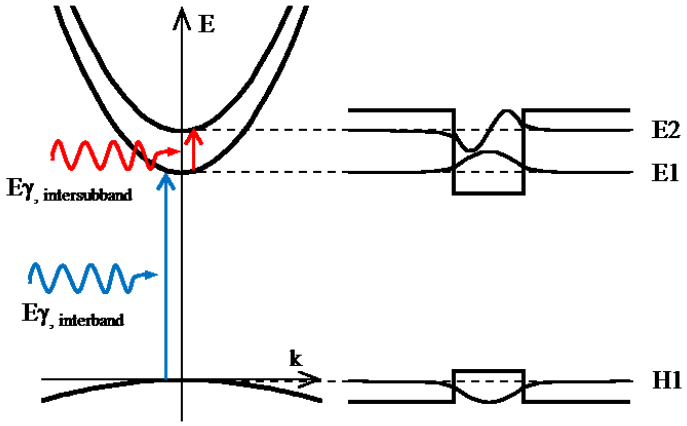

Figure 55: Schematic diagram of E-k dispersion relationship of quantum well and showing optical interband transition at $E\gamma_{,interband}$ between H1 and E1 followed by inter-subband transition at $E\gamma_{,inter\text{-}subband}$ between E1 and E2, which arise from 1 dimensional confinement.

4.4 Experimental Work

In order to build the complete model which predicts the optical carrier generations in a real quantum well system, the optical character of the single quantum well devices as designed earlier in the chapter is experimentally investigated. The details of samples VN2817-20 are described in Appendix A, 3-6.

4.4.1. Sample 1: n-i-n with n-doped Quantum Well Sample

The n-i-n sample has an n-doped single quantum well in the i-region which already has carriers in the E1 band. By illuminating the sample from the wedge, the carriers can be excited into the E2 band where they can be drifted in the applied field and conduct current, despite the sample otherwise acting as a resistor.

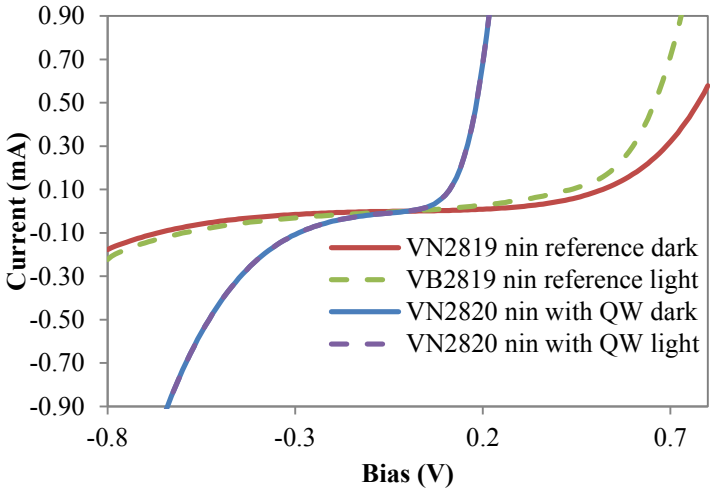

Figure 56: Current voltage relationship of n-i-n samples, VN2819 and VN2820 in dark and with light.

The reference n-i-n sample shows very low conductivity as shown in red in Figure 56 due to a highly resistive intrinsic region. The n-i-n sample with the quantum well has low conductivity at low applied bias but conductivity increases at high bias as carriers in the quantum well start to tunnel out of the well, carrying current. Even though the I-V curve is expected to be symmetric in these devices, both show higher conductivity at forward bias compared to reverse bias. This is because of the difference in the n-contacts which are made with one contact at the top of the mesa with Ti/Au and the other contact at the etched lower surface with Au/Ge/Ni/Au.

When the samples are illuminated with photons with energy above the bandgap of the devices, absorbed photons generate carriers in the i-region and conductivity increases, as can be seen in Figure 56. In actual fact, the photocurrent flows even at zero bias because of the asymmetry in the electric potential due to the difference in the contacts. The wavelength-dependent photocurrent has been measured and external quantum efficiency (EQE: the method and definition as described in section 3.1.3) calculated and plotted in Figure 57.

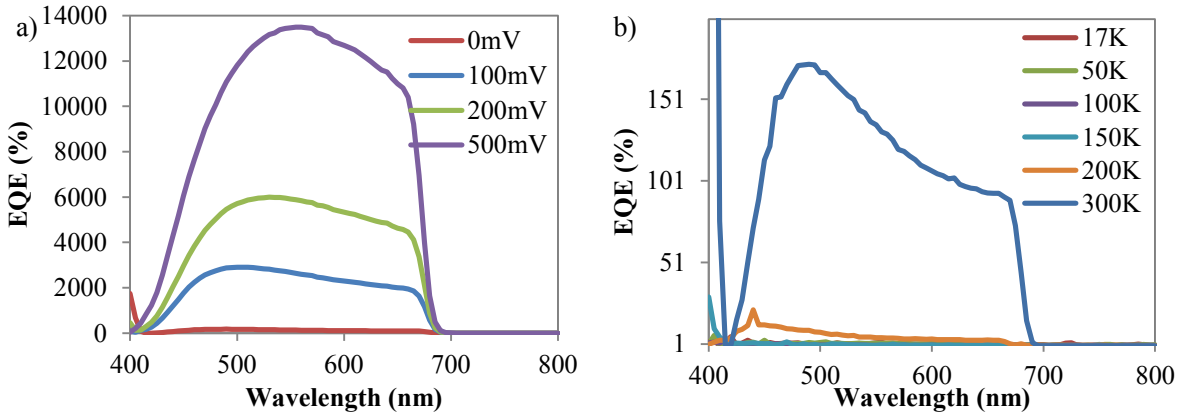

Figure 57: External quantum efficiency of VN 2819 a) with different applied bias at 300K and b) at different temperature and with zero bias.

The EQE of the device at different applied bias shows efficiency exceeding 100% which is unphysical as 1 photon cannot generate more than 1 charge carrier. However, the excited electrons can flow across the i-region many times until they recombine with holes leading to single electrons detected many times and thus higher photocurrent. In Figure 57b), the temperature-dependent EQE at zero bias shows that the n-i-n sample has much higher photocurrent at high temperatures due to lower conductivity in the n-region reducing the total conductivity of the device.

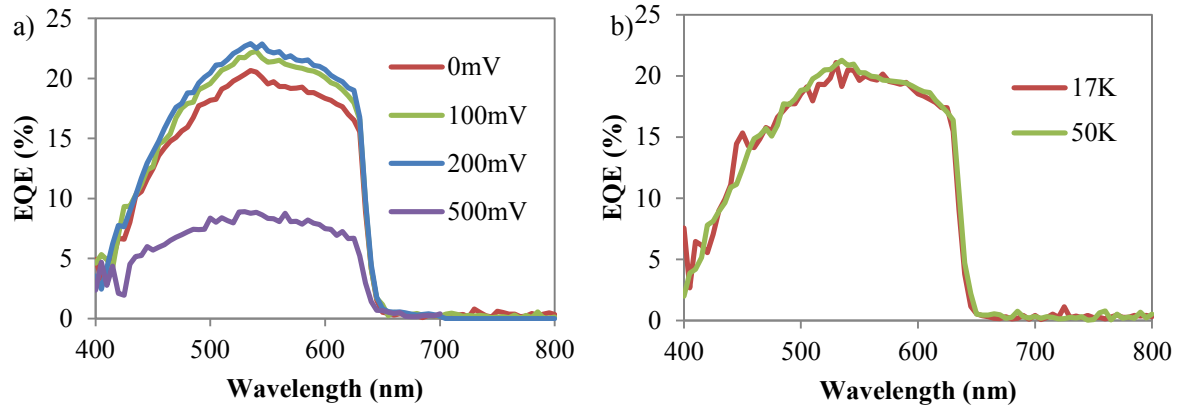

Figure 58: External quantum efficiency of VN 2820 a) with different applied bias at 300K and b) at different temperature and with zero bias.

In VN2820, as the dark current is much higher than the VN2819, the EQE measurement becomes much more difficult especially at higher temperature, as seen in Figure 58. The bias-dependent EQE shows that the increase in leakage current affects the measurement of photocurrent as the higher background noise reduces the sensitivity.

At the time of writing, only the basic characterisation of the sample has been achieved due to long delays in the sample fabrication process, which was caused by the service requirement of the MBE machine. In order to proceed to the next step, proper inter-subband characterisation of the sample is required which could not be completed within the timescales of the PhD project. The work will be continued in the future and the plan for this is outlined in chapter 5.

4.4.2. Sample 2: p-i-n Quantum Well Sample – Quantum Well Solar Cell

VN2817 is a p-i-n sample which has a single quantum well in the i-region without any doping and VN2818 is a reference sample with an identical structure except for the quantum well. As the sample does not have carriers in the E1 band of the quantum well, the E1states first need to be photofilled in order to observe the inter-subband transition. Therefore, by illuminating the sample from the wedge while continuously exciting the carriers from the H1 state to the E1 state through CW radiation at a wavelength to match the interband transition, the carriers can be excited into the E2 band from H1via

the E1 state and any extra photocurrent observed will be due to sequential absorption of the photons. The samples firstly facilitate the investigation of interband transitions to provide enough information for the model, before subsequently being used for the study of sequential absorption of photons via the intermediate band.

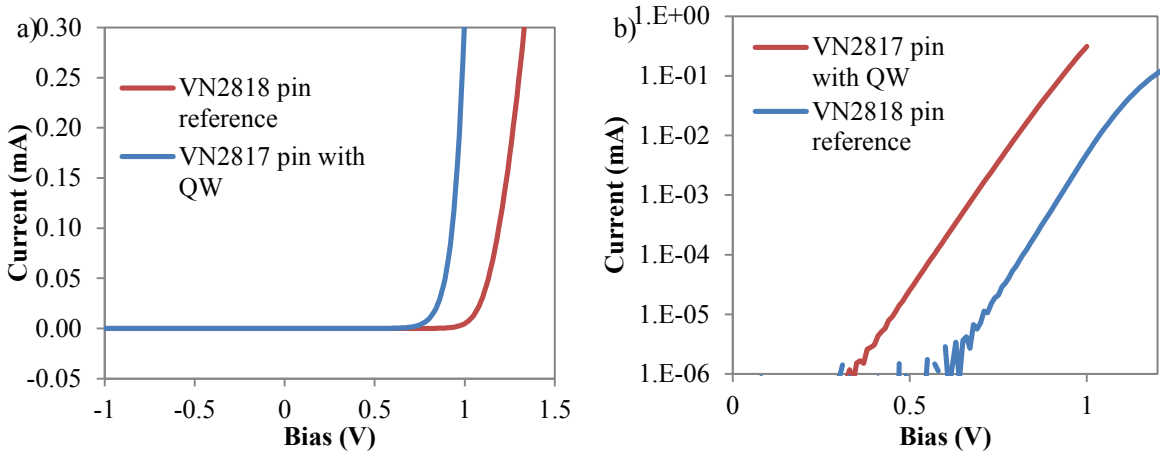

Figure 59: Current voltage relationship of p-i-n samples a) on normal scale and b) on log scale

The current voltage characterisation of the samples shows good p-i-n diode behaviour with low leakage current. The straight line, shown in log plot Figure 59b), means that they are both close to the ideal diode and both series and Shunt resistance is very low. With the quantum well in the i-region, VN2817 shows I-V characteristics which reflect the effectively lower bandgap device.

The EQE measurement of the devices shows a steady shift in the bandgap energy with temperature in Figure 60.

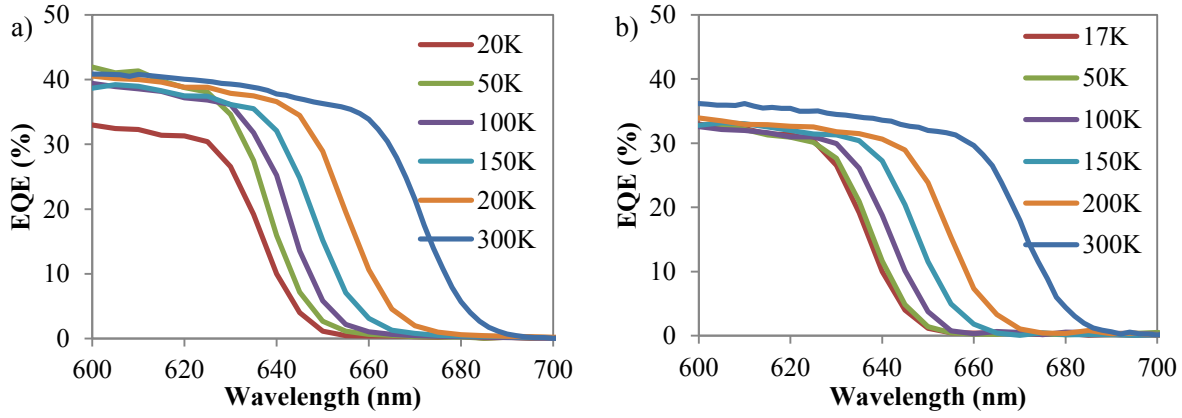

Figure 60: External quantum efficiency of a) VN2817 and b) VN2818 at different temperature

The main purpose of the EQE measurement was to determine the transition energy of the interband transition in the quantum well as well as the strength of the transition. However, due to an issue with

the noise levels caused by vibration in the cryogenic system, this proved to be difficult. Further work on this is planned and again, is outlined in the final chapter.

4.5 Summary

In this chapter, a new set of samples have been presented, which were designed in order to experimentally investigate the interband and inter-subband transitions individually. The rate model for simulating these transitions were programmed and the two models were combined to predict the strength of sequential absorption of the photons in the quantum well in order to simulate a quantum well IBSC. Some of the basic characteristics of the samples were also measured and analysed.

There is further experimental work planned for the future which will be carried out using the same samples and a description of this is outlined in the chapter 5.

Chapter 5

Conclusion and Further Work

Photovoltaic energy conversion could provide a renewable, low carbon energy source by utilising solar energy which is unlimited and powers the Earth's climate and ecosystem. However, the photovoltaic energy conversion efficiency of a single junction solar cell is limited to 31% at 1-sun. The IBSC is a concept which could potentially raise this efficiency limit and promises high power conversion efficiency in the future. Much study of IBSCs has been undertaken using quantum dots and highly-mismatched alloys but the power conversion efficiency gain has not been demonstrated due to the short lifetime of the intermediate and conduction electron states. The innovative concept of the Photon Ratchet IBSC (PR-IBSC) adds an extra energy band that extends the lifetime of carriers by suppressing direct recombination routes. The main aim of this project was to prove the benefit of the new concept and to design an IBSC which implements this innovative structure through experimental and theoretical work.

The first calculation of the theoretical power conversion efficiency limit under optimum conditions using the detailed balance model is presented. Even though the addition of the ratchet band introduces extra energy loss due to thermalisation of carriers from the IB to the RB, there is a theoretical efficiency gain overall and the limiting efficiency is increased from 46.8% to 48.5% at 1-sun. In order to understand where the power gain has come from, the loss mechanisms in solar cells were investigated and their contributions determined. By comparing the composition of the losses in IBSCs and PR-IBSCs, it was found that, although the ratchet inevitably increases the below-bandgap and thermalisation losses, the associated efficiency gain through reduction in recombination is even larger leading to a net efficiency increase. However, at full concentration, the ratchet level reduces the efficiency of an IBSC. The fundamental difference between a solar cell operating at full concentration and one at 1-sun, is the presence of the Boltzmann loss, which is caused by significant entropy generation due to the mismatch between the étendues of the restricted incident solar photons and isotropic emitted light. Hence, at 1-sun, the introduction of the ratchet band reduces recombination rates which, in the presence of a significant Boltzmann loss, leads to higher net efficiency. At full concentration, the Boltzmann loss is absent, so while the introduction of the ratchet band enables the recombination rates to be adjusted, the loss introduced by the ratchet band cannot offset any other losses in the cell. This work has been published in *Applied Physics Letters* in 2012 to propose the PR-IBSC for the first time, along with the results of theoretical calculations.

In order to accomplish a working IBSC, we have chosen a quantum well, in which the IB and the RB arises from quantum confinement of electron states in the conduction band, as a possible candidate.

This was due to quantum wells having a larger optical absorption cross-section, as well as less constraint in choosing the position of the energy levels by changing material compositions and thickness of the layers, when compared to other potential materials. Through experimental characterisation of GaAs p-i-n diode with a single 7nm InGaAs well in the i-region, we have experimentally observed a clear increase in photocurrent due to sequential absorption of sub-bandgap photons. Multiple photon absorption is one of the essential conditions needing to be satisfied for IBSCs and the result indicates that the quantum well could be a suitable candidate for IBSCs. This experimental result has been published in the *Journal of Photovoltaics* in 2014 to mark the first observation of photocurrent generated by sequential absorption of photons in a quantum well IBSC. Along with the work on PR-IBSCs mentioned above, we have put in on-going experimental efforts to observe sequential absorption of visible photons in the shape of photocurrent in InGaAs double quantum wells with a GaAs barrier.

Finally, in order to fully understand the optical transitions characteristics of quantum wells, it is important to characterise the interband and inter-subband transitions individually. Building a model to describe the carrier density-dependent strength of both transitions, as well as the lifetime of excited carriers, has led us to better understand the sequential carrier generation process between confined energy levels in quantum wells. We have designed n-i-n and p-i-n devices with an identical single quantum well to experimentally study the transitions individually and have built a model to simulate the transitions, as well as carry out basic characterisation of the samples. This work is part of an ongoing project and ideas for further work include optical characterisation of the transitions, the details of which are described below.

Further Work

As mentioned above, there is further work to be done on the new set of samples which have been fabricated and have undergone some basic characterisation work, as mentioned in chapter 4.

The n-i-n quantum well sample VN2820 described in chapter 4 is designed to study inter-subband transition between confined states in the conduction band which arises from two-dimensional quantum confinement. Firstly, in order to determine the wavelength of the inter-subband transition, the IR EQE of the sample must be measured with the radiation coupled from the wedge and at some applied bias so that the photocurrent signal is amplified. If the signal appears to be weak, the same measurement may be performed using a quantum cascade laser as the excitation source, which has much higher optical power density compared to the monochromatic radiation from the lamp and which is linearly polarised, so that the photocurrent response will be larger. There is also an opportunity to undertake this measurement at the Diamond Light Source which has the facility for

multimode IR micro-spectroscopy – an advanced quantitative analytical technique which can provide tightly focused illumination of the sample, achieving high optical density, while measuring the frequency-dependent response of the sample through high sensitivity vibrational spectroscopy via FTIR up to the THz range. We expect the photocurrent response to be broadband as the transition broadening parameter Γ in (4.52) is large such that it removes all divergences, leading to two smooth transition peaks for bound-to-bound and bound-to-continuum, even possibly merged to form 1 peak. By fitting the results to the model described in chapter 4, the transition energy and the position of the subbands can be identified. It is important to note that this measurement should be performed at a multiple bias point as the position of the peaks shift when there is a large applied electric field across the quantum well due to shift in subband positions.

Photocurrent measurements described above are useful for identifying transition energy and relative transition strength. However, it is difficult to determine the absolute transition strength from the result because of the amplification of photocurrent signal, known as gain, in the n-i-n diode due to applied bias. The amplification factor depends on the applied bias and it is almost impossible to operate the experiment at a gain level which is exactly equal to one. In order to measure the exact transition strength of the inter-subband transition, we need to measure the absorption of the IR directly, using the experimental setup shown in Figure 61a). The optically chopped IR beam from the quantum cascade laser goes through the sample and transmitted light is detected and separated from the background signal by the use of a lock-in-amplifier. It must be noted that the sample needs to be processed into the geometry as described in chapter 1 (Figure 12), in order to couple the IR light into the inter-subband transition. Subtracting the signal of transmitted light through the sample from the signal without the sample in place will show the reduction in the IR transition due to the sample. However, this includes not only the absorption by the quantum well but also the interface reflections and free carrier absorption. In order to separate the quantum well absorption from other effects, the same measurement should be repeated on the reference sample VN2819 which has an identical structure to the VN2820 but without the quantum well. Therefore, a comparison of the transmission data of VN2820 with the VN2819 will reveal the strength of the inter-subband transition.

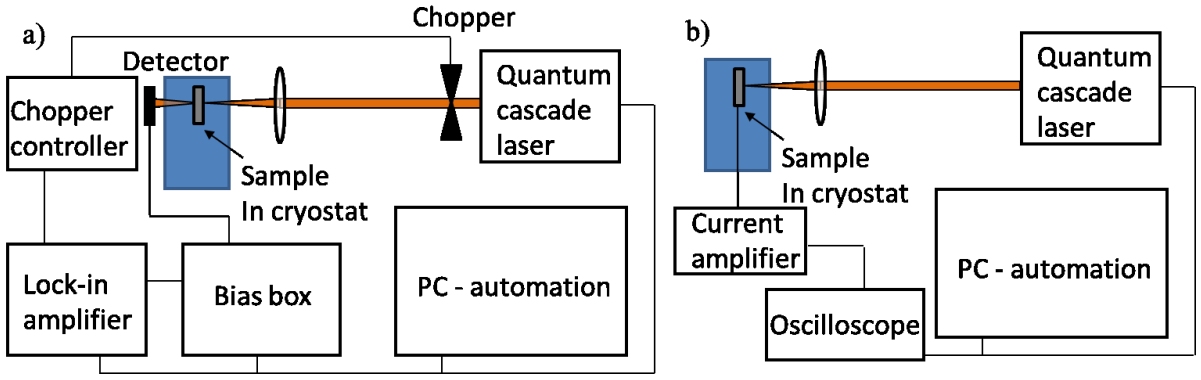

Figure 61: Experimental set for a) IR absorption measurement of sample. b) Transient photocurrent measurement.

The other property of the inter-subband transition that we would like to determine in order to complete the model is the lifetime of the excited carriers. This can be experimentally measured through transient photocurrent using the setup shown in Figure 61b). The photocurrent generated by the sample by an IR laser pulse is converted by the fast current amplifier and analysed using the oscilloscope. The photocurrent will only flow while the carriers are still in the excited states and by measuring the photocurrent decay over time, the lifetime of the excited carriers can be indirectly measured.

With the data collected by the above measurements, the inter-subband model described in chapter 4 will be complete.

The p-i-n quantum well device VN2817 is the sample which acts as a quantum well IBSC and is the perfect sample to study both interband and inter-subband transitions, together with its reference sample VN2818. In addition to what has been measured so far (details described in chapter 4), we plan to investigate inter-subband properties further using this sample. In order to identify the position of all relevant states, we plan to perform bias-dependent low-temperature EQE measurement focusing on the response in the region below the bandgap of the AlGaAs barrier. At short circuit and low applied bias conditions, the carriers generated via the transition between the confined energy states in the conduction band and the valence band, such as H1 to E1, tunnel through the barrier and contribute to photocurrent.[72] Therefore, by fitting the transition wavelength to the simulation of quantum wells described in chapter 4, the position of the confined states in the conduction band and the valence band can be determined. As the quantum well in n-i-n and p-i-n devices should be identical, the energy separation between the confined energy states in the conduction band determined from the samples should be the same. Unlike the n-i-n samples, since the two terminals are connected to different bands, a single photo-generated carrier can contribute to photocurrent once, so there is a one-to-one relationship between the absorbed photon and the photo-generated electron flow in p-i-n devices. From the bias-dependent EQE data alone, the transition rates between the confined states of the conduction and valence bands can be determined, while absorption measurement using a visible beam can also be performed on a double side polished wafer.

Again, we are also interested in the interband optical lifetime of photo-generated carriers and this can be determined directly by measuring the PL decay using the time-resolved PL setup shown in Figure 62. A pulsed laser generates carriers which quickly thermalise to the bend-edge and emit photons through optical recombination. Measuring the number of photons at peak wavelength at some time after the pulsed laser triggers, followed by collecting the data at different times to obtain the full picture of time-decaying PL, can allow us to determine the optical lifetime of the carriers in confined

states. The decay profile also includes the carrier thermalisation time, which should be much faster compared to the radiative lifetime of the carriers, but still is important enough to be considered.

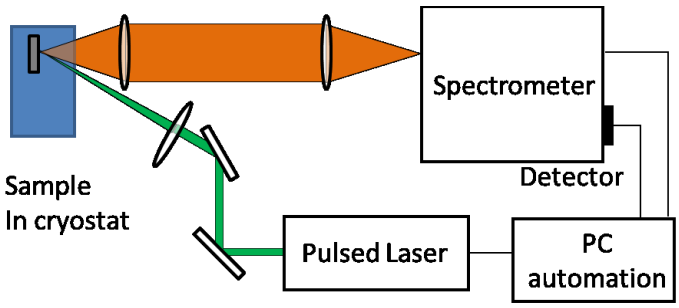

Figure 62: Experimental setup for time resolved PL

This should then complete the interband model described in chapter 4 and thus combining with the inter-subband model from before, this will finally allow us to predict the photocurrent generated by sequential absorption of photons which is a large milestone of this project.

Finally, VN2817 can be used to study the sequential absorption of subbandgap photons via interband and inter-subband transitions in quantum wells. Unlike VN2820, the E1 states need to be photofilled before the inter-subband takes place. Figure 63 shows the experimental setup where the sample is illuminated with the CW laser to continuously generate the carriers in the E1 states, which can then be excited to E2 states by the pulsed IR beam from the quantum cascade laser. The transient photocurrent is recorded by the oscilloscope and, although there will be background photocurrent signal due to the tunnelling of the carriers generated by the CW laser, the second inter-subband signal due to the absorption of the IR photons should appear as an increase in photocurrent. By using the tuneable laser for both transitions with different optical densities, the full wavelength dependent sequential absorption process can be observed.

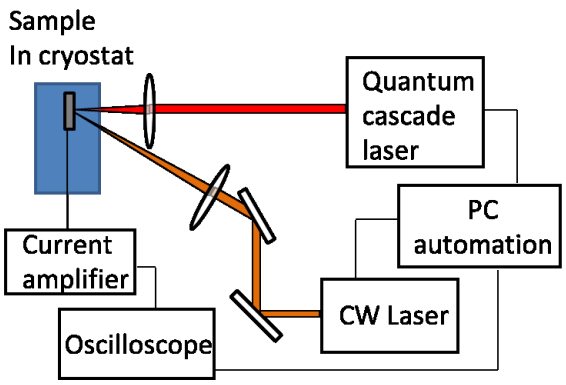

Figure 63: Experimental setup for sequential absorption measurement

At the Diamond Light Source mentioned previously in this chapter we can also measure the absorption of IR photons via FTIR through the use of IR radiation from a synchrotron, while optically generating the carriers in the E1 states of VN2817.

Conclusion

In this project, we have shown that the photon ratchet increases the limiting efficiency of an IBSC and hence provides fundamental benefits to photovoltaic energy conversion. Through detecting photocurrent due to the sequential absorption of photons, we have demonstrated that confined energy levels in quantum wells are suitable for creating intermediate states. By completing the additional experiments described above, we would be able to learn the rates of each transition under given conditions and use this information to model PR-IBSCs in which a quantum cascade structure takes the main role of thermal transport from the IB to the RB, and where the radiative lifetime of the carrier can be extended by the use of a type-II structure acting to spatially separate electrons from holes, example of which is shown in Figure 64.

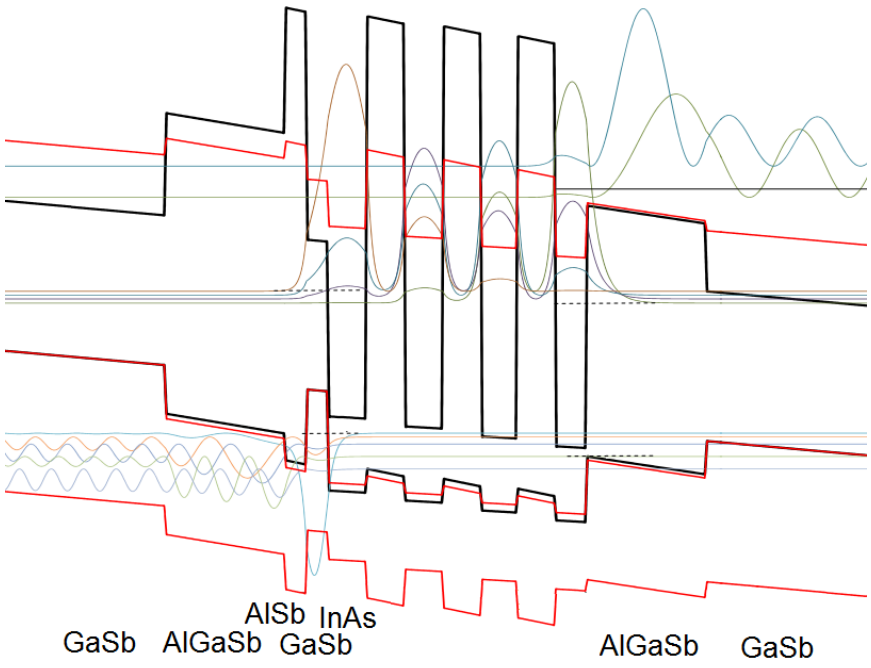

Figure 64: Possible quantum cascade PR-IBSC based on GaSb material designed by Oliver Curtin. The carrier generation via optical interband transition takes place in GaSb/InAs step well with AlSb barrier before holes tunnel out to the left and electrons cascade down to the InAs well on the right where it can undergo inter-subband transition.

By demonstrating a PR-IBSC, we intend to further increase the energy conversion efficiency of photovoltaic devices and thus contribute towards lowering their cost per unit energy - eventually to a level where they can directly compete with currently available sources of energy.

Appendix A: Details of samples

1. Sample Data - QT1168

Single quantum well p-i-n solar cells grown on a substrate on-axis GaAs (manufactured by Wafer Tech L) which was a 2 micron v-grooved Si doped buffer layer structured by Toshiba.

Thickness (Å)	Material	Dopant	Type	Concentration (cm^{-3})
2200	GaAs	C	p	2.3E+18
450	$Al_{0.8}Ga_{0.2}As$	C	p	2.0E+18
5000	GaAs	C	p	2.0E+18
1560	GaAs			
70	$In_{0.2}Ga_{0.8}As$			
1560	GaAs			
40000	GaAs	Si	n	1.0E+18
15000	$Al_{0.3}Ga_{0.7}As$	Si	n	1.0E+18
500	AlAs	Si	n	2.0E+18
1000	GaAs	Si	n	1.0E+18

Epitaxial growth details supplied by J.S. Roberts, University of Sheffield.

The following structured substrates were used, the buffer layer coated substrate patterned by Toshiba, a 2u grooved Si doped on axis half wafer located downstream, standard 3deg off process trial Si VFG half wafer in the UP position. Sample morphology for the 3deg off sample was free of texture while the two patterned wafers had the typical on-axis surface defects. This can be explained by growth infilling the etched features leaving a surface which behaves as an on-axis substrate. All assessment was made on the 3deg off UP wafer with a single Polaron trace providing the p and n-GaAs doping. No profile of the AlGaAs and AlAs was made.

Coated by 2um of Si:Al0.3 to form an anti reflection coating for 970nm.

2. Sample Data - N2139

Sample supplied by Sharp Laboratory of Europe Limited.

Nitride single quantum well p-i-n light emitting diode grown on Si doped GaN on sapphire substrate.

Thickness (Å)	Material	Dopant	Type	Concentration (cm^{-3})
2100	GaN	Mg	p	2.3E+18
50	$Al_{0.1}Ga_{0.9}N$			
24	$In_{0.2}Ga_{0.8}N$			
200	$Al_{0.1}Ga_{0.9}N$			
50	$Al_{0.1}Ga_{0.9}N$			
24	$In_{0.2}Ga_{0.8}N$			
200	$Al_{0.1}Ga_{0.9}N$			
1200	GaN	Si	n	1.0E+18

Top surface with contacts without mesa.

Electroluminescence of devices.

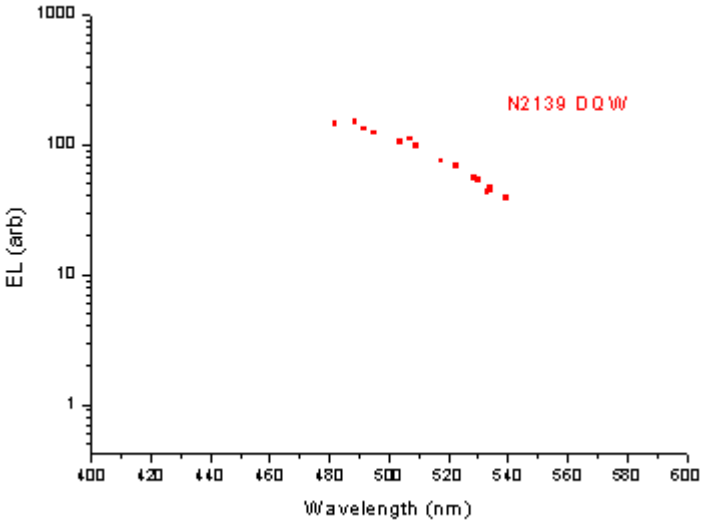

3. Sample Data - VN2817

Single quantum well p-i-n solar cell grown on undoped GaAs substrate.

Thickness (Å)	Material	Dopant	Type	Concentration (cm^{-3})
200	GaAs	Be	p	2.0E+18
1500	$Al_{0.3}Ga_{0.7}As$	Be	P	9.0E+17
1250	$Al_{0.3}Ga_{0.7}As$			
250	$Al_{0.3}Ga_{0.7}As$			
70	$In_{0.05}Ga_{0.95}As$			
1500	$Al_{0.3}Ga_{0.7}As$			
5000	$Al_{0.3}Ga_{0.7}As$	Si	n	2.0E+18
2000	GaAs			

Epitaxial growth details supplied by Edmund Clarke, University of Sheffield.

Room temperature PL.

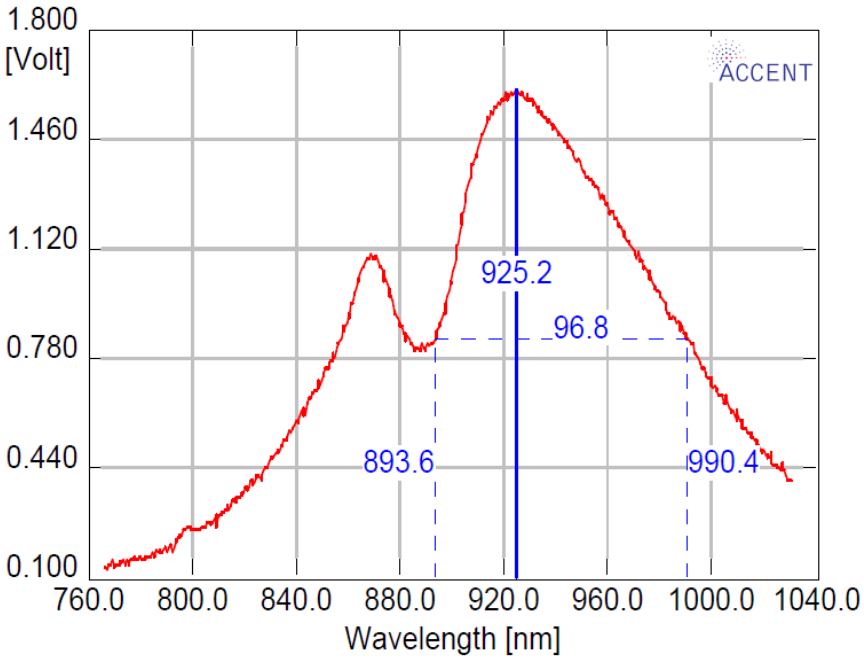

4. Sample Data - VN2818

Reference p-i-n solar cell for VN2817 grown on undoped GaAs substrate.

Thickness (Å)	Material	Dopant	Type	Concentration (cm^{-3})
200	GaAs	Be	p	2.0E+18
1500	$Al_{0.3}Ga_{0.7}As$	Be	P	9.0E+17
3070	$Al_{0.3}Ga_{0.7}As$			
5000	$Al_{0.3}Ga_{0.7}As$	Si	n	2.0E+18
2000	GaAs			

Epitaxial growth details supplied by Edmund Clarke, University of Sheffield.

Room temperature PL.

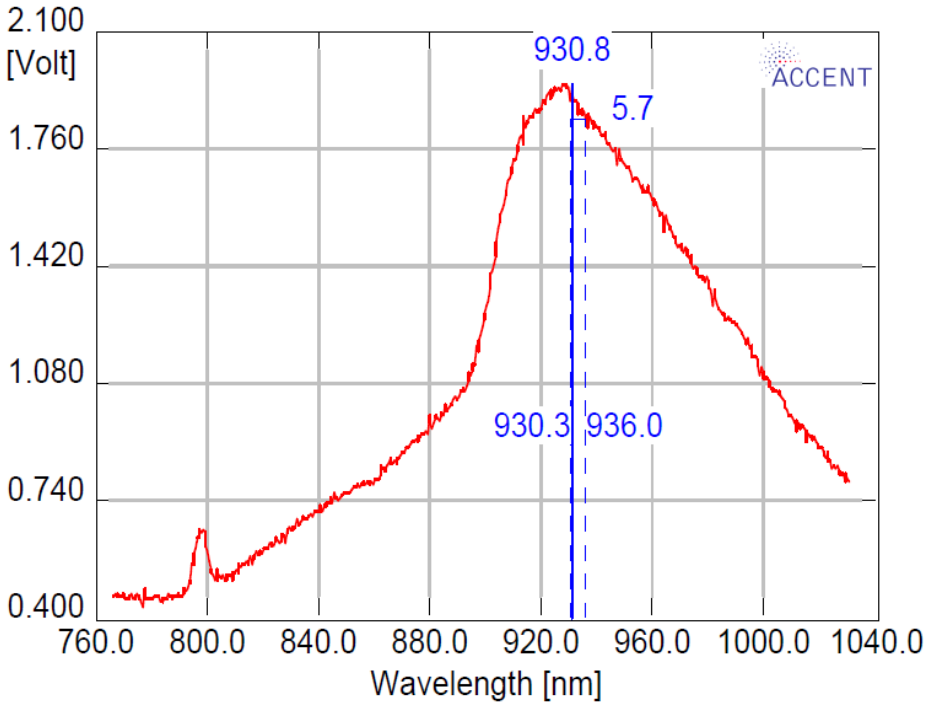

5. Sample Data - VN2819

Reference n-i-n device for VN2820 grown on undoped GaAs substrate.

Thickness (Å)	Material	Dopant	Type	Concentration (cm^{-3})
200	GaAs	Si	n	2.0E+18
1500	$Al_{0.3}Ga_{0.7}As$	Si	n	9.0E+17
3070	$Al_{0.3}Ga_{0.7}As$			
5000	$Al_{0.3}Ga_{0.7}As$	Si	n	2.0E+18
2000	GaAs			

Epitaxial growth details supplied by Edmund Clarke, University of Sheffield.

Room temperature PL.

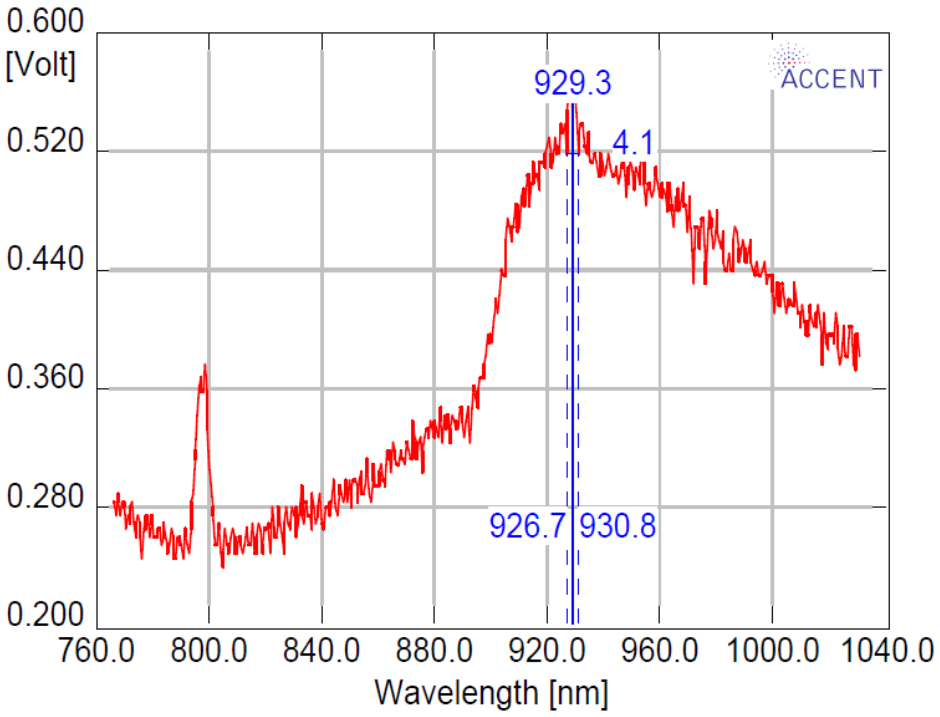

6. Sample Data - VN2820

Single n-doped quantum well in a n-i-n device grown on undoped GaAs substrate.

Thickness (Å)	Material	Dopant	Type	Concentration (cm^{-3})
200	GaAs	Si	n	2.0E+18
1500	$Al_{0.3}Ga_{0.7}As$	Si	n	1.0E+18
1250	$Al_{0.3}Ga_{0.7}As$			
250	$Al_{0.3}Ga_{0.7}As$			
70	$In_{0.05}Ga_{0.95}As$	Si	n	2.0E+18
1500	$Al_{0.3}Ga_{0.7}As$			
5000	$Al_{0.3}Ga_{0.7}As$	Si	n	1.0E+18
2000	GaAs			

Epitaxial growth details supplied by Edmund Clarke, University of Sheffield.

Room temperature PL.

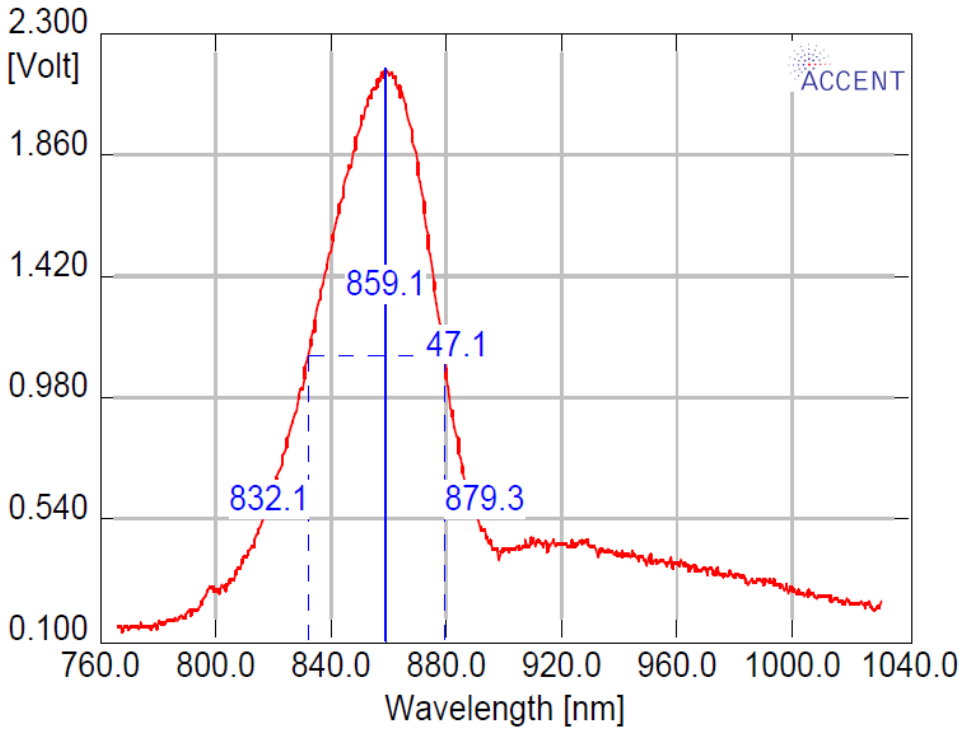

Appendix B: Simulation of Devices

1. k.p theory [73]

In typical bulk semiconductor crystals, the band structure is described by a parabolic E-k dispersion relationship using an effective mass approximation near the conduction band-edge. However, away from the conduction band-edge and in the valence band, especially in strained quantum wells, the band structure is more complicated and requires other approximation methods for calculating the band structure and optical properties of crystalline solids.

The conduction band states are mostly s-like in character, while the valence band states are mostly p-like at the level of the crystalline unit cell. There are three degenerate p-type atomic orbitals which take part in valence band state wave functions. Detailed calculations using the empirical pseudopotential method show that there are two valence bands degenerate at the centre of the Brillouin zone, namely heavy-hole and light-hole bands, and a third band close by, called the spin-orbit split-off band. The bands are energy eigenstates of the bulk material and described by single band states in bulk crystal. However, in quantum wells, the states are mixed and the wavefunctions have contributions from all the bulk bands. In such a situation, the states are described by Hamiltonian matrices or coupled Schrödinger equations which deliver the possible energies and wavefunctions expressed as a set of envelope functions representing the amplitude of the corresponding basis states of the bulk bands. This method is known as the multiband effective mass method or the k.p method because the interaction is described by the k.p perturbation.

According to quantum mechanics in the single-electron approximation, the electrons have wavefunction which can be described by the Schrödinger equation:

$$\mathcal{H}\Phi_n(\boldsymbol{r}) = \left[\frac{p^2}{2m} + \boldsymbol{V}(\boldsymbol{r})\right]\Phi_n(\boldsymbol{r}) = E_n\Phi_n(\boldsymbol{r}) \qquad (6.1)$$

where $\mathcal{H}$ is the Hamiltonian, p is the momentum operator, m is mass of an electron, $\boldsymbol{V}$ is the potential, $\Phi_n(\boldsymbol{r})$ and E_n are the wavefunction and energy of an electron in an eigenstate labelled by n. The solutions of the Schrödinger equation, using the Bloch function theorem in the reduced zone scheme, are expressed as:

$$-\Phi_{n\boldsymbol{k}}(\boldsymbol{r}) = exp(i\boldsymbol{k}.\boldsymbol{r})u_{n\boldsymbol{k}}(\boldsymbol{r}) \qquad (6.2)$$

where n is the band index, $\boldsymbol{k}$ is the wavevector in the first Brillouin zone and $u_{n\boldsymbol{k}}$ has the periodicity of the lattice. Substituting (6.2) in (6.1), we obtain an equation of $u_{n\boldsymbol{k}}$:

$$\mathcal{H}_{\boldsymbol{k}} u_{n\boldsymbol{k}} = \left[\frac{p^2}{2m} + \frac{\hbar \boldsymbol{k}.\boldsymbol{p}}{m} + \frac{\hbar^2 k^2}{2m} + \boldsymbol{V}\right] u_{n\boldsymbol{k}} = E_{n\boldsymbol{k}} u_{n\boldsymbol{k}} \tag{6.3}$$

At $\boldsymbol{k} = \boldsymbol{k}_0 = \boldsymbol{0}$, this reduces to:

$$\left(\frac{p^2}{2m} + \boldsymbol{V}\right) u_{n\boldsymbol{0}} = E_{n\boldsymbol{0}} u_{n\boldsymbol{0}} \tag{6.4}$$

and the solutions of (6.4) form a complete and orthonormal set of basis functions $u_{n\boldsymbol{0}}$. Using either degenerate or nondegenerate perturbation theory, the terms $\frac{\hbar \boldsymbol{k}.\boldsymbol{p}}{m}$ and $\frac{\hbar^2 k^2}{2m}$ can be treated as perturbation to calculate the band dispersion near any $\boldsymbol{k}_0$ by expanding around $\boldsymbol{k}_0$ of known $E_{n\boldsymbol{k}_0}$ and $u_{n\boldsymbol{k}_0}$.

Assuming that the band structure has an extremum at the energy $E_{n\boldsymbol{0}}$ where the band is nondegenerate, the eigenfunctions $u_{n\boldsymbol{k}}$ and eigenvalues $E_{n\boldsymbol{k}}$ at a neighbouring point $\boldsymbol{k}$ can be expanded to second order in k in terms of the unperturbed wavefunctions $u_{n\boldsymbol{0}}$ and energies $E_{n\boldsymbol{0}}$ by treating the terms involving k in (6.3) as perturbations.

$$u_{n\boldsymbol{k}} = u_{n\boldsymbol{0}} + \frac{\hbar}{m} \sum_{n' \neq n} \frac{\langle u_{n\boldsymbol{0}} | \boldsymbol{k}.\boldsymbol{p} | u_{n'\boldsymbol{0}} \rangle}{E_{n\boldsymbol{0}} - E_{n'\boldsymbol{0}}} u_{n'\boldsymbol{0}} \tag{6.5}$$

and

$$E_{n\boldsymbol{k}} = E_{n\boldsymbol{0}} + \frac{\hbar^2 k^2}{2m} + \frac{\hbar^2}{m^2} \sum_{n' \neq n} \frac{|\langle u_{n\boldsymbol{0}} | \boldsymbol{k}.\boldsymbol{p} | u_{n'\boldsymbol{0}} \rangle|^2}{E_{n\boldsymbol{0}} - E_{n'\boldsymbol{0}}} \tag{6.6}$$

The linear terms in k vanish because $E_{n\boldsymbol{0}}$ has been assumed to be an extremum. It is conventional to express the energy $E_{n\boldsymbol{k}}$ for small values of k as:

$$E_{n\boldsymbol{k}} = E_{n\boldsymbol{0}} + \frac{\hbar^2 k^2}{2m^*} \tag{6.7}$$

where m^* is defined as the effective mass of the band. Therefore, the effective mass of a nondegenerate band can be calculated by:

$$\frac{1}{m^*} = \frac{1}{m} + \frac{2}{m^2 k^2} \sum_{n' \neq n} \frac{|\langle u_{n\boldsymbol{0}} | \boldsymbol{k}.\boldsymbol{p} | u_{n'\boldsymbol{0}} \rangle|^2}{E_{n\boldsymbol{0}} - E_{n'\boldsymbol{0}}} \tag{6.8}$$

It shows that an electron in a solid has a mass different from that of a free electron because of coupling between electronic states in different bands via $\boldsymbol{k}.\boldsymbol{p}$ term, which depends on two factors:

- A wavefunction $u_{n'\boldsymbol{0}}$ can couple to $u_{n\boldsymbol{0}}$ only if the matrix element $\langle u_{n'\boldsymbol{0}} | \boldsymbol{k}.\boldsymbol{p} | u_{n\boldsymbol{0}} \rangle$ is nonzero.

- The energy separation $E_{n'\mathbf{0}} - E_{n\mathbf{0}}$ between the two bands n and n' determines the relative importance of the contribution of n' to the effective mass of n. Bands with energy less than $E_{n\mathbf{0}}$ will contribute a positive term to $\frac{1}{m^*}$ making m^* smaller than the free electron mass. Bands with energies higher than $E_{n\mathbf{0}}$ tend to increase m^* or even cause m^* to become negative as in the case of the top valence bands in the diamond- and zinc-blende-type semiconductors.

In addition to this, the Bir-Pikus strain Hamiltonian can be derived and used through the transformation of coordinates in appropriate directions.

2. Basic Equations of Semiconductor Device Physics [14]

The Schrödinger equation is solved for heterostructure systems for a single charge carrier. In many devices with a large number of charge carriers are present, it is necessary to solve the electrostatics describing the system, in order to determine if typical carrier densities would give rise to a significant additional potential on top of the usual band-edge potential terms.

When the semiconductor is doped with donors, for example, the donors become ionised and supply electrons forming new charge distribution. The divergence of the electric field $\boldsymbol{E}$ arising from a charge distribution ρ can be expressed by using Poisson's equation:

$$\nabla . \boldsymbol{E} = \frac{\rho}{\epsilon} \tag{6.9}$$

where $\epsilon = \epsilon_r \epsilon_0$ is the permittivity of the material. The charge density in a semiconductor was given by free carriers such as electrons in the conduction band (negative), holes in valence band (positive) and space charge due to ionized donors (positive) and acceptors (negative). Therefore, it is given by:

$$\rho = q(p - n + N_D^+ - N_A^-) \tag{6.10}$$

where p and n are the densities of holes and electrons, and N_D^+ and N_A^- are the densities of ionized donors and acceptors.

Both electrons and holes contribute to current flow by drift and diffusion processes. The total current density of electrons is given by:

$$J_e = q\mu_e n\boldsymbol{E} + qD_e \nabla . n \tag{6.11}$$

and for holes it is given by:

$$J_h = q\mu_h p\boldsymbol{E} - qD_h \nabla . p \tag{6.12}$$

where the mobilities and diffusion constants are related through the Einstein relationships:

$$D_e = \frac{kT}{q}\mu_e \tag{6.13}$$

and

$$D_h = \frac{kT}{q}\mu_h \tag{6.14}$$

Finally, it is important to keep track of the number of electrons and holes in a system. This is given by continuity equations for electrons and holes:

$$\frac{1}{q}\nabla . J_e = R - G \tag{6.15}$$

and

$$\frac{1}{q}\nabla . J_h = G - R \tag{6.16}$$

where G is the net generation rate and R is the net recombination rate.

Appendix C: Publications

1. First Author Publications

The results of limiting efficiency and fundamental loss calculations for photon ratchet IBSCs were published in the Applied Physics Letter proposing the introduction of a photon ratchet band which would benefit IBSCs. The details are as follows: [43]

Title: Photon ratchet intermediate band solar cells
Journal: Applied Physics Letter
Volume: **100**
Issue: 26
Published online: 27th June 2012
doi: http://dx.doi.org/10.1063/1.4731277

The results of photocurrent measurement due to sequential absorption of photons in a single quantum well solar cell were published in the Journal of Photovoltaics demonstrating that a quantum well is a suitable candidate for an intermediate band solar cell. The details are as follows: [38]

Title: Progress towards Realizing an Intermediate Band Solar Cell – Sequential Absorption of Photons in a Quantum Well Solar Cell
Journal: Journal of Photovoltaics
Volume:**4**
Issue: 2
Published on: 10th February 2014
doi: http://dx.doi.org/10.1109/JPHOTOV.2014.2301891

2. Co-Author Publications

Daniel J. Farrell and Megumi Yoshida, *Operating regimes for second generation luminescent solar concentrators*, Progress in Photovoltaics: Research and Applications, Vol. 20, 1, 93-99, **2012**

Roland B. Piper, Megumi Yoshida, Daniel J. Farrell, Tony Khoury, Maxwell J. Crossley, Timothy W. Schmidt, Saif A. Haquea and N. J. Ekins-Daukesa, *Kinetic insight into bimolecular upconversion: experiment and simulation*, RSC Advances, 4, 8059-8063, **2014**

3. Conferences

M. Yoshida, H. Amrania, B. Browne, E. Yoxall, N. J. Ekins-Daukes and C. Phillips, *The importance of multi-photon absorption in solar cells and study of inter-subband transitions in a quantum well structure*, Proceeding for Photovoltaic Science Application and Technology (PVSAT-7) Conference and Exhibition,087, **2011**

Megumi Yoshida, Nicholas J. Ekins-Daukes, Daniel J. Farrell and Chris C. Phillips, *Photon Ratchet Intermediate Band Solar Cells*, 21st International Photovoltaic Science and Engineering Conference, Fukuoka, **2011**

Megumi Yoshida, Nicholas J. Ekins-Daukes, Daniel J. Farrell and Chris C. Phillips, *Photon Ratchet Intermediate Band Solar Cells*, UK Semiconductor Conference, Sheffield, **2012**

M. Yoshida, H. Amrania, D. J. Farrell, B. Browne, E. Yoxall, N. J. Ekins-Daukes and C. C. Phillips, *Progress towards Realizing an Intermediate Band Solar Cell – Sequential Absorption of Photons in a Quantum Well Solar Cell*, 39th IEEE Photovoltaic Specialists Conference, Tampa, **2013**

4. Seminars

Megumi Yoshida, Nicholas J. Ekins-Daukes, Daniel J. Farrell and Chris C. Phillips, *Photon Ratchet Intermediate Band Solar Cells*, High Efficiency Materials for Photovoltaics, London, **2012**

M. Yoshida, H. Amrania, D. J. Farrell, B. Browne, E. Yoxall, N. J. Ekins-Daukes and C. C. Phillips, *Progress towards Realizing an Intermediate Band Solar Cell – Sequential Absorption of Photons in a Quantum Well Solar Cell*, Naval Research Laboratory, **2013**

M. Yoshida, H. Amrania, D. J. Farrell, B. Browne, E. Yoxall, N. J. Ekins-Daukes and C. C. Phillips, *Progress towards Realizing an Intermediate Band Solar Cell – Sequential Absorption of Photons in a Quantum Well Solar Cell*, University of Kobe, **2014**

Bibliography

[1] E. Cook, *The Flow of Energy in an Industrial Society*, Scientific American, Vol. 10, 225(3), **1971**
[2] the U.S. Energy Information Administration (EIA), *The International Energy Outlook 2013*, **July 2013**
[3] V. Smil, *Energy Transitions – History, Requirements, Prospects*, Praeger Publishers Inc. ISBN 0313381771, **2010**
[4] N. Huddleston. *Understanding and Responding to Climate Change*, the National Research Council, US National Academy of Sciences. **2013**
[5] P. M. Vitousek, *Beyond Global Warming: Ecology and Global Change*, Ecological Society of America Ecology, Vol. 75, 7, 1861-1876, **1994**
[6] National Aeronautics and Space Administration, *Sun: Facts & Figures*, http://solarsystem.nasa.gov/planets/profile.cfm?Display=Facts&Object=Sun (01/08/2014)
[7] David S. Ginley, David Cahen, *Fundamentals of Materials for Energy and Environmental Sustainability, Global Energy Flow*, Cambridge University Press, ISBN: 9781107000230, **February** 2012
[8] BP Statistical Review of World Energy, **2013** http://www.bp.com/en/global/corporate/about-bp/energy-economics/statistical-review-of-world-energy.html (01/08/2014)
[9] *25th Annual Data Collection Results: PV Production Explodes in 2008*, PVNews, Vol. 28, 4, 15-18, **April 2009**
[10] M. A. Green, *Third Generation Photovoltaics: Advanced Solar Energy Conversion*, Springer, ISBN 3-402-65627, **2005**
[11] http://www.ise.fraunhofer.de/en/press-and-media/press-releases/presseinformationen-2013/world-record-solar-cell-with-44.7-efficiency **23 september 2013**
[12] J. Nelson, *The Physics of Solar Cells,* Imperial College Press, ISBN 1-86094-349-7, **2003**
[13] P. Wurfel, *Physics of Solar Cells,* Wiley-VCH, ISSBN 3-527-40428, **2005**
[14] M. A. Green, *Solar Cells: Operating Principles, Technology and System Applications*, Prentice-Hall, ISBN 0-13-82270, **1986**
[15] W. Shockley, H. J. Queisser, *Detailed Balance Limit of Efficiency of p-n Junction Solar Cells*, Journal of Applied Physics, Vol. 32, 3, 510, **1961**
[16] C. H. Henry, *Limiting efficiencies of ideal single and multiple energy gap terrestrial solar cells*, Journal of Applied Physics, Vol. 51, 8, 4494, **1980**
[17] L. C. Hirst and N. J. Ekins-Daukes, *Fundamental losses in solar cells*, Progress in Photovoltaics, Vol. 19, 3, 286, **2011**
[18] P. T. Landsberg, T. Markvart, *The Carnot factor in solar cell theory*. Solid-State Electronics, Vol. 42, 4, 657–659, **1998**
[19] P. Wurfel, *Thermodynamic limitations to solar energy conversion*, Physica E: low-dimensinal systems and nanostructures, vol. 14, 18, **2002**
[20] Markvart T. *Thermodynamics of losses in photovoltaicconversion*. Applied Physics Letters, Vol. 91, 6, 64102, **2007**
[21] G. L. Araujo, A. Martı, *Absolute limiting efficiencies for photovoltaic energy conversion*. Solar Energy Materials and Solar Cells, Vol. 33, 2, 213, **1994**
[22] A. Luque and A. Martí, *Increasing the efficiency of ideal solar cells by photon induced transitions at intermediate levels*, Physical Review Letters, Vol. 78, 26, 5014 -5017, **1997**
[23] Y. Okada, T. Morioka, K. Yoshida, R. Oshima, Y. Shoji, T. Inoue and T. Kita, *Increase in photocurrent by optical transitions via intermediate quantum states in direct-doped InAs/GaNAs strain-compensated quantum dot solar cell*, Journal of Applied Physics, Vol. 109, 024301, **2011**
[24] A. Luque and A. Marti, *Quantum dot intermediate band solar cell*, in Proc. 28th IEEE Photovoltaics Specialists Conference, 940, **2000**
[25] W. G. Hu, T. Inoue, O. Kojima and T. Kita, *Energy band structure and the half-filling of the intermediate band in the quantum-dot solar cell*, Physica Status Solild C, Vol. 8, 622, **2011**

[26] E. Antolín, A. Martí, J. Olea, D. Pastor, G. González-Díaz, I. Mártil, and A. Luque, *Lifetime recovery in ultrahighly titanium-doped silicon for the implementation of an intermediate band material*, Applied Physics Letter, Applied Physics, Vol. 94, 042115, **2009**
[27] W. Wang, A. S. Lin, and J. D. Phillips, *Intermediate-Band Photovoltaic Solar Cell Based on ZnTe:O* Journal of Applied Physics, Vol. 95, 011103, **2009**
[28] A. Luque, A. Martí, N. López, E. Antolín, and E. Cánovas, *Operation of the intermediate band solar cell under non-ideal space charge region conditions and half-filling of the intermediate band*, Journal of Applied Physics, Vol. 99, 094503, **2006**
[29] S. M. Hubbard, C. D. Cress, C. G. Bailey, R. P. Raffaelle, S. G. Bailey, and D. M. Wilt, *Effect of strain compensation on quantum dot enhanced GaAs solar cells*, Applied Physics Letters, Vol. 92, 12, 123512, **2008**
[30] W. Shockley and W. T. Read, Jr., *Statistics of the Recombinations of Holes and Electrons*, Physcal Review, Vol. 87, 835, **1952**; R. N. Hall, *Electron-Hole Recombination in Germanium*, Physcal Review, Vol. 87, 387, **1952**
[31] N. J. Ekins-Daukes, C. B. Honsberg, and M. Yamaguchi, *Signature of intermediate band materials from luminescence measurements*, in Proceedings of the 31st IEEE Photovoltaic Specialists Conference, Orlando, Florida, Vol. 49, **2005**
[32] A. Erol, Dilute III-V Nitride Semiconductors and Materials systems, Springer Berlin Heidelberg, ISBN 978-3-540-74528-0, **2008**
[33] W. Shan, W. Walukiewicz, J. W. Ager III, E. E. Haller, J. F. Geisz, D. J. Friedman, J. M. Olson and Sarah R. Kurtz, *Effect of nitrogen on the band structure of GaInNAs alloys*, Journal of Applied Physics, Vol. 86, 2349, **1999**
[34] N. López, L. A. Reichertz, K. M. Yu, K. Campman, and W. Walukiewicz, *Engineering the Electronic Band Structure for Multiband Solar Cells*, Physcal Review Letter, Vol. 106, 028701, **2011**
[35] Nazmul Ahsan, Naoya Miyashita, Muhammad Monirul Islam, Kin Man Yu, Wladek Walukiewicz and Yoshitaka Okada, *Two-photon excitation in an intermediate band solar cell structure*, Applied Physics Letters, Vol. 100, 172111, **2012**
[36] R. Heitz, T. R. Ramachandran, A. Kalburge, Q. Xie, I. Mukhametzhanov, P. Chen, and A. Madhukar, *Observation of Reentrant 2D to 3D Morphology Transition in Highly Strained Epitaxy: InAs on GaAs*, Physcal Review Letter, Vol. 78, 4071, **1997**
[37] A. Martí, E. Antolín, C. R. Stanley, C. D. Farmer, N. López, P. Díaz, E. Cánovas, P. G. Linares and A. Luque, *Production of Photocurrent due to Intermediate-to-Conduction-Band Transitions: A Demonstration of a Key Operating Principle of the Intermediate-Band Solar Cell*, Physical Review Letters, Vol. 97, 247701, **2006**
[38] M. Yoshida, H. Amrania, D. J. Farrell, B. Browne, E. Yoxall, N. J. Ekins-Daukes and C. C. Phillips, *Progress towards Realizing an Intermediate Band Solar Cell – Sequential Absorption of Photons in a Quantum Well Solar Cell*, IEEE Journal of Photovoltaics, Vol. 4, 2, 2014
[39] M. Sugiyama, Y. Wang, K. Watanabe, T. Morioka, Y. Okada, *Photocurrent Generation by Two-Step Photon Absorption With Quantum-Well Superlattice Cell*, IEEE Journal of Photovoltaics, Vol.2, 3, 298, **2012**
[40] T. Kita, T. Maeda, and Y. Harada, *Carrier dynamics of the intermediate state in InAs/GaAs quantum dots coupled in a photonic cavity under two-photon excitation*, Physical Review B, Vol. 86, 035301, **2012**
[41] K. Yoshida, Y. Okada, and N. Sano, Appl. Phys. Lett. 97, 133503 (2010)
[42] M. Helm, *The basic physics of intersubband transitions*, in Semiconductors and Semimetals Vol. 62, 1–99, Academic, New York, **1999**
[43] M. Yoshida, N. J. Ekins-Daukes, D. J. Farrell and C. C. Phillips, *Photon ratchet intermediate band solar cells*, Applied Physics Letters Vol. 100, 26, **2012**
[44] P. Wahnón and C. Tablero, *Ab initio electronic structure calculations for metallic intermediate band formation in photovoltaic materials*, Physical Review B, Vol. 65, 165115, **2002**
[45] B. Fückel, D. A. Roberts, Y. Y. Cheng, R. G. C. R. Clady, R. B. Piper, N. J. Ekins-Daukes, M. J. Crossley and T. W. Schmidt, *Singlet Oxygen Mediated Photochemical Upconversion of NIR Light*, Journal of Physical Chemistry Letters, Vol. 2, 9, 966–971, **2011**

[46] N. J. Ekins-Daukes and T. W. Schmidt, *A molecular approach to the intermediate band solar cell: The symmetric case*, Applied Physics Letter Vol. 93, 063507, **2008**
[47] P. Olsson, C. Domain, and J. F. Guillemoles, *Ferromagnetic Compounds for High Efficiency Photovoltaic Conversion: The Case of AlP:Cr*, Physical Review Letter, Vol. 102, 227204, **2009**
[48] J. Faist, F. Capasso, D. L. Sivco, A. L. Hutchinson, C. Sirtori, S. N. G. Chu, and A. Y. Cho, Quantum cascade laser: *Temperature dependence of the performance characteristics and high T_0 operation*, Applied Physics Letter Vol. 65, 2901, **1994**
[49] Jérôme Faist, Federico Capasso, Carlo Sirtori, Deborah L. Sivco, Albert L. Hutchinson, and Alfred Y. Cho, *Vertical transition quantum cascade laser with Bragg confined excited state*, Applied Physics Letters, Vol. 66, 538, **1995**
[50] Rita Claudia Iotti and Fausto Rossi,*Nature of Charge Transport in Quantum-Cascade Lasers*, Physical Review Letter, Vol. 87, 14, 146603, **2001**
[51] G. Ru, F.-S. Choa, X. Wei, G. Chen, and J. B. Khurgin, *Measurement of the lifetimes of photo-excited carriers in type-I and type-II quantum well materials*, Conference on Lasers and Electro-Optics, 1-2, **2006**
[52] S. Fukatsu, H. Sunamura, Y. Shiraki, and S. Komiyama, *Phononless radiative recombination of indirect excitons in a Si/Ge type-II quantum dot*, Applied Physics Letters Vol. 71, 258-260, **1997**
[53] F. Hatami, M. Grundmann, N.N. Ledentsov, F. Heinrichsdorff, R. Heitz, J. Bohrer, D. Bimberg, S.S. Ruvimov, P. Werner, V.M. Ustinof, P.S. Kop'ev and Zh.I. Alferov, *Carrier dynamics in type-II GaSb/GaAs quantum dots*, Physical Review B, Vol. 57, 4635-4641, **1998**
[54] G.A. Bastard, *Wave Mechanics Applied to Semiconductor Heterostructures*, Les Editions de Physique, Paris, ISBN 978-0470217085, **1988**
[55] L. C. West and S. J. Eglash, *First observation of an extremely large ‐dipole infrared transition within the conduction band of a GaAs quantum well*, Applied Physics Letters, Vol. 46, 1156, **1985**
[56] A. De Vos ,*Thermodynamics of Solar Energy Conversion*, Wiley-VCH, ISBN 978-3-527-40841-2, **1995**
[57] American Society for Testing and Materials (ASTM) Terrestrial Reference Spectra for Photovoltaic Performance Evaluation http://rredc.nrel.gov/solar/spectra/am1.5/
[58] A. Luque, A. Marti, *The Intermediate Band Solar Cell: Progress Toward the Realization of an Attractive Concept*, Advanced Materials, Vol. 22, 160-174, **2010**
[59] L. Cuadra, A. Marti andA. Luque, *Influence of the overlap between the absorption coefficients on the efficiency of the intermediate band solar cell*, IEEE Transactions on Electron Devices, Vol. 51, 1002, **2004**
[60] N. L. A. Chan, N. J. Ekins-Daukes, H. E. Bridley, *Optimal bandgap combinations - Does material quality matter?*, IEEE Journal of Photovoltaics, Vol. 2, 2, **2012**
[61] A. M. Kechiantz, L. M. Kocharyan and H. M. Kechiyants, *Band alignment and conversion efficiency in Si/Ge type-II quantum dot intermediate band solar cells*, Nanotechnology, Vol. 18, 405401, **2007**
[62] M. Wolf and H. Rauschenbach, *Series resistance effects on solar cell measurements*, Advanced Energy Conversion, Vol. 3, 2, 455-479, **1963**
[63] K. P. O'Donnell and X. Chen, *Temperature dependence of semiconductor band gaps*, Applied Physics Letter, Vol. 58, 25, **1991**
[64] Y. P. Varshni, *Temperature Dependence of The Energy Gap in Semiconductors*, Physica 34, 149-154, **1967**
[65] J. Nelson, M. Paxman, K.W.J. Barnham, J.S. Roberts, C.C. Button, *Steady-State Carrier Escape from Single Quantum Wells*, IEEE Journal of Quantum. Electron, Vol. 29, 1460-1468, **1993**
[66] A. Zachariou, J. Barnes, K. W. J. Barnham, J. Nelson, E. S. M. Tsui, J. Epler, and M. Pate, *A carrier escape study from InP/InGaAs single quantum well solar cells*, Journal of Applied Physics, Vol. 83, 877-881, **1998**
[67] A. I. M. Rae, *Quantum Mechanics*, Taylor and Francis, ISN 1-58488-970-5, **2008**
[68] P. Harrison, *Quantum Wells, Wires and Dots*, Wiley, ISBN 0-470-01080-0, **2005**
[69] S. Birner, nextnano semiconductor soltware soluions, http://www.nextnano.com/ (01/08/2014)

[70] Paul H. Holloway and Gary E. McGuire, *Handbook of Compound Semiconductors: Growth, Processing, Characterization, and Devices*, Cambridge University Press, ISBN: 978-0-8155-1374-2, **2008**
[71] B.A. Joyce, *Molecular beam epitaxy of semiconductor films—atomic dimension control and the evaluation of crystal growth dynamics*, Contemporary Physics, Vol. 32, 1, 21-34, **1991**
[72] M. Razeghi and A. Rogalski, *Semiconductor ultraviolet detectors*, Journal of Applied Physics, Vol. 79, 7433, **1996**
[73] P. Y. Yu and M. Cardona, *Fundamentals of Semiconductors - Physics and Materials Properties, 3rd edition, Springer*, ISBN 3-540-25470-6, **2005**